

2.6.12.1985

THE EFFECT OF NON-LOCAL CONDUCTIVITY ON MICROWAVE TRANSMISSION
THROUGH FERROMAGNETIC METALS

by

Kenneth Bjorn Urquhart

B. Sc., Simon Fraser University, 1983

A THESIS SUBMITTED IN PARTIAL FULFILLMENT OF
THE REQUIREMENTS FOR THE DEGREE OF
MASTER OF SCIENCE
in the Department
of
Physics

© Kenneth Bjorn Urquhart 1985

SIMON FRASER UNIVERSITY

April 1985

All rights reserved. This work may not be reproduced in whole or in part, by photocopy or other means, without permission of the author.

APPROVAL

Name: Kenneth Bjorn Urquhart

Degree: Master of Science

Title of Thesis: The Effect of Non-local Conductivity on
Microwave Transmission Through Ferromagnetic
Metals

Examining committee:

Chairman: B. P. Clayman

J. F. Cochran
Senior Supervisor

R. H. / Enns

B. Heinrich
External Examiner
Department of Physics
Simon Fraser University

Date Approved: April 4, 1985

PARTIAL COPYRIGHT LICENSE

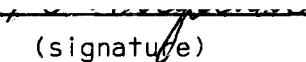
I hereby grant to Simon Fraser University the right to lend my thesis, project or extended essay (the title of which is shown below) to users of the Simon Fraser University Library, and to make partial or single copies only for such users or in response to a request from the library of any other university, or other educational institution, on its own behalf or for one of its users. I further agree that permission for multiple copying of this work for scholarly purposes may be granted by me or the Dean of Graduate Studies. It is understood that copying or publication of this work for financial gain shall not be allowed without my written permission.

Title of Thesis/Project/Extended Essay

The Effect of Non-Local Conductivity on Microwave Transmission

through Ferromagnetic Metals

Author:


(signature)

Kenneth Bjorn URQUHART

(name)

April 18, 1985

(date)

ABSTRACT

The transmission of 24 GHz microwave radiation through a slab of ferromagnetic metal has been numerically evaluated as a function of a static magnetic field oriented normal to the plane of the slab. The calculations assumed a metal with a spherical Fermi surface whose parameters were chosen to simulate Nickel. The current density at a point was non-locally related to the electric field throughout the metal and the two limiting cases of specular and diffuse surface scattering of the current carriers were investigated.

The transmission was calculated as a function of the applied field for mean free paths l ranging from $\delta/l \gg 1$ (normal skin effect regime) to $\delta/l \ll 1$ (extreme anomalous skin effect regime), where δ is the rf skin depth. In the anomalous skin effect regime ($\delta/l \leq 1$) the transmission was found to depend on the type of surface scattering. For slabs of thickness $d > \delta$ (typically, $\delta \approx 0.8 \mu\text{m}$ while $d > 1 \mu\text{m}$), a strong transmission peak appeared when the static magnetic field was at a value corresponding to ferromagnetic resonance (FMR) and diffuse scattering was used. No such peak appeared using specular surface scattering. Further, when $\delta \ll d \leq l$, the calculations carried through for diffuse scattering showed a transmission maximum at an applied field corresponding to cyclotron resonance of the carriers while the calculations carried out using specular scattering showed a transmission minimum at the same static magnetic field value.

ACKNOWLEDGEMENTS

First of all, I would like to thank John Cochran and Bretislav Heinrich for all their help and encouragement with my work.

I wish to thank Jill Tasker, Paul Caron, Bill Ballantyne, and Dan Yancey for keeping me company during the many late nights and early mornings I spent parked in front of a computer terminal doing calculations. I also wish to thank Joni Anderson and Diane Guenther of Production Services for all the times they resurrected my damaged data sets.

I want to thank Doreen Young for the dance lessons and Don Hunter for allowing me to bounce so many ideas off his balding dome. I would like to thank my co-workers Ken Myrtle and Jeff Rudd for the many interesting discussions we had about matters physical and otherwise.

Finally, I wish to acknowledge the financial support of the Natural Sciences and Engineering Research Council and Simon Fraser University which made this work possible.

TABLE OF CONTENTS

Approval ii

Abstract iii

Acknowledgements iv

List of Figures viii

1. INTRODUCTION 1

2. THE ELECTRIC FIELD IN THE SLAB 17

 2.1 Introduction 17

 2.2 Maxwell's Equations in the Perpendicular Configuration 18

 2.3 The Constitutive Relation Between \mathbf{B} and \mathbf{H} 23

 2.4 The Constitutive Relation Between \mathbf{j} and \mathbf{E} 28

 2.5 The Boundary Value Problem 32

 2.5.1 BVP I: Circular Polarization, Free Space 35

 2.5.2 BVP II: Linear Polarization, Anisotropic Space 44

 2.6 Chapter Summary 51

3. CALCULATING THE CIRCULARLY POLARIZED KERNELS 57

 3.1 Introduction 57

 3.2 The Kernels in an Infinite Medium 60

 3.2.1 A Closed Form for the Kernels 71

 3.3 A Sum Rule to Check the Kernels 72

 3.4 The Conductivity Tensor 74

 3.4.1 Limiting Forms of $k(\mathbf{y})$ 75

4. SOLUTION IN THE NORMAL SKIN EFFECT REGIME 78

 4.1 Introduction 78

 4.2 The NSE Solutions 79

4.3	Predictions of the NSE Transmission Theory	82
4.3.1	Variation of NSE Surface Impedance with Magnetic Field	82
4.3.2	Variation of NSE Transmission Coefficient with Magnetic Field	85
5.	ELECTRIC FIELD SOLUTION FOR DIFFUSE SURFACE SCATTERING	91
5.1	Introduction	91
5.1.1	Summation Convention	93
5.2	The Boundary Value Problem for Diffuse Scattering	94
5.3	Reduction to a Set of Simultaneous Equations	97
5.4	Incorporation of Boundary Conditions	103
5.5	The Integrated Current Elements	107
5.6	Evaluation of the Integrated Current Elements ...	112
5.6.1	Summary of Integrated Current Elements	117
5.6.2	The Function $G(x)$	120
5.7	Recovery of the NSE results	121
5.8	The Magnetic Field and Current Density in the Slab	123
5.9	Implementation on a Computer	124
5.9.1	Convergence of the Numerical Solution	125
6.	ELECTRIC FIELD SOLUTION FOR SPECULAR SURFACE SCATTERING	130
6.1	Introduction	130
6.2	Solution of the Boundary Value Problem	131
6.3	Evaluation of the Series Solutions	140
6.3.1	An Estimation of the Sum Limit p	143
6.3.2	A More Formal Way of Evaluating the Series	145
6.4	Integral Form for the Transmission Coefficient ..	147

6.4.1 Evaluation of The Contour Integral	151
6.4.2 Residue Evaluation	156
6.4.3 The Net Integral Solution	158
6.5 Implementation of The Integral Solution	159
6.5.1 Numerical Evaluation of the Integral	160
6.5.2 Numerical Extraction of the Roots of $y^2+ak(y)$..	161
6.6 Closed Forms for the Transmission Coefficients in the Thick Slab Limit ($d/l \gg 1$)	164
7. RESULTS AND DISCUSSION	169
7.1 Introduction	169
7.2 Calculated Results	171
7.2.1 Variation of the Surface Impedance with H_0 and l	171
7.2.2 Variation of T_- with H_0 , l and d	174
7.2.3 Variation of T_+ with H_0 and l	179
7.3 Discussion of the Transmission Behaviour	179
7.4 Scaling Properties of the Transmission Coefficients	189
7.5 The Linearly Polarized Transmission Coefficient ..	192
Appendix A: Nickel Parameters	202
Appendix B: Linear and Circular Polarization	204
Appendix C: Generalized Boundary Conditions	208
Appendix D: Semi-Classical Current Density Calculation	212
Appendix E: The Exponential Integral	219
Appendix F: Gauss-Laguerre Quadrature	222
BIBLIOGRAPHY	224

LIST OF FIGURES

FIGURE		PAGE
1	Transmission Amplitude Calculated Using Room Temperature Theory	3
2	Electric Field Distribution in a 5 μm Thick Slab for a Conduction Mean Free Path of 25 μm	13
3	The Geometry of the Perpendicular Configuration	19
4	Symmetry Relations Among the Transverse Kernel Elements	31
5	Boundary Value Problem Associated With Transmission of Circularly Polarized Waves	36
6	Boundary Value Problem Associated With Transmission of Linearly Polarized Waves	45
7	Geometry Used to Calculate the Kernels in an Infinite Medium	62
8	Variation of the Positive Circularly Polarized Permeability μ_+ with H_0	83
9	Variation of the Negative Circularly Polarized Permeability μ_- with H_0	84
10	Variation of Positive Circularly Polarized Surface Impedance with H_0 in NSE Regime	86
11	Variation of Negative Circularly Polarized Surface Impedance with H_0 in NSE Regime	87
12	Variation of Positive Circularly Polarized Transmission Coefficient with H_0 in NSE Regime ...	89
13	Variation of Negative Circularly Polarized Transmission Coefficient with H_0 in NSE Regime ...	90
14	Equivalent Problems for Calculating the Kernels in a Finite Slab and in an Infinite Medium	95
15	Subdivision of Slab for Numerical Solution of Diffuse Scattering Problem	98

16	Matrix Equation for the N+1 Electric Field Points Across the Slab (Diffuse Scattering Solution) ...	104
17	Modified Matrix Equation for New Boundary Conditions $E(0)=1$, $h(d)=0$	106
18	Total Integrated Current Matrix for $N = 5$	108
19	Total Integrated Current Matrix for $N = 5$ Filled Using Only $2N$ Elements and Symmetry Relationships	113
20	Plot of $ T_{\pm} $ vs. N to see how the diffuse scattering solutions converge with N	127
21	Plot of $\log_{10} G_{\pm}(z) $ vs. z toto check convergence of diffuse scattering solution	128
22	Plot of $\log_{10} G_{\pm}(z) $ vs. z tocheck convergence of diffuse scattering solution	129
23	Equivalence Between the Current Response in a Finite Metal Slab and an Infinite Conducting Medium for Specular Surface Scattering	133
24	The Generation of Identical Current Densities in a Finite Slab and and Infinite Medium for Specular Surface Scattering	135
25	Relation Between the Branch Cuts of $\ln(t)$ and $\ln((1+y)/(1-y))$	152
26	Integration Contour Used to Evaluate The Transmission Coefficient Integral	154
27	Plots of $ z_-^5 $ vs. H_0 for $\delta/l \gg 1$ to $\delta/l \ll 1$	172
28	Plots of $ T_- $ vs. H_0 and l for $d = 2 \mu\text{m}$	175
29	Plots of $ T_- $ vs. H_0 and l for $d = 5 \mu\text{m}$	176
30	Plots of $ T_- $ vs. H_0 and l for $d = 10 \mu\text{m}$	177
31	Plots of $ T_+ $ vs. H_0 and l for $d = 2 \mu\text{m}$	180
32	Plots of $ T_+ $ vs. H_0 and l for $d = 5 \mu\text{m}$	181
33	Plots of $ T_+ $ vs. H_0 and l for $d = 10 \mu\text{m}$	182
34	Plots of T_- components vs. H_0 for Specular Surface Scattering and $l = 0.03 \mu\text{m}$	184

35	Plots of T_{-} components vs. H_0 for Specular Surface Scattering and $l = 2 \mu\text{m}$	185
36	Electric Field Distribution in a $5 \mu\text{m}$ Thick Slab for a Conduction Mean Free Path of $25 \mu\text{m}$	188
37	Ratio of $ T_{-}/T_{-}(d/l \gg 1) $ for Specular Surface Scattering.	190
38	Ratio of $ T_{-}/T_{-}(d/l \gg 1) $ for Diffuse Surface Scattering.	191
39	Plots of $\log_{10} T $ vs. H_0 for $d = 2 \mu\text{m}$ and Specular Scattering	194
40	Plots of $\log_{10} T $ vs. H_0 for $d = 2 \mu\text{m}$ and Diffuse Scattering	195
41	Plots of $\log_{10} T $ vs. H_0 for $d = 5 \mu\text{m}$ and Specular Scattering	196
42	Plots of $\log_{10} T $ vs. H_0 for $d = 5 \mu\text{m}$ and Diffuse Scattering	197
43	Plots of $\log_{10} T $ vs. H_0 for $d = 10 \mu\text{m}$ and Specular Scattering	198
44	Plots of $\log_{10} T $ vs. H_0 for $d = 10 \mu\text{m}$ and Diffuse Scattering	199
45	Phase Space Trajectory used to Calculate the Solution of the Boltzmann Equation	215

1. INTRODUCTION

One of the methods used to measure the magnetic properties of a ferromagnetic metal is the microwave transmission experiment¹. In the experiment, a thin slab of the subject metal is immersed in a uniform d.c. magnetic field H_0 , one side of the slab irradiated with linearly polarized microwaves, and the transmitted signal measured as a function of H_0 . Comparison between theory and experiment is simplified when H_0 is oriented either parallel to the plane of the slab (parallel configuration) or perpendicular to the plane (perpendicular configuration).

For a saturated specimen at room temperature, the variation of the transmitted signal with H_0 has been well understood using a theory that combines the Landau-Lifshitz equation of motion with Maxwell's equations in which a local conductivity characterized by Ohm's Law is assumed:

$$\vec{j}(\vec{r}) = \sigma_0 \vec{E}(\vec{r}) \quad [1.1]$$

(where σ_0 is the d.c. conductivity, $\vec{j}(\vec{r})$ is the rf current density, $\vec{E}(\vec{r})$ is the rf electric field, and both fields are assumed to have a suppressed time dependence of $\exp(-i\omega t)$). The theory predicts a maximum in the transmission for a value of H_0 that corresponds to ferromagnetic antiresonance (FMAR) in the

metal and a minimum when H_0 corresponds to ferromagnetic resonance (FMR) (a good introduction to the room temperature theory can be found in ref. 1). The general variation of the transmitted signal with H_0 is shown in figure 1. Excellent fits of transmission data have been obtained using this theory (see, for example, figure 2 in ref. 2).

However, the theory was unable to account for transmission behaviour observed in a series of parallel configuration experiments carried out by Dewar, Heinrich, and Cochran at 24 GHz on pure Nickel specimens 3 - 10 μm thick³. At room temperature (300 K), the transmission exhibited a lineshape similar to that shown in figure 1 except that a small transmission peak was located near the magnetic field value corresponding to FMR. Theory predicted a deep minimum at FMR. As the specimens were cooled, the FMR peak attenuated until it was unobservable at 80 K. Further cooling caused the normally dominant FMAR peak to attenuate until a virtually featureless transmission was obtained at 40 K. Below 20 K a new peak at FMR appeared which increased in strength until it dominated the transmission profile at liquid Helium temperature (4.2 K).

Heinrich and Cochran⁴ demonstrated that the small FMR peak at room temperature was due to energy transport across the slab by phonons generated in the skin layer by magnetoelastic coupling⁴⁻⁶ between the specimen's resonantly precessing magnetization vector and the crystal lattice.

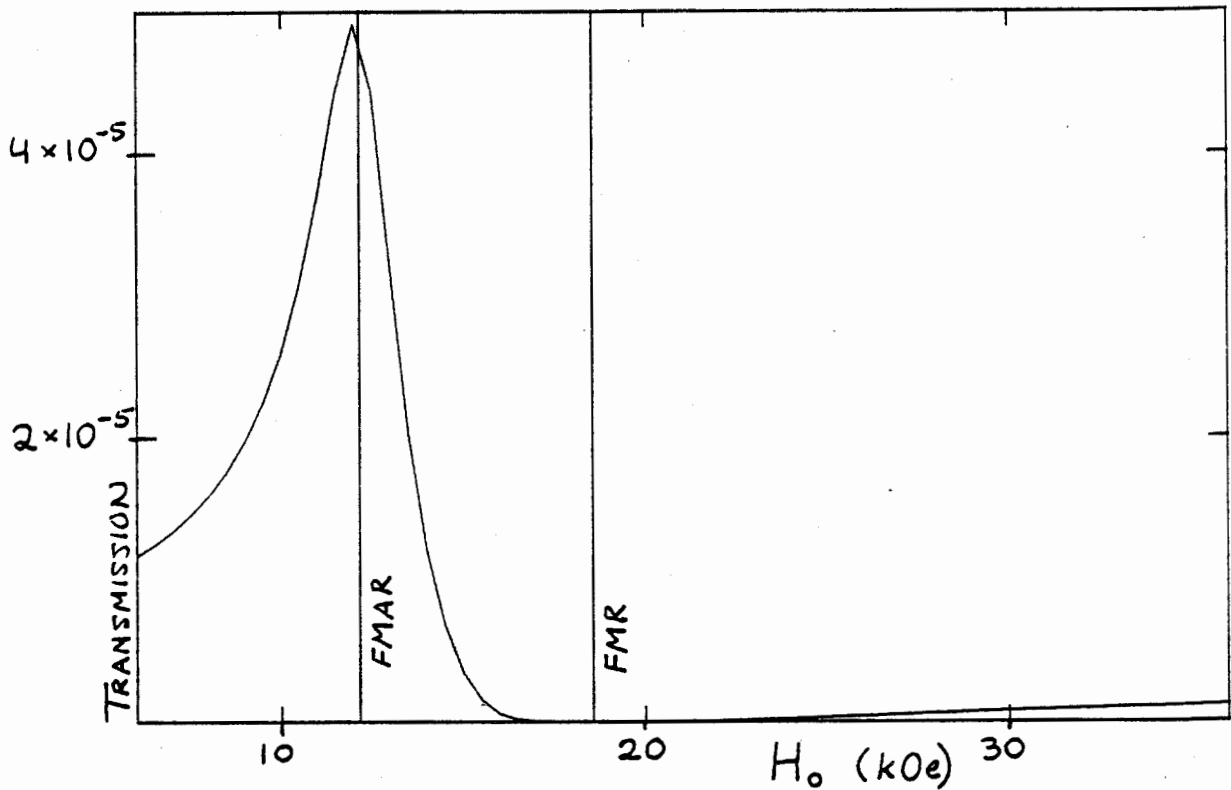


Fig. 1 Transmission amplitude versus applied magnetic field H_0 calculated for a 5 μm thick slab of Nickel using room temperature theory (see Chapter 4). H_0 was perpendicular to the plane of the slab and the incident 24 GHz microwaves were assumed to be negative circularly polarized. The parameters used in the calculation are listed in Appendix A. For these parameters, FMAR occurs at $H_0 = 12.1$ kOe and FMR occurs at $H_0 = 18.5$ koe.

But magnetoelastic coupling could definitely NOT explain the FMR peak that occurred below 20 K. The strength of an FMR transmission peak generated by magnetoelastic effects depends on the precessional amplitude of a specimen's magnetization vector⁷ and the precessional amplitude is controlled, in part, by the magnetic damping: the stronger the damping, the smaller the amplitude. In pure Nickel, the magnetic damping increases rapidly with decreasing temperature⁸. This caused the small room temperature FMR peak to attenuate and become unobservable at temperatures below about 80 K.

The most likely source of the discrepancy between theory and experiment is the theory's tacit assumption that Ohm's Law (equation [1.1]) relates the rf current density $\vec{j}(\vec{r})$ to the rf electric field $\vec{E}(\vec{r})$ in the metal. Ohm's Law is valid only in the normal skin effect (NSE) regime where the electron mean free path l is much less than the normal rf skin depth $\delta = c/(2\pi\omega\sigma_0\mu)^{1/2}$. While the condition $\delta/l \gg 1$ is satisfied by nearly all metals at room temperatures and microwave frequencies, l is not a constant in pure metals: l tends to increase with decreasing temperature. In the transmission experiments of Dewar, Heinrich, and Cochran, δ was the order of $0.5 \mu\text{m}$ while residual resistance ratio measurements indicated that l increased from approximately $0.001 \mu\text{m}$ at room temperature (300 K) to approximately $10 \mu\text{m}$ at liquid helium temperatures (4.2 K). Hence, $\delta/l \approx 500$ at 300 K (well within the NSE regime) while $\delta/l \approx 0.05$ at 4.2 K.

When $\delta/l \leq 1$, we encounter the anomalous skin effect (ASE) regime and Ohm's Law is no longer valid⁹. The rf current density at a point \bar{r} in the metal depends not only on the electric field at \bar{r} but non-locally on the rf electric field distribution throughout a region of mean radius l about \bar{r} . This new relationship can be expressed by¹⁰:

$$\bar{j}(\bar{r}) = \int_{\Omega} \bar{\kappa}(\bar{r}, \bar{\xi}) \cdot \bar{E}(\bar{\xi}) d\bar{\xi} \quad [1.2]$$

where $\bar{\kappa}(\bar{r}, \bar{\xi})$ is called the current kernel or conductivity tensor and the integral extends over the volume Ω of the metal. The kernel represents the current density generated at a point \bar{r} in the metal due to a delta function electric field at $\bar{\xi}$. Its form depends on the orientation of H_0 in the slab, the shape of the metal's Fermi surface, and the type of scattering the electrons undergo in the bulk and at the surfaces of the metal. Owing to a lack of any detailed theory about the way electrons scatter at a surface, the surface scattering is usually assumed to be specular (the component of the conduction electron's velocity normal to the surface is reversed on impact) or diffuse (the electron emerges from the collision in thermal equilibrium with its surroundings; ie, the electron loses all previous knowledge of its previous trajectory on impact)^{11,12}.

Cochran and Heinrich¹³ investigated whether or not non-local conductivity alone could explain the anomalous transmission behaviour in the pure Nickel specimens at 4.2 K.

They carried through two parallel configuration transmission calculations in the extreme anomalous limit $\delta/l \ll 1$ using a non-local current density similar to equation [1.2] for a metal with a spherical Fermi surface that magnetically resembled Nickel. Magnetoelastic coupling was neglected. The slab was chosen to be $5.0 \mu\text{m}$ thick and the mean free path was taken to be $10.8 \mu\text{m}$ (corresponding to 4.2 K in the pure Nickel specimens). One calculation was based on specular surface scattering of the conduction electrons. In contrast to the results obtained from the room temperature, or NSE theory, the non-local calculation predicted no interesting transmission features at FMAR or FMR. The transmission was nearly independent of H_0 . The second calculation employed diffuse surface scattering of the electrons and it qualitatively reproduced the anomalous, low temperature transmission behaviour observed by Dewar, Heinrich, and Cochran: a strong peak at FMR and no interesting structure at FMAR. The two authors also considered transmission enhancement by phonons generated in the slab by magnetoelastic coupling, Bragg forces, collision drag forces between the electrons and the lattice¹⁴, and driving of the lattice at the slab faces by electron collisions. These mechanisms were postulated by Dewar, et al³ as possible sources of the low temperature FMR peak, but Cochran and Heinrich found all the above mechanisms to have a very small effect on the transmission lineshape in the $\delta/l \ll 1$ (extreme ASE) limit. Cochran and Heinrich concluded that the enhanced FMR transmission seen in pure Nickel at low temperatures was due

to non-local conduction effects coupled with diffuse surface scattering of the conduction electrons.

In a recent paper¹⁵, Kogan, Turov, and Ustinov continued the theoretical investigation of microwave transmission through ferromagnetic metals in the anomalous skin effect regime. The authors considered the perpendicular configuration, ignored curvature of the electron orbits by the magnetic field, and assumed specular surface scattering of the conduction electrons. They developed an expression for the transmission through a slab of thickness d in terms of an infinite sum. The sum was used to derive closed, analytic expressions for the transmission in the two cases of extremely thick ($d/l \gg 1$) and extremely thin ($d/l \ll 1$) slabs. They concluded that no transmission maximum at FMR could be predicted from their theory in the extreme anomalous limit ($\delta/l \ll 1$) but some structure should occur at FMAR. They further expressed the opinion that repeating the calculation using diffuse surface scattering of the carriers would also fail to predict any transmission maximum at FMR; they felt that any enhanced transmission at FMR could not be attributed to non-local conductivity.

In this thesis, microwave transmission calculations for a ferromagnetic metal in the perpendicular configuration are presented. The calculations are based on numerical transmission models valid for any δ/l and slab thickness d . Both cases of specular and diffuse surface scattering of the conduction electrons were considered. The calculations were carried out

for two reasons: first, in view of the results of Cochran and Heinrich for the parallel configuration, and the conclusions of Kogan, Turov, and Ustinov, it was of interest to see what differences, if any, would exist between the transmission curves calculated for the cases of specular and diffuse surface scattering; second, it would be useful to carry through specular scattering calculations in the perpendicular configuration that explicitly took orbital effects into account and considered experimentally accessible values of l and d (ie, $0.001 \leq l \leq 100 \mu\text{m}$ and $1 \leq d \leq 30 \mu\text{m}$). The extreme thin slab result of Kogan, Turov, and Ustinov cannot be checked experimentally - the thin specimens required cannot be fabricated. The extreme thick slab result cannot be checked either. When $d/l \gg 1$, and $\delta/l \ll 1$, their expression for the transmitted microwave power contained the factor $\exp(-2d/l)$. Taking l to be $1 \mu\text{m}$ (a reasonable value in a pure metal at liquid helium temperature), d to be $100 \mu\text{m}$ (to keep $d/l \gg 1$), and assuming a 1 Watt incident microwave beam, the thick slab expression predicts a transmitted power level well below the 10^{-20} Watt limit of experimental detectability¹.

Our transmission calculations were carried through for a model metal with a spherical Fermi surface that magnetically resembled Nickel (the same type of metal that Cochran and Heinrich considered and the kind of metal for which the Kogan, Turov, and Ustinov results were derived). The effective mass and Fermi velocity were chosen to correspond to the majority

carriers in Nickel: $m^*/m_0 = 5$ and $v_F = 2 \times 10^7$ cm/sec, where m_0 is the free electron mass. These values were taken from the low temperature cyclotron resonance data for sp band belly orbits reported by Goy and Grimes¹⁶. The current kernel $\tilde{\kappa}(\vec{r}, \vec{\xi})$ needed to calculate the non-local current density (equation [1.2]) was derived semi-classically using the Boltzmann transport equation in the relaxation time approximation^{10, 17, 18}. The relaxation time τ (the mean time an electron travels before suffering a collision) was taken to be a constant throughout the metal and related to the electron mean free path by $l = v_F \cdot \tau$.

The Landau-Lifshitz equation of motion¹⁹ was used to describe the metal's magnetization vector. Only torques due to magnetocrystalline anisotropy, Gilbert damping, and the demagnetizing field were included. Torques due to exchange, diffusion, and magnetoelastic coupling were ignored, their effects being negligible compared to the magnetic damping in pure Nickel at low temperatures and 24 GHz incident radiation¹. Note however, that the methods we present to calculate the transmission can be readily extended to include these additional torques.

In the perpendicular configuration, the transmission calculations are considerably simplified by the use of circularly polarized coordinates to describe the rf electromagnetic fields in the slab. Further, we need only calculate the transmission of circularly polarized incident radiation through a slab surrounded by vacuum. The transmission

of arbitrarily polarized radiation through a slab surrounded by any kind of dielectric may be obtained by linear combination of the circularly polarized solutions²⁰. (see chapter 2, section 2.5).

Formal solutions for the transmission of circularly polarized radiation through finite slabs of non-magnetic metal have been known for some time. Platzmann and Buchsbaum²¹ solved the problem for specular surface scattering in 1963 while Baraff²² presented one analytic solution for the case of diffuse surface scattering in 1968 and another²³ in 1973. These solutions have proven to be very useful for examining limiting transmission cases (as Kogan, Turov, and Ustinov¹⁵ did when they extended Platzmann and Buchsbaum's method to a ferromagnet) and for deriving simple physical arguments to explain the various ASE transmission features observed in non-magnetic metals (see, for example, Baraff's analysis of his first diffuse scattering solution²⁴ and his comparison with experiment²⁵). Interestingly enough, Baraff found that the microwave transmission through a non-magnetic metal was strongly dependent on the type of surface scattering at the slab faces^{23, 24}. This result suggests that the calculated transmission through a ferromagnetic metal should also depend on whether the surface scattering was specular or diffuse.

However, the formal solutions are not well suited to general calculational work. The specular scattering solution of Platzmann and Buchsbaum²¹ for the transmission is expressed as

an infinite sum. The sum converges very slowly unless $d/\delta \leq 1$. Baraff obtained iterative solutions for the diffuse scattering case. The first method²² converges like $\exp(-d/l)$ and is very difficult to work with if more than one iteration is carried out. This makes the method unsuitable for experimentally interesting cases where $d/l < 1$ unless a low accuracy solution is acceptable. The second method²³ is based on multiple reflections of conduction electrons in the slab and requires considerable numerical work to repeatedly evaluate several complex integrals. Finally, there is the problem that none of the three methods are suitable for calculating the rf electric field distribution in the slab. These distributions are very useful for determining the source of various transmission features.

In order to carry out microwave transmission calculations in all skin effect regimes we had to develop several new methods for calculating the transmission through the slab and the rf field distributions in the slab valid for any δ/l ratio and slab thickness d . The infinite sum solution of Platzmann and Buchsbaum²¹ has been recast into two new forms. One is a much faster converging series solution suitable for calculating the internal rf field distributions and the transmission through the slab. The other is an integral form suitable for very fast calculation of the transmission only. See chapter 6 for details.

The complex iterative schemes of Baraff^{22, 23} for diffuse scattering have been replaced by a brute-force numerical method that simultaneously calculates the electric field distribution across the slab and the transmission through the slab. This method is easy to implement and valid for any δ/l ratio and slab thickness d . See chapter 5.

The results of our calculations may be summed up with the two diagrams shown in figure 2. The logarithm of the electric field amplitude in a 5 μm thick slab is plotted against depth z in the slab and against external magnetic field H_0 . The mean free path l was 25 μm , making $\delta/l \ll 1$ (well within the extreme ASE regime). 24 GHz, negative circularly polarized, microwaves were assumed to fall on the $z = 0$ slab face at normal incidence. One diagram was calculated for specular surface scattering and the other was calculated for diffuse surface scattering.

The front surface skin layers[†] are clearly visible on the two plots and remarkably similar in structure. Note how the rf skin depth δ goes through a maximum near $H_0 = 12.14$ kOe (the magnetic field value corresponding to FMAR) and a minimum at a value of $H_0 = 18.55$ kOe (the magnetic field value corresponding to FMR). This behaviour is also predicted by the room temperature theory¹ (see chapter 4). The fields in the bulk and at the rear of the slab definitely depend on the type of surface

[†] The skin layer and the skin depth δ both refer to the distance into the slab over which the rf electric field has appreciable amplitude. In figure 2 we can see that the skin layer in our 5 μm slab is the order of 1 μm .

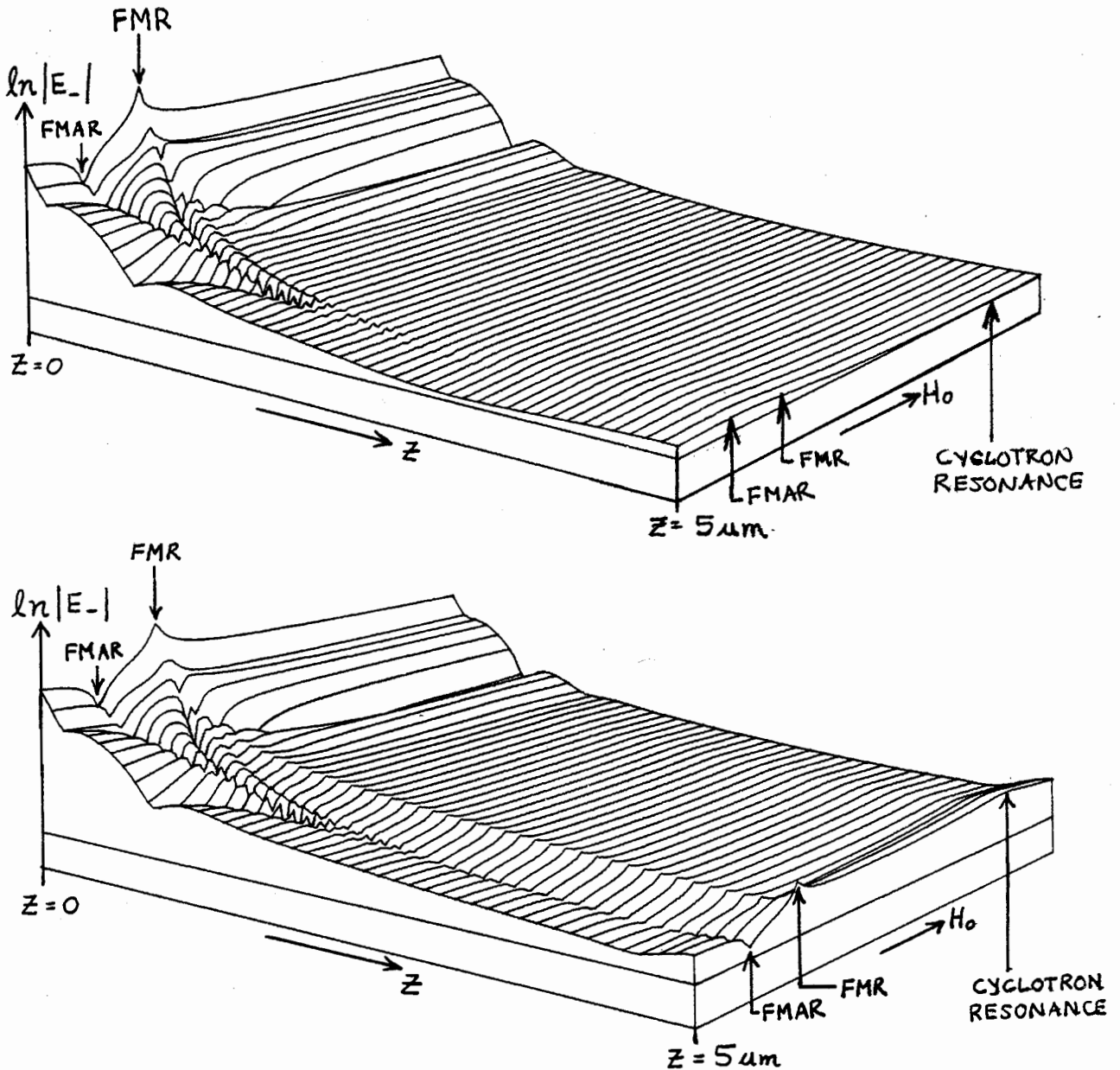


Fig. 2 Logarithm of the negative circularly polarized electric field amplitude in a $5\ \mu\text{m}$ thick slab plotted against depth z in the slab and applied magnetic field H_0 . The electron mean free path was taken to be $l = 25\ \mu\text{m}$. The parameters used in the calculation are listed in Appendix A.

scattering. In figure 2 we see that the electric field distribution calculated for specular surface scattering exhibits only a weak dependence on H_0 , going through a maximum near FMAR and a broad minimum at a value of $H_0 = 49.2$ kOe corresponding to cyclotron resonance of the conduction electrons. On the other hand we see that the electric field distribution calculated for diffuse surface scattering goes through a minimum at FMAR, a maximum at FMR, and yet another, weaker maximum at cyclotron resonance. Further, all magnetic field dependent electric field features increase in magnitude towards the rear of the slab.

In figure 2 the electric field at $z = d$ is proportional to the transmitted signal amplitude. One can therefore see that the transmission for specular scattering will be relatively featureless except for a broad FMAR peak and a minimum at cyclotron resonance. No interesting features can be seen at FMR. This is in general agreement with the predictions of Kogan, Turov, and Ustinov¹⁵ (we cannot predict the behaviour at cyclotron resonance from their theory because they ignored orbital effects). In contrast, the transmission calculated for diffuse surface scattering goes through a minimum at FMAR, a strong maximum at FMR, and another maximum at cyclotron resonance. This is more like the results of Cochran and Heinrich¹³ in their parallel configuration calculations.

The general behaviour of the electric field distributions shown in figure 2 has a simple physical explanation. In the anomalous skin effect regime, the electric fields generated in

the skin layer are mainly due to shielding electrons that run more or less parallel to the $z = 0$ slab face and therefore the electric field distribution near the front of the slab is relatively unaffected by the surface scattering conditions. However, the electric fields in the bulk are mainly due to electrons that enter the skin layer, scatter off the $z = 0$ face, and head back into the slab after picking up energy from the driving field. These electrons are indeed affected by the surface scattering. We should therefore not be too surprised that the electric field distributions in the bulk of the metal are different for specular and diffuse surface scattering. In fact, Baraff²³ explicitly demonstrated that the transmission peak at cyclotron resonance for diffuse surface scattering, and the transmission minimum at cyclotron resonance for specular scattering²⁴, could be directly attributed to the type of surface scattering at the rear of the slab.

This thesis is organized as follows. In chapter 2 we derive the boundary value problem that describes the electric field distribution in the slab when the current density is non-locally related to the electric field. In chapter 3 we calculate semi-classically the current kernels associated with our problem using the method of Cohen, Harrison, and Harrison²⁶ to solve the Boltzmann transport equation. In chapter 4 we solve the boundary value problem assuming $\delta/l \gg 1$ (the NSE regime) and review the predictions of the room temperature theory. Chapter 5 carries out the numerical solution for the

boundary value problem assuming diffuse scattering at the slab faces. Chapter 6 considers both numerical and analytic solutions for the electric field in the slab when the surfaces specularly scatter the conduction electrons. In chapter 7 we present the results of our calculations and discuss their significance.

2. THE ELECTRIC FIELD IN THE SLAB

2.1 Introduction

Calculating the transmission through a slab of metal entails determining the rf electric field distribution $\vec{E}(\vec{r})$ in the slab. In this chapter we formulate the perpendicular configuration boundary value problem for $\vec{E}(\vec{r})$ when the current density $\vec{j}(\vec{r})$ is non-locally related to $\vec{E}(\vec{r})$.

In section 2.2 we write down Maxwell's equations for our geometry. The constitutive equation linking the induction field $\vec{B}(\vec{r})$ to the magnetic field $\vec{H}(\vec{r})$ is considered in section 2.3 while the constitutive relation between $\vec{j}(\vec{r})$ and $\vec{E}(\vec{r})$ is considered in section 2.4. In section 2.5, Maxwell's equations and the constitutive relations are combined to form a second order integrodifferential equation for $\vec{E}(\vec{r})$. We impose boundary conditions on the solutions that allow us to calculate (i) the transmission of circularly polarized radiation through a slab surrounded by free space and (ii) the transmission of linearly polarized radiation through a slab surrounded by an anisotropic space. The latter case corresponding to the experimental situation. Finally, in sections 2.6, there is a chapter summary.

We should point out that each part of the problem is discussed in considerable detail. A reader who is familiar with the transmission boundary value problem may find it useful to skip to the chapter summary in section 2.6 and refer back to the material in the rest of the chapter for the details.

2.2 Maxwell's Equations in the Perpendicular Configuration

We start by writing down Maxwell's equations in Gaussian units:

$$\nabla \times \bar{\mathbf{E}}(\bar{\mathbf{r}}, t) = -\partial \bar{\mathbf{B}}(\bar{\mathbf{r}}, t) / \partial t \quad [2.1]$$

$$\nabla \times \bar{\mathbf{H}}(\bar{\mathbf{r}}, t) = (4\pi/c) \bar{\mathbf{j}}(\bar{\mathbf{r}}, t) + (1/c) \partial \bar{\mathbf{D}}(\bar{\mathbf{r}}, t) / \partial t \quad [2.2]$$

$$\nabla \cdot \bar{\mathbf{D}}(\bar{\mathbf{r}}, t) = 4\pi\rho \quad [2.3]$$

$$\nabla \cdot \bar{\mathbf{B}}(\bar{\mathbf{r}}, t) = 0 \quad [2.4]$$

where $\bar{\mathbf{D}}(\bar{\mathbf{r}}, t)$ is the rf displacement field and ρ is the free charge density.

The geometry of the perpendicular configuration is shown in figure 3. The specimen is located in the space $0 \leq z \leq d$ and a d.c. magnetic field H_0 is directed along the z axis. Microwaves of frequency f (circular frequency $\omega = 2\pi f$) fall on the slab at normal incidence and give rise to a reflected and a transmitted

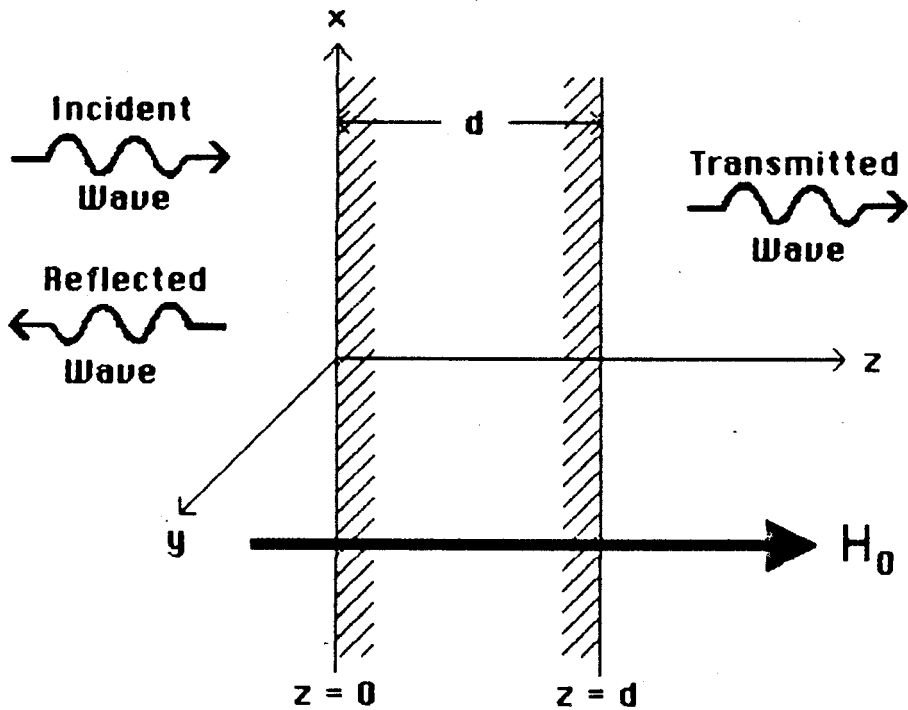


Fig. 3 The perpendicular configuration transmission geometry. A slab of metal is located between the planes $z = 0$ and $z = d$ and a uniform d.c. magnetic field H_0 is directed along the z axis. Microwave radiation is normally incident on the $z = 0$ slab face and a transmitted and a reflected wave are generated.

wave.

In this geometry, the rf fields generated in the slab will have a spatial variation in the z-direction only. If we take the time dependence of all quantities to be $\exp(-i\omega t)$ and neglect the displacement current in [2.2] compared with the real currents (an excellent approximation at microwave frequencies)³² then Maxwell's equations [2.1] - [2.2] may be reduced to

$$\partial E_x / \partial z = (i\omega/c) b_y \quad [2.5]$$

$$\partial E_y / \partial z = -(i\omega/c) b_x \quad [2.6]$$

$$\partial h_x / \partial z = (4\pi/c) j_y \quad [2.7]$$

$$\partial h_y / \partial z = -(4\pi/c) j_x \quad [2.8]$$

$$j_z = 0; \quad b_z = 0 \quad [2.9]$$

This is all the information we can get out of Maxwell's equations. To proceed further we must specify the constitutive relations linking \mathbf{B} to \mathbf{H} and \mathbf{j} to \mathbf{E} . This is done in sections 2.3 and 2.4. For our problem, the constitutive relations take on particularly simple forms in circularly polarized coordinates and not cartesian coordinates. In this new coordinate system, we decompose a transverse rf field vector into a pair of counter-rotating vectors rather than into two orthogonal

cartesian vectors. For example, if we were to look down the z axis (towards $z = -\infty$) at a transverse electric field vector $\bar{E}(\bar{r}, t) = \bar{E}(z)\exp(-i\omega t)$, instead of saying $\bar{E}(z)\exp(-i\omega t)$ was made up of the two cartesian components $E_x(z)\exp(-i\omega t)\hat{x}$ and $E_y(z)\exp(-i\omega t)\hat{y}$ we would say that it was composed of a circularly polarized vector $E_+(z)\exp(-i\omega t)\hat{e}_+$ rotating clockwise with an angular velocity of ω rad/sec. and a circularly polarized vector $E_-(z)\exp(-i\omega t)\hat{e}_-$ rotating counter-clockwise with an angular velocity of $-\omega$ rad/sec. Here, \hat{x} and \hat{y} are orthogonal unit vectors in the x and y directions, respectively, and \hat{e}_\pm are orthogonal circularly polarized basis vectors defined by:

$$\hat{e}_\pm = (\hat{x} \mp i\hat{y})/2 \quad [2.10]$$

The conversion of x and y cartesian field components to + and - circularly polarized field components is easy enough.

Using the results of Appendix B we write

$$E_{\pm} = E_x \pm iE_y \quad [2.13]$$

$$b_{\pm} = b_x \pm ib_y \quad [2.14]$$

$$h_{\pm} = h_x \pm ih_y \quad [2.15]$$

$$j_{\pm} = j_x \pm ij_y \quad [2.16]$$

It's important to note that there are several common ways of defining the circularly polarized basis vectors²⁷. Each definition leads to a slightly different set of relations between the cartesian and circularly polarized field components. Appendix B demonstrates how to arrive at the conversion formulae [2.13] - [2.16] for our particular choice of \hat{e}_{\pm} .

Maxwell's equations can be re-expressed in circularly polarized form by multiplying [2.6] and [2.8] by $\pm i$, adding them to [2.5] and [2.7] respectively, and then using [2.13]-[2.16]:

$$\partial E_{\pm} / \partial z = \pm (\omega/c) b_{\pm} \quad [2.17]$$

$$\partial h_{\pm} / \partial z = \mp (4\pi i/c) j_{\pm} \quad [2.18]$$

$$j_z = 0; \quad b_z = 0 \quad [2.19]$$

2.3 The Constitutive Relation Between \underline{B} and \underline{H}

The magnetic properties of the metal enter Maxwell's equations through the constitutive relation linking $\underline{B}(\underline{z})$ to $\underline{H}(\underline{z})$. In ferromagnetic metals, this relationship may be obtained from the Landau-Lifshitz equation of motion¹⁹ for the specimen's precessing magnetization vector \underline{M} . In Nickel, this equation can take the form¹

$$\partial \underline{M} / \partial t = -\gamma [\underline{M} \times \underline{H}] + (G/\gamma M_s^2) [\underline{M} \times \partial \underline{M} / \partial t] \quad [2.20]$$

$$\underline{H} = \underline{H}_0 - \underline{H}_d + \underline{H}_A + \underline{H}$$

$$\underline{M} = \underline{M}_s + \underline{m}$$

where \underline{H} is an effective magnetic field composed of the external field \underline{H}_0 , the demagnetizing field \underline{H}_d , a field \underline{H}_A associated with magnetocrystalline anisotropy, and the rf field \underline{H} . \underline{M} is the magnetization vector composed of the saturation magnetization \underline{M}_s and of the rf magnetization \underline{m} . The second term on the right hand side of [2.20] is a phenomenological damping term due to Gilbert³³. G is the damping parameter in sec^{-1} and $\gamma = g|e|/2mc$ is the spectroscopic splitting factor.

In general, there are additional effective magnetic fields in [2.20] due to exchange and diffusion torques^{28, 29, 30} acting

on \bar{M} . However in Nickel, at 24 GHz, the exchange and diffusion torques are negligible and can be ignored¹.

The solution of the Landau-Lifshitz equation [2.20] for \bar{m} in terms of \bar{H} is rather simple provided we assume that H_0 saturates the specimen (ie, pulls \bar{M} parallel to H_0), the [100] crystal direction lies along H_0 , and \bar{H} and \bar{m} are small compared to H_0 and M_S . In that case, we may write:

$$\bar{H} = (h_x, h_y, H_{\text{eff}}) \quad [2.21]$$

$$\bar{M} = (m_x, m_y, M_S) \quad [2.22]$$

where

$$H_{\text{eff}} = H_0 - H_d + H_A \quad [2.23]$$

$$H_d = 4\pi M_S \quad [2.24]$$

$$H_A = 2K_1/M_S \quad [2.25]$$

H_{eff} is the effective internal d.c. magnetic field, H_d is the demagnetizing field for a plane specimen unbounded in the x and y directions, H_A is the effective magnetocrystalline anisotropy field^{29,31} appropriate for a crystal whose [100] direction is along the z axis, and K_1 is the first anisotropy constant in ergs/cc, All fields are expressed in Oersteds.

Substituting [2.21] and [2.22] into [2.20], and assuming \bar{m} and \bar{H} have a time dependence of $\exp(-i\omega t)$, gives two equations

for m_x and m_y in terms of h_x and h_y

$$-i\omega m_x = -\gamma(m_y H_{\text{eff}} - h_y M_s) + i(\omega/\gamma)(G/M_s)m_y \quad [2.26]$$

$$-i\omega m_y = -\gamma(-m_x H_{\text{eff}} + h_x M_s) - i(\omega/\gamma)(G/M_s)m_x \quad [2.27]$$

and by [2.21] and [2.22], $h_z = 0$ and $m_z = 0$ to first order in m/M_s and h/H_0 . Equations [2.26] and [2.27] allow us to relate \bar{m} to \bar{h} through $\bar{m} = \tilde{\chi} \cdot \bar{h}$ where $\tilde{\chi}$ is the dynamic susceptibility tensor. The desired constitutive relation between \bar{B} and \bar{H} is determined by $\bar{B} = \bar{H} + 4\pi\bar{m}$ which we may write as

$$\bar{B}(\bar{r}) = \tilde{\mu} \cdot \bar{H}(\bar{r}) \quad [2.28]$$

$$\tilde{\mu} = 1 + 4\pi\tilde{\chi} \quad [2.29]$$

where $\tilde{\mu}$ is the dynamic permeability tensor.

In the perpendicular configuration, both $\tilde{\chi}$ and $\tilde{\mu}$ diagonalize in circularly polarized coordinates. To see this, multiply [2.27] by $\pm i$, add it to [2.26], and let $m_{\pm} = m_x \pm im_y$. This results in the two independent equations:

$$[\pm H_{\text{eff}} + (\omega/\gamma) \mp i(\omega/\gamma)G/(\gamma M_s)]m_{\pm} = \pm M_s h_{\pm} \quad [2.30]$$

and the diagonal components of the susceptibility tensor $\tilde{\chi}$ are given by $\chi_{\pm} = m_{\pm}/h_{\pm}$ and $\chi_{zz} = 0$. By [2.29], the corresponding

diagonal components of the permeability tensor are just

$$\mu_{\pm} = 1 + 4\pi\chi_{\pm} \text{ and } \mu_{zz} = 1; \text{ ie,}$$

$$\mu_{\pm} = \frac{B_{\text{eff}} \pm \omega/\gamma - i(\omega/\gamma)(G/\gamma M_S)}{H_{\text{eff}} \pm \omega/\gamma - i(\omega/\gamma)(G/\gamma M_S)} \quad [2.31]$$

$$\mu_{zz} = 1 \quad [2.32]$$

where

$$B_{\text{eff}} = H_{\text{eff}} + 4\pi M_S \quad [2.33]$$

is the effective d.c. induction field in Oersteds.

The magnetic constitutive equations for our problem are therefore

$$b_{\pm}(z) = \mu_{\pm} h_{\pm}(z) \quad [2.34]$$

and, by [2.19] and [2.32], $b_z(z) = h_z(z) = 0$.

A few comments are in order about the circularly polarized permeabilities μ_{\pm} . First of all, the specimen must be saturated for the permeabilities [2.31] to be valid. This requires H_{eff} to be positive (ie, to lie along H_0) or, by [2.23],

$$H_0 > H_d - H_A = 4\pi M_S - 2K_1/M_S \quad [2.35]$$

Using the parameters listed in Appendix A we find

$4\pi M_s = 6.410$ kOe and $2K_1/M_s = -4.313$ kOe. In the perpendicular configuration, the saturation condition for Nickel is therefore $H_0 > 10.72$ kOe.

Next, from [2.31], we see that only the negative polarization is magnetically active. At one value of H_0 the numerator of μ_- becomes small, and hence so does μ_- ; this field is defined by

$$B_{\text{eff}} = \omega/\gamma \quad (\text{FMAR}) \quad [2.36]$$

and corresponds to FMAR. At a larger field value the denominator of μ_- becomes small and μ_- becomes large; this field is defined by

$$H_{\text{eff}} = \omega/\gamma \quad (\text{FMR}) \quad [2.37]$$

and corresponds to FMR. In contrast, μ_+ exhibits only a monotonic variation with H_0 ; the positive polarization is magnetically inactive.

Using the definitions for B_{eff} and H_{eff} , the conditions for

FMAR and FMR in the perpendicular configuration become:

$$H_0 = \omega/\gamma - 2K_1/M_S \quad (\text{FMAR}) \quad [2.38]$$

$$H_0 = \omega/\gamma + 4\pi M_S - 2K_1/M_S \quad (\text{FMR}) \quad [2.39]$$

From Appendix A we see that $\omega/\gamma = 7.827$ kOe in Nickel (at 24 GHz) and since $2K_1/M_S = -4.313$ kOe FMAR will occur at $H_0 = 12.1$ kOe and FMR will occur at $H_0 = 18.5$ kOe.

2.4 The Constitutive Relation Between \vec{j} and \vec{E}

The electronic properties of the metal enter through the constitutive relation linking $\vec{j}(z)$ to $\vec{E}(z)$. According to the semi-classical theory of conduction, the current density generated at a point \vec{r} in a metal is entirely determined by the action of the electric field on each electron reaching \vec{r} since it's last collision. This last collision occurs, on average, within a distance of one electron mean free path l from \vec{r} . In the normal skin effect (NSE) regime, where $\delta/l \gg 1$, conduction electrons are acted upon by essentially a constant electric field between collisions. We may therefore calculate $\vec{j}(\vec{r})$, the current density at \vec{r} , assuming the electric field throughout the metal to be equal to $\vec{E}(\vec{r})$; ie, we can relate $\vec{j}(\vec{r})$ to $\vec{E}(\vec{r})$ locally through Ohm's Law (equation [1.1]).

However, in the anomalous skin effect (ASE) regime, characterized by $\delta/l \leq 1$, the electric field is not constant

over the distance l . Ohms's Law is no longer valid and $\vec{j}(\vec{r})$ now depends non-locally on the rf electric field throughout a region of mean radius l about \vec{r} . This more general constitutive relation can be written as¹⁰:

$$\vec{j}(\vec{r}) = \int_{\Omega} \tilde{\kappa}(\vec{r}, \vec{\xi}) \cdot \vec{E}(\vec{\xi}) d\vec{\xi} \quad [1.2]$$

where the integral extends over the volume Ω of the metal. As mentioned in chapter 1, $\tilde{\kappa}(\vec{r}, \vec{\xi})$ is called the current kernel. Formally, the kernel is a Green's function that gives the rf current density at a point \vec{r} in the metal due to a delta function rf electric field at $\vec{\xi}$. Weighting $\tilde{\kappa}(\vec{r}, \vec{\xi})$ with the rf electric field at $\vec{\xi}$ and then integrating over $\vec{\xi}$ yields the net current density at \vec{r} . Physically, the kernel represents all the microscopic aspects of our problem, such as the form of the electron trajectories and the nature of the electron scattering processes.

The geometry of the perpendicular configuration, and the cylindrical symmetry of our metal's spherical Fermi Surface, considerably simplifies the non-local current density [1.2]. Specifically, all rf fields vary spatially in the z direction only and the symmetry of the Fermi surface prevents electric fields in the x and y directions from contributing to the current density in the z direction. Since $j_z = 0$ by [2.9] then it follows that $E_z = 0$ and the transverse components of $\vec{j}(z)$ may

be written as

$$j_x(z) = \int_0^d [K_{xx}(z, \xi)E_x(\xi) + K_{xy}(z, \xi)E_y(\xi)]d\xi \quad [2.40]$$

$$j_y(z) = \int_0^d [K_{yx}(z, \xi)E_x(\xi) + K_{yy}(z, \xi)E_y(\xi)]d\xi \quad [2.41]$$

where the $K_{ij}(z, \xi)$ ($i, j = x, y$) are the transverse components of the cartesian current kernel $\tilde{\kappa}(\vec{r}, \vec{\xi})$. This kernel tensor diagonalizes in circularly polarized coordinates. Referring to figure 4, it's not too hard to see that the Fermi surface's symmetry about the z axis leads to the the relationships

$$K_{xx}(z, \xi) = K_{yy}(z, \xi) \quad [2.42]$$

$$K_{yx}(z, \xi) = -K_{xy}(z, \xi) \quad [2.43]$$

If we use [2.42] in [2.41] and [2.43] in [2.40], then multiply [2.41] by $\pm i$ and add it to [2.40] we get the circularly polarized current densities

$$j_{\pm}(z) = \int_0^d K_{\pm}(z, \xi)E_{\pm}(\xi)d\xi \quad [2.44]$$

where we have defined the circularly polarized current kernels $K_{\pm}(z, \xi)$ by

$$K_{\pm}(z, \xi) = K_{xx}(z, \xi) \pm iK_{yx}(z, \xi) \quad [2.45]$$

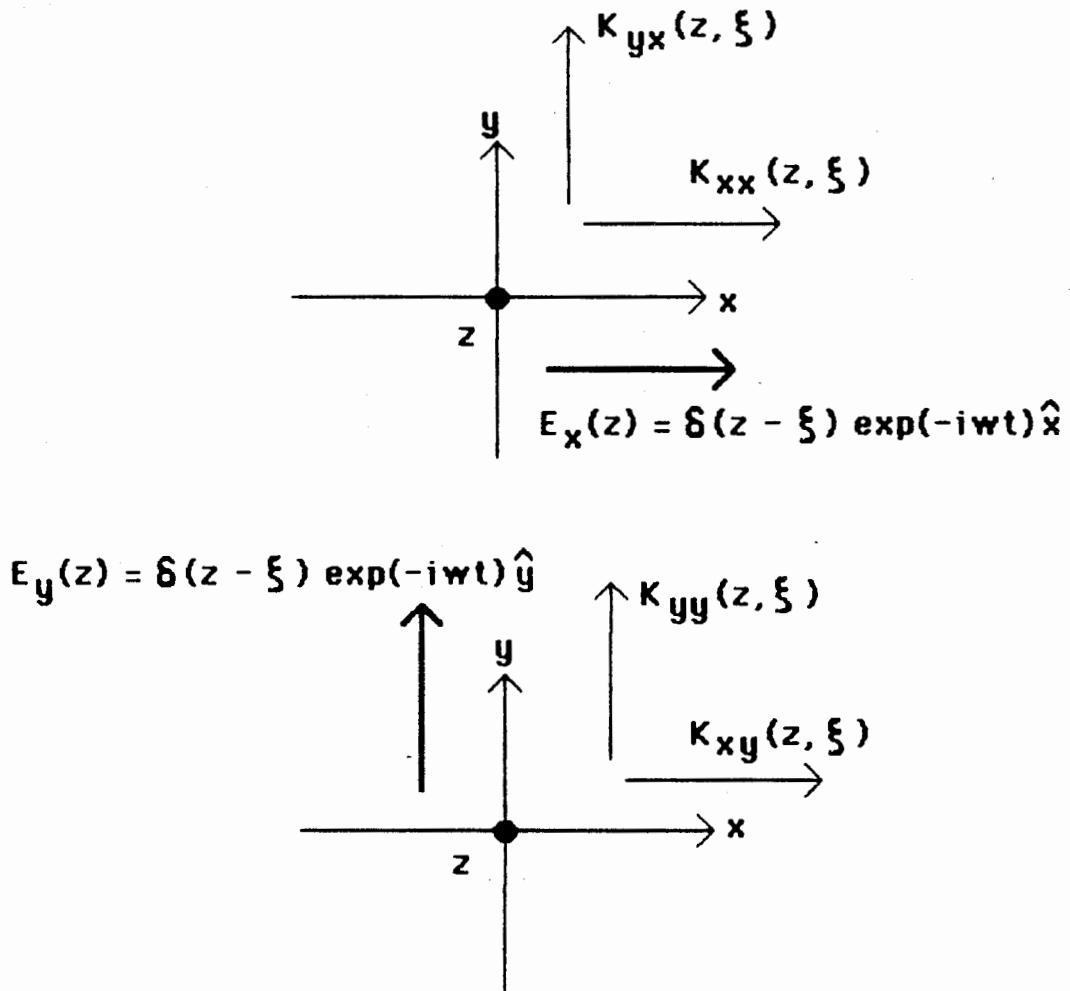


Fig. 4 Diagram showing the transverse current response in the slab pictured in figure 3 due to delta-function rf electric fields directed along the x and y axes. For a Fermi surface with cylindrical symmetry about the z axis we can see that the current densities generated by the electric fields will be related by $K_{xx}(z, \xi) = K_{yy}(z, \xi)$ and $K_{yx}(z, \xi) = -K_{xy}(z, \xi)$.

The kernels $K_{\pm}(z, \xi)$ for our problem are calculated in chapter 3.

2.5 The Boundary Value Problem

Combining the circularly polarized Maxwell's equations [2.17]-[2.18] with the constitutive relations [2.34] and [2.44] yields two independent, second order, integro-differential equations for the rf electric fields $E_{+}(z)$ and $E_{-}(z)$; ie,

$$\partial E_{\pm} / \partial z = \pm(\omega/c) b_{\pm} \quad [2.17]$$

$$\partial h_{\pm} / \partial z = \mp(4\pi i/c) j_{\pm} \quad [2.18]$$

$$b_{\pm}(z) = \mu_{\pm} h_{\pm}(z) \quad [2.34]$$

$$j_{\pm}(z) = \int_0^d K_{\pm}(z, \xi) E_{\pm}(\xi) d\xi \quad [2.44]$$

combine to give

$$E_{\pm}''(z) + [2i\mu_{\pm}/(\sigma_0 \delta_0^2)] j_{\pm}(z) = 0 \quad [2.46]$$

$$j_{\pm}(z) = \int_0^d K_{\pm}(z, \xi) E_{\pm}(\xi) d\xi \quad [2.44]$$

where we have written $4\pi i \omega \mu_{\pm} / c^2 = [2i\mu_{\pm}/(\sigma_0 \delta_0^2)]$ and used a

prime (') to denote differentiation with respect to z . The quantity $\delta_0 = c/(2\pi\omega\sigma_0)^{1/2}$ is the classical rf skin depth for a nonmagnetic metal ($\mu_{\pm} = 1$). The skin depth is a measure of how far an incident electromagnetic wave can propagate into a metal before suffering appreciable attenuation. In a good conductor, at room temperatures and microwave frequencies, δ_0 is the order of $1 \mu\text{m}$ (see chapter 4).

We now consider what boundary conditions to impose on the solutions of [2.46] at the $z = 0$ and $z = d$ slab faces. In this thesis we shall be concerned with calculating the transmission through the slab for two important special cases:

- (I) A slab surrounded by free space and irradiated at normal incidence by a circularly polarized wave of frequency $f = \omega/2\pi$.
- (II) A slab surrounded by an anisotropic space and irradiated at normal incidence by a linearly polarized wave of frequency $f = \omega/2\pi$.

In the perpendicular configuration, a positive (negative) circularly polarized incident wave will generate only positive (negative) circularly polarized transmitted and reflected waves. This considerably simplifies the interpretation of transmission features, particularly in our case where only the negative polarization is magnetically active (see section 2.3).

However, real transmission experiments are not carried out using circularly polarized microwaves propagating in free space. The specimen is usually clamped between two microwave cavities and rectangular waveguides are used to feed microwaves into one cavity and pass the signal transmitted into the other cavity on

to a detector³⁴. Such cavities and waveguides are designed to allow microwaves of only one specific linear polarization at a given frequency f to propagate; waves of other polarizations are attenuated. While this provides a convenient method of delivering microwaves of a specific frequency and linear polarization to the front surface of the slab it also means that we can only measure one linearly polarized component of the transmitted and reflected waves (in the perpendicular configuration the two waves are, in general, elliptically polarized). The transmission calculated for case (II) can be made to correspond to this experimental situation.

The boundary conditions associated with cases (I) and (II) are quite different from one another (see sections 2.5.1 and 2.5.2). Fortunately, we do not have to solve [2.46] for each new set of boundary conditions.

Consider the particularly simple set of boundary conditions

$$h_{\pm}(0) = 1; h_{\pm}(d) = 0 \quad [2.48]$$

which are very nearly the same as the boundary conditions corresponding to case (I) -- the transmission of a circularly polarized wave through a slab surrounded by free space (see section 2.5.1 and especially the discussion following equation [2.82]). Let the solutions of [2.46] that satisfies [2.48] be $G_{+}(z)$ and $G_{-}(z)$ or, for brevity, $G_{\pm}(z)$. These particular solutions have the interesting property that the electric fields

$E_{\pm}(z)$ satisfying [2.46] and arbitrary values of $h_{\pm}(0)$ and $h_{\pm}(d)$ can be written (see Appendix C)

$$E_{\pm}(z) = h_{\pm}(0)G_{\pm}(z) - h_{\pm}(d)G_{\pm}(d - z) \quad [2.51]$$

Hence, the solutions $G_{\pm}(z)$ can be used to solve any boundary value problem we might care to construct. In particular, we can use them to solve the transmission boundary value problems associated with the cases (I) and (II) discussed above.

2.5.1 BVP I: Circular Polarization, Free Space

The boundary value problem we wish to solve is shown in figure 5. The slab is surrounded by free space and the $z = 0$ face is irradiated at normal incidence by either a positive or a negative circularly polarized wave of amplitude h_{\pm}^0, E_{\pm}^0 . This gives rise to a reflected wave of amplitude h_{\pm}^R, E_{\pm}^R at the $z = 0$ slab face and a transmitted wave of amplitude h_{\pm}^T, E_{\pm}^T at the $z = d$ face. In the perpendicular configuration, there is no mixing of modes; that is, a positive (negative) circularly polarized wave can only excite positive (negative) circularly polarized fields and currents in the slab. Therefore, the transmitted and reflected waves will be positive (negative) circularly polarized.

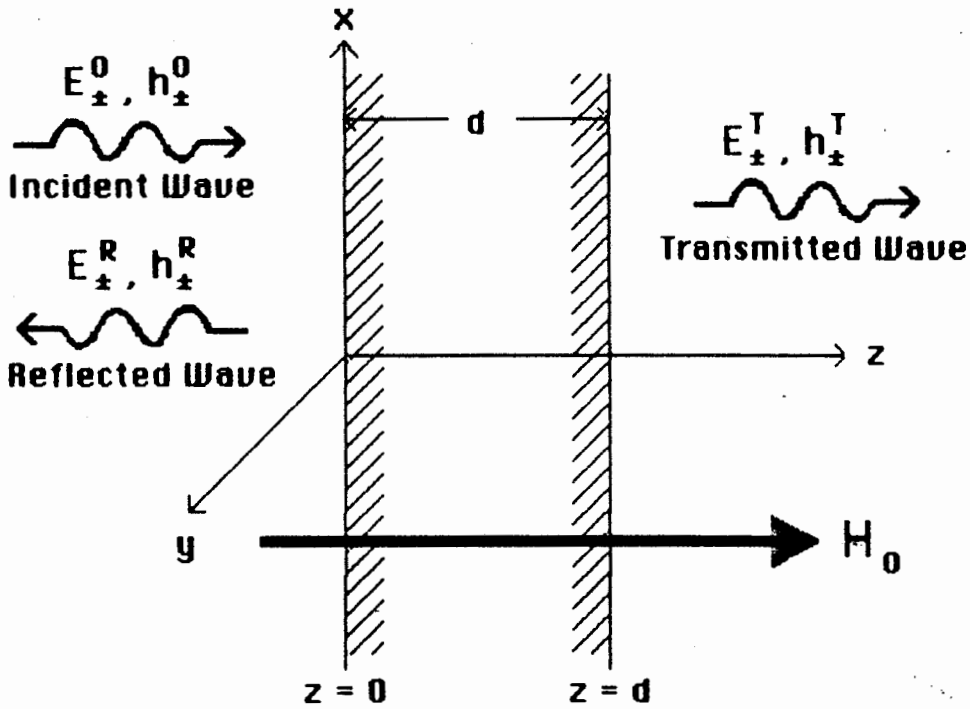


Fig. 5 The boundary value problem used to calculate the transmission of circularly polarized microwaves through a slab surrounded by vacuum. A circularly polarized wave is normally incident on the $z = 0$ slab face generating a reflected wave and a transmitted wave.

Now, from figure 5 we can see that the electric and magnetic fields just outside the slab are given by

$$h_{\pm}(0) = h_{\pm}^0 + h_{\pm}^R \quad [2.52]$$

$$E_{\pm}(0) = E_{\pm}^0 + E_{\pm}^R \quad [2.53]$$

$$h_{\pm}(d) = h_{\pm}^T \quad [2.54]$$

$$E_{\pm}(d) = E_{\pm}^T \quad [2.55]$$

We can relate the electric field amplitudes to the magnetic field amplitudes. From [2.1]-[2.2], and the relations [2.13]-[2.16], we get Maxwell's equations for free space

$$\partial E_{\pm} / \partial z = \pm (\omega/c) h_{\pm} \quad [2.56]$$

$$\partial h_{\pm} / \partial z = \mp (\omega/c) E_{\pm} \quad [2.57]$$

$$\partial^2 E_{\pm} / \partial z^2 + k_0^2 E_{\pm} = 0 \quad [2.58]$$

where, $k_0^2 = (\omega/c)^2 \quad [2.59]$

Waves propagating in free space in the +z direction will

therefore have a harmonic dependence of $\exp[i(k_0z - \omega t)]$ and their electric and magnetic field amplitudes will be related by

$$E_{\pm} = \mp i h_{\pm} \text{ (forward waves)}$$

Similarly, waves propagating in the $-z$ direction will have a dependence of $\exp[-i(k_0z + \omega t)]$ and

$$E_{\pm} = \pm i h_{\pm} \text{ (backward waves)}$$

Thus,

$$E_{\pm}^0/h_{\pm}^0 = Z_{\pm}^0 = \mp i \quad [2.60]$$

$$E_{\pm}^T/h_{\pm}^T = Z_{\pm}^0 = \mp i \quad [2.61]$$

$$E_{\pm}^R/h_{\pm}^R = -Z_{\pm}^0 = \pm i \quad [2.62]$$

where Z_{\pm}^0 is the circularly polarized wave impedance in free space.

Now, experimentally, one measures the transmission coefficients T_{\pm} and the reflection coefficients R_{\pm} defined by

$$T_{\pm} = h_{\pm}^T/h_{\pm}^0 \quad [2.63]$$

$$R_{\pm} = h_{\pm}^R/h_{\pm}^0 \quad [2.64]$$

If we take $h_{\pm}^0 = 1$ then $h_{\pm}^R = R_{\pm}$ and $h_{\pm}^T = T_{\pm}$. Using this convention, and [2.60]-[2.62], we can re-write [2.52]-[2.55] in terms of the transmission and reflection coefficients:

$$h_{\pm}(0) = 1 + R_{\pm} \quad [2.65]$$

$$E_{\pm}(0) = \mp i(1 - R_{\pm}) \quad [2.66]$$

$$h_{\pm}(d) = T_{\pm} \quad [2.67]$$

$$E_{\pm}(d) = \mp iT_{\pm} \quad [2.68]$$

Next, according to the general solution [2.51], the electric and magnetic fields just inside the slab are given by

$$E_{\pm}(0) = h_{\pm}(0)G_{\pm}(0) - h_{\pm}(d)G_{\pm}(d) \quad [2.69]$$

$$E_{\pm}(d) = h_{\pm}(0)G_{\pm}(d) - h_{\pm}(d)G_{\pm}(0) \quad [2.70]$$

The continuity of the transverse fields $E_{\pm}(z)$ and $h_{\pm}(z)$ across the slab faces allows us to substitute [2.52], [2.66], [2.54], and [2.68] into [2.69] and [2.70] to get two simultaneous equations for R_{+} and T_{+} and two simultaneous equations for R_{-} and T_{-} in terms of the known quantities $G_{\pm}(0)$

and $G_{\pm}(d)$

$$[1 \pm iG_{\pm}(0)]R_{\pm} + [\mp iG_{\pm}(d)]T_{\pm} = [1 \mp iG_{\pm}(0)] \quad [2.71]$$

$$[\mp iG_{\pm}(d)]R_{\pm} + [1 \pm iG_{\pm}(0)]T_{\pm} = [\pm iG_{\pm}(d)] \quad [2.72]$$

The solutions of these equations are

$$T_{\pm} = \frac{\pm 2iG_{\pm}(d)}{[1 \pm iG_{\pm}(0)]^2 + G_{\pm}^2(d)} \quad [2.73]$$

$$R_{\pm} = \frac{[1 \mp iG_{\pm}(0)][1 \pm iG_{\pm}(0)] - G_{\pm}^2(d)}{[1 \pm iG_{\pm}(0)]^2 + G_{\pm}^2(d)} \quad [2.74]$$

We can simplify these solutions. Cochran has shown²⁰ that if our slab is several times thicker than the skin depth δ , and if the free space wavelength λ of the incident radiation is much greater than δ , then one can, to a good approximation, neglect products of two or more of the $G_{\pm}(0)$ and $G_{\pm}(d)$ (Our calculations for Nickel at 24 GHz have shown that $|G_{\pm}(0)| \leq 10^{-3}$ and $|G_{\pm}(d)| \ll |G_{\pm}(0)|$ as long as $d/\delta \geq 2$ or 3). With this in mind,

the exact solutions [2.73] and [2.74] reduce to

$$T_{\pm} \approx \pm 2iG_{\pm}(d) \quad [2.75]$$

$$R_{\pm} \approx \frac{[1 \mp iG_{\pm}(0)]}{[1 \pm iG_{\pm}(0)]} \\ \approx 1 \mp 2iG_{\pm}(0) \quad [2.76]$$

Since $|G_{\pm}(0)|$ and $|G_{\pm}(d)|$ are both less than 10^{-3} in our problem, the approximate expressions [2.75] and [2.76] are accurate to one part in a thousand.

From [2.76] we see that $R_{\pm} \approx 1$ (ie, the metal surface at $z = 0$ reflects nearly all of the incident wave). Experimentally one measures the difference between R_{\pm} and 1. One such measure of this difference is the surface impedance z_{\pm}^S defined by

$$z_{\pm}^S = E_{\pm}(0)/h_{\pm}(0) \quad [2.77]$$

Using [2.66] and [2.65] we get

$$z_{\pm}^S = \mp i(1 - R_{\pm})/(1 + R_{\pm}) \quad [2.78]$$

and if we substitute either form of R_{\pm} given by [2.76] into

[2.78] we get:

$$z_{\pm}^S = G_{\pm}(0) \quad [2.79]$$

This result may also be obtained directly from [2.69] since we can ignore the product of $h_{\pm}(d)G_{\pm}(d)$ in comparison with $h_{\pm}(0)G_{\pm}(0)$ (see [2.80] and [2.81] below).

The electric field distribution in the slab is found by substituting [2.76] into [2.52], [2.75] into [2.54], and then inserting the resulting expressions into [2.51]:

$$h_{\pm}(0) \approx 2[1 \mp iG_{\pm}(0)] \approx 2 \quad [2.80]$$

$$h_{\pm}(d) \approx \pm 2iG_{\pm}(d) \quad [2.81]$$

$$E_{\pm}(z) \approx 2G_{\pm}(z) \quad [2.82]$$

We have two comments to make about the results of this section.

First, we see that the values of $G_{\pm}(0)$ and $G_{\pm}(d)$ completely specify the experimentally measureable surface impedances $z_{\pm}^S = G_{\pm}(0)$ and transmission coefficients $T_{\pm} \approx \pm 2iG_{\pm}(d)$. It should be noted that it is also common to discuss the results of a transmission calculation in terms of the "transmission impedance", z_{\pm}^T , defined in a manner analagous to the surface impedance:

$$z_{\pm}^T = E_{\pm}(d)/h_{\pm}(0) \quad [2.83]$$

which, by [2.82] and [2.80], is just $G_{\pm}(d)$.

Second, we see from [2.80] and [2.81] that the boundary conditions appropriate for transmission into free space are very nearly equal to $h_{\pm}(0) = 2$ and $h_{\pm}(d) = 0$. This is the reason the functions $G_{\pm}(z)$, which satisfy the boundary conditions $h_{\pm}(0) = 1$, $h_{\pm}(d) = 0$ come so close to describing the actual electric fields [2.82] in the slab. The rapid variation of $h_{\pm}(z)$ across the slab is due to the tremendous mismatch between the impedance of free space and the impedance in the metal. In free space,

$|E_{\pm}/h_{\pm}| = 1$ (see [2.60]) while in the metal, $|E_{\pm}/h_{\pm}| \ll 1$. When a wave of unit amplitude is normally incident on the front of the slab, nearly all of the wave is reflected. By [2.66] and [2.65], this leads to $h_{\pm}(0) \approx 2$ and $E_{\pm}(0) \ll 1$. A small portion of the incident wave propagates through the slab and transmits out into free space at $z = d$. This requires $|E_{\pm}(d)/h_{\pm}(d)| = 1$. Since $E_{\pm}(0) \ll 1$, we must have $E_{\pm}(d) \ll 1$ and $h_{\pm}(d) \ll 1$. This leads directly to the approximate boundary conditions $h_{\pm}(0) = 2$ and $h_{\pm}(d) = 0$.

2.5.2 BVP II: Linear Polarization, Anisotropic Space

We now wish to solve the boundary value problem shown in figure 6. The slab is surrounded by an anisotropic medium and irradiated at normal incidence by a linearly polarized wave of amplitude h_y^0, E_x^0 . In general, there will be two orthogonal, linearly polarized transmitted waves and, similarly, two reflected waves (ie, the net transmitted and reflected waves are elliptically polarized). See figure 6.

In an anisotropic medium the impedance of a given wave depends on the wave's polarization. For our case, we shall assume that in the medium occupying the half space $-\infty < z \leq 0$, the wave impedances of waves propagating in the +z direction, and corresponding to the orthogonal polarizations shown in figure 6, are given by

$$E_x/h_y = Z_0$$

$$-E_y/h_x = Z_1$$

(forward propagating waves in the space $-\infty < z \leq 0$)

where Z_0 and Z_1 are, in general, complex numbers. Similarly, in the space $d \leq z < \infty$, we shall assume that the wave impedances of the waves propagating in the +z direction, and corresponding to the orthogonal polarizations shown in figure 6, are given by

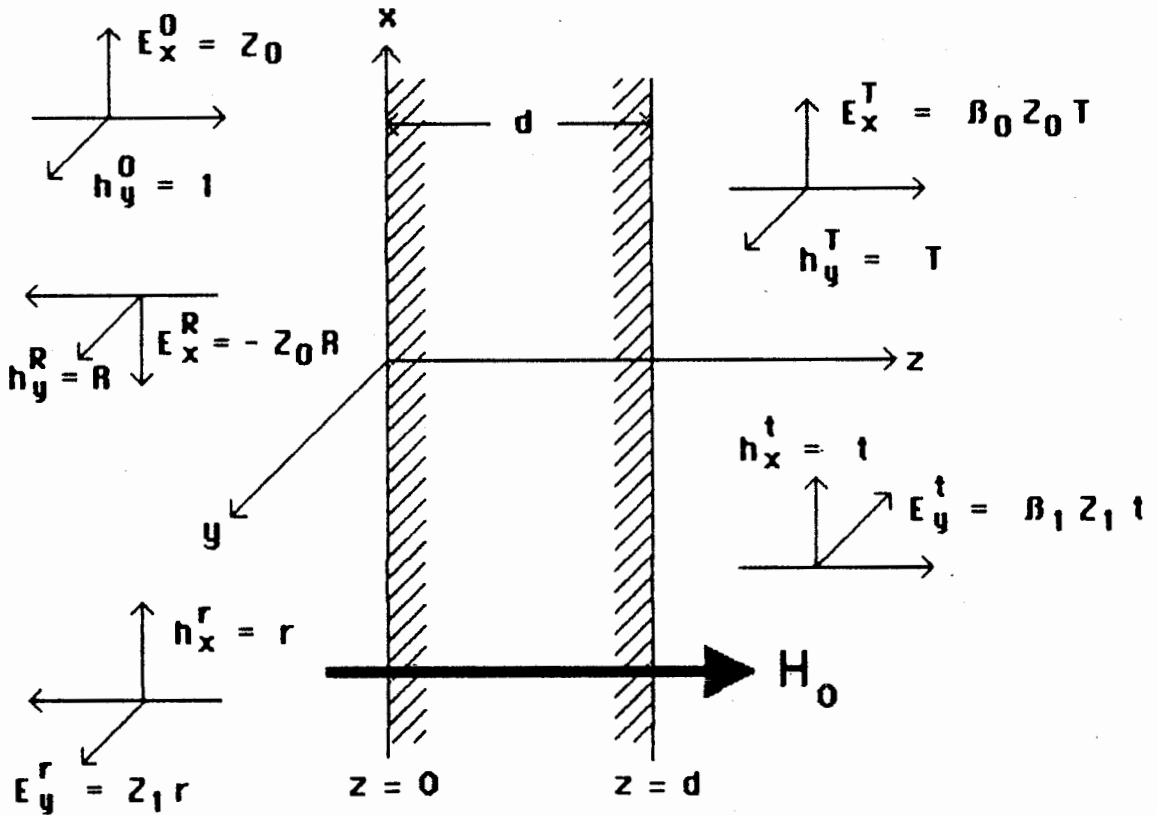


Fig. 6 The boundary value problem used to calculate the transmission of linearly polarized microwaves through a slab surrounded by an anisotropic medium. A Linearly polarized wave is normally incident on the $z = 0$ slab face generating a pair of orthogonal reflected waves and a pair of orthogonal transmitted waves.

$$E_x/h_y = \beta_0 Z_0$$

$$-E_y/h_x = \beta_1 Z_1$$

(forward propagating waves in the space $d \leq z < \infty$)

where β_0 and β_1 are also, in general, complex numbers.

We have written the wave impedances in this form for two reasons. First, we can recover the case of a slab surrounded by free space simply by setting $Z_0 = Z_1 = 1$ and $\beta_0 = \beta_1 = 1$. Second, to model an actual transmission experiment (where the waves propagate in rectangular waveguides) we need only replace Z_0 with the impedance of the waveguide's propagating polarization and Z_1 with the impedance of the waveguide's non-propagating polarization. Also, in order to account for transmission into a resonant microwave cavity, we equate β_0 and β_1 with the cavity amplitude factors. Cochran, Heinrich, and Dewar³⁴ have discussed how to calculate the values of Z_0 , Z_1 , β_0 , and β_1 . These authors found that a set-up that measures the transmission of 24 GHz radiation through thin slabs used to form a common end wall between two microwave cavities could be described by $Z_0 = 1.23$, $Z_1 = -5i$, $\beta_0 = 2.32 \times 10^{-2}$, and $\beta_1 = 1$.

To solve the linearly polarized boundary value problem posed in figure 6 we proceed in much the same way as we did in section 2.5.1. We start by defining the experimentally measurable reflection and transmission coefficients

R, r, T, and t:

$$h_y^R/h_y^0 = R \quad [2.84]$$

$$h_x^r/h_y^0 = r \quad [2.85]$$

$$h_y^T/h_y^0 = T \quad [2.86]$$

$$h_x^t/h_y^0 = t \quad [2.87]$$

We then assume $h_y^0 = 1$ and write down the net electric and magnetic fields just outside the slab faces in terms of the reflection and transmission coefficients and the wave impedances. Referring to figure 6 we find:

$$h_x(0) = r; \quad h_y(0) = 1 + R \quad [2.88]$$

$$E_x(0) = Z_0(1 - R); \quad E_y(0) = Z_1 r \quad [2.89]$$

$$h_x(d) = t; \quad h_y(d) = T \quad [2.90]$$

$$E_x(d) = \beta_0 Z_0 T; \quad E_y(d) = -\beta_1 Z_1 t \quad [2.91]$$

Next, using [2.13] and [2.15], we convert [2.88]-[2.91] to

circularly polarized form:

$$h_{\pm}(0) = r \pm i(1 + R) \quad [2.92]$$

$$E_{\pm}(0) = Z_0(1 - R) \pm iZ_1r \quad [2.93]$$

$$h_{\pm}(d) = t \pm iT \quad [2.94]$$

$$E_{\pm}(d) = \beta_0 Z_0 T \mp i\beta_1 Z_1 t \quad [2.95]$$

To obtain exact expressions for R , r , T , and t in terms of the known quantities $G_{\pm}(0)$ and $G_{\pm}(d)$ we substitute [2.92]-[2.95] into the general solutions

$$E_{\pm}(0) = h_{\pm}(0)G_{\pm}(0) - h_{\pm}(d)G_{\pm}(d) \quad [2.69]$$

$$E_{\pm}(d) = h_{\pm}(0)G_{\pm}(d) - h_{\pm}(d)G_{\pm}(0) \quad [2.70]$$

This results in four simultaneous equations for the four reflection and transmission coefficients. The solutions are extremely complicated and contain many terms. However, the solutions may be considerably simplified if we assume, as in section 2.5.1, that $|G_{\pm}(d)| \leq |G_{\pm}(0)| \ll 1$.

The simplification process is tedious and error prone. Fortunately, there is a much easier way to derive simplified forms for the reflection and transmission coefficients.

Equations [2.93] and [2.95] can be used to express the transmission and reflection coefficients in terms of the circularly polarized electric fields at $z = 0$ and $z = d$:

$$R = 1 - ([E_+(0) + E_-(0)] / 2Z_0) \quad [2.96]$$

$$r = [E_+(0) - E_-(0)] / (2iZ_1) \quad [2.97]$$

$$T = [E_+(d) + E_-(d)] / (2\beta_0 Z_0) \quad [2.98]$$

$$t = [E_-(d) - E_+(d)] / (2i\beta_1 Z_1) \quad [2.99]$$

Now, the electric fields $E_{\pm}(z)$ generated in the slab shown in figure 6 are due to a linearly polarized incident wave of unit magnetic field amplitude $h_y^0 = 1$. By $h_{\pm} = h_x \pm ih_y$ we see that this is equivalent to saying that the electric fields $E_{\pm}(z)$ were generated in the slab by two circularly polarized incident waves of magnetic field amplitudes $h_{\pm}^0 = \pm i$. But we know from section 2.5.1 that circularly polarized incident waves of amplitude $h_{\pm}^0 = 1$ generate electric fields $2G_{\pm}(z)$ (see [2.82]). Hence, the electric fields generated by incident waves of amplitude $h_{\pm}^0 = \pm i$ are just $E_{\pm}(z) = \pm 2iG_{\pm}(z)$. Using these

results in the approximate expressions [2.96]-[2.99] yields

$$R = 1 - (i[G_+(0) - G_-(0)]/Z_0) \quad [2.100]$$

$$r = [G_+(0) + G_-(0)]/(Z_1) \quad [2.101]$$

$$T = i[G_+(d) - G_-(d)]/(\beta_0 Z_0) \quad [2.102]$$

$$t = [G_+(d) + G_-(d)]/(\beta_1 Z_1) \quad [2.103]$$

and these are the same expressions that we worked out by simplifying the bulky exact expressions for R , r , T , and t (we will not be presenting the details of the tedious simplification process).

We can go even further. From equations [2.75] and [2.76] we have the circularly polarized transmission and reflection coefficients defined by

$$\pm 2iG_{\pm}(d) = T_{\pm}$$

$$\pm 2iG_{\pm}(0) = 1 - R_{\pm}$$

using these to eliminate $G_{\pm}(0)$ and $G_{\pm}(d)$ from [2.100]-[2.103] allows us to express the linearly polarized reflection and transmission coefficients in terms of the circularly polarized

coefficients:

$$R = (1 - 1/Z_0) + [R_+ + R_-]/(2Z_0) \quad [2.104]$$

$$r = [R_- - R_+]/(2iZ_1) \quad [2.105]$$

$$T = [T_+ + T_-]/(2\beta_0 Z_0) \quad [2.106]$$

$$t = [T_+ - T_-]/(2i\beta_1 Z_1) \quad [2.107]$$

2.6 Chapter Summary

A lot of material has been covered in this chapter and it's worthwhile to collect all the results in one place.

We have a metal with a spherical Fermi surface that magnetically resembles Nickel. We wish to calculate the microwave transmission through a slab of the material for the case where a d.c. magnetic field H_0 is normal to the plane of the slab (the perpendicular configuration) and the electron mean free path l in the metal is much greater than the rf skin depth δ . This requires us to calculate the rf electric field in the slab and to solve an appropriate transmission boundary value problem. The boundary value problem was formulated as follows:

Maxwell's Equations

In section 2.2 we found that the geometry of the perpendicular configuration reduced Maxwell's equations to

$$\partial E_{\pm} / \partial z = \pm(\omega/c) b_{\pm} \quad [2.17]$$

$$\partial h_{\pm} / \partial z = \mp(4\pi i/c) j_{\pm} \quad [2.18]$$

$$j_z = 0; b_z = 0 \quad [2.19]$$

where we have expressed the equations in circularly polarized coordinates (see Appendix B).

The Constitutive Relation between \vec{B} and \vec{H}

In section 2.3, the material equation linking b_{\pm} to h_{\pm} was derived from the Landau-Lifshitz equation of motion for the specimen's precessing magnetization vector \vec{M} . In Nickel, at 24 GHz, only torques due to H_0 , the demagnetizing field, magnetocrystalline anisotropy, and magnetic damping need to be included in the equation of motion. Torques due to exchange and diffusion are negligible and can be ignored. Assuming H_0 saturates the specimen, we found that the desired constitutive

relation between b_{\pm} and h_{\pm} could be written as

$$b_{\pm}(z) = \mu_{\pm} h_{\pm}(z) \quad [2.34]$$

where,

$$\mu_{\pm} = \frac{B_{\text{eff}} \pm \omega/\gamma - i(\omega/\gamma)(G/\gamma M_S)}{H_{\text{eff}} \pm \omega/\gamma - i(\omega/\gamma)(G/\gamma M_S)} \quad [2.31]$$

(all quantities in [2.31] are defined in section 2.3 and in Appendix A).

The Constitutive Relation between \vec{j} and \vec{E}

When the electron mean free path l exceeds the rf skin depth δ , the rf current density \vec{j} depends on the electric field distribution throughout the slab. If we assume that the metal's Fermi surface is cylindrically symmetric about the normal to the plane of the slab we found in section 2.4 that we could write the material equation linking j_{\pm} to E_{\pm} as

$$j_{\pm}(z) = \int_0^d K_{\pm}(z, \xi) E_{\pm}(\xi) d\xi \quad [2.44]$$

where the $K_{\pm}(z, \xi)$ are the circularly polarized kernels defined by

$$K_{\pm}(z, \xi) = K_{xx}(z, \xi) \pm iK_{yx}(z, \xi) \quad [2.45]$$

where the $K_{ij}(z, \xi)$ ($i, j = x, y$) represent the rf current density generated in the j th direction at a depth z in the slab due to a delta function rf electric field sheet in the i th direction at a depth ξ in the slab. The form that the kernels $K_{\pm}(z, \xi)$ take in our problem are discussed in chapter 3.

The Boundary Value Problem for \bar{E}

In section 2.5 we combined Maxwell's equations with the constitutive relations to arrive at the following boundary value problem for $E_{\pm}(z)$:

$$E_{\pm}''(z) + [2i\mu_{\pm}/(\sigma_0 \delta_0^2)]j_{\pm}(z) = 0 \quad [2.46]$$

$$j_{\pm}(z) = \int_0^d K_{\pm}(z, \xi) E_{\pm}(\xi) d\xi \quad [2.44]$$

$$h_{\pm}(0) = 1; h_{\pm}(d) = 0 \quad [2.48]$$

where $\delta_0 = c/(2\pi\omega\sigma_0)^{1/2}$ is the classical rf skin depth for a nonmagnetic metal ($\mu_{\pm} = 1$).

We imposed the boundary conditions [2.48] because $G_{\pm}(z)$, the solutions of [2.46] which satisfy these boundary conditions, can be superposed to generate the electric field distributions $E_{\pm}(z)$ that satisfy arbitrary $h_{\pm}(0)$ and $h_{\pm}(d)$ (see Appendix C); viz,

$$E_{\pm}(z) = h_{\pm}(0)G_{\pm}(z) - h_{\pm}(d)G_{\pm}(d - z) \quad [2.51]$$

BVP I: Transmission of Circularly Polarized Radiation into Free Space

In section 2.5.1 we solved the boundary value problem corresponding to the transmission of a circularly polarized wave through a slab surrounded by free space (see figure 5). The circularly polarized transmission and reflection coefficients were found to be

$$T_{\pm} = h_{\pm}^T/h_{\pm}^0 \approx \pm 2iG_{\pm}(d) \quad [2.75]$$

$$R_{\pm} = h_{\pm}^R/h_{\pm}^0 \approx 1 \mp 2iG_{\pm}(0) \quad [2.76]$$

(provided that the slab was 2 or 3 times thicker than the rf skin depth δ -- see section 2.5.1, after equation [2.74]).

BVP II: Transmission of Linearly Polarized Radiation into an Anisotropic Space

In section 2.5.2 we solved the boundary value problem corresponding to the transmission of a linearly polarized wave through a slab surrounded by an anisotropic space

(see figure 6). This corresponds to the experimental situation where the microwaves are contained in rectangular waveguides. The linearly polarized transmission and reflection coefficients were found to be

$$R = h_y^R/h_y^0 = 1 - (i[G_+(0) - G_-(0)]/Z_0) \quad [2.100]$$

$$r = h_x^r/h_y^0 = [G_+(0) + G_-(0)]/(Z_1) \quad [2.101]$$

$$T = h_y^T/h_y^0 = i[G_+(d) - G_-(d)]/(\beta_0 Z_0) \quad [2.102]$$

$$t = h_x^t/h_y^0 = [G_+(d) + G_-(d)]/(\beta_1 Z_1) \quad [2.103]$$

(where, again, the slab must be two or three times thicker than the rf skin depth for the expressions to be valid).

In [2.100]-[2.103], Z_0 is the wave impedance of the propagating mode in the waveguide, Z_1 is the wave impedance of the non-propagating mode, β_0 is the cavity amplitude factor associate with the propagating mode, and β_1 is the amplitude factor associated with the non-propagating mode. (β_0 and β_1 were included to account for transmission into a resonant microwave cavity -- see section 2.5.2 for details). For a system designed to measure the transmission of 24 GHz microwave radiation³⁴, $Z_0 = 1.23$, $Z_1 = -5i$, $\beta_0 = 2.32 \times 10^{-2}$, and $\beta_1 = 1$.

3. CALCULATING THE CIRCULARLY POLARIZED KERNELS

3.1 Introduction

In section 2.4 of chapter 2 we found that the non-local constitutive relation between $\vec{j}(z)$ and $\vec{E}(z)$ in our slab could be written as

$$j_{\pm}(z) = \int_0^d K_{\pm}(z, \xi) E_{\pm}(\xi) d\xi \quad [2.44]$$

$$j_z(z) = 0 \quad [2.9]$$

where $K_{\pm}(z, \xi)$ are the circularly polarized current kernels. For a metal having a Fermi surface that's cylindrically symmetric about the z-axis, the kernels can be defined by

$$K_{\pm}(z, \xi) = K_{xx}(z, \xi) \pm iK_{yx}(z, \xi) \quad [2.45]$$

where $K_{xx}(z, \xi)$ and $K_{yx}(z, \xi)$ are the current densities generated in the x and y directions, respectively, at a point z due to a delta function electric field in the x direction at a point ξ . (see fig 4 on p. 31).

Using the current density expression [2.44], we were able to construct a general boundary value problem for the electric

fields $E_{\pm}(z)$ in the slab (see section 2.6 in chapter 2). However, we cannot solve the boundary value problem until we know the precise form of the kernels $K_{\pm}(z, \xi)$.

As mentioned in section 2.4, the kernels contain all the microscopic aspects of a given problem. In particular, they depend on the type of scattering the conduction electrons undergo at the surfaces of the slab. In this thesis, we wish to solve the boundary value problem for $E_{\pm}(z)$ in a metal with a spherical Fermi surface and for the two cases of specular and diffuse surface scattering. For diffuse surface scattering we can show that the kernels $K_{\pm}(z, \xi)$ are identical to the kernels $K_{\pm}^{\infty}(z, \xi)$ calculated for an infinite metal with a d.c. magnetic field directed along the z axis (see section 5.2 of chapter 5). For specular scattering we can show, using arguments similar to those of Platzmann and Buchsbaum²¹, that the current densities $j_{\pm}(z)$ can be correctly calculated using the expression

$$j_{\pm}(z) = \int_{-\infty}^{\infty} K_{\pm}^{\infty}(z, \xi) E_{\pm}(\xi) d\xi$$

provided $j_{\pm}(z)$ and $E_{\pm}(z)$ are made even functions of z and periodic with period $2d$. (see section 6.2 of chapter 6). This makes the specular scattering problem amenable to solution by fourier transform methods(see section 6.3).

Both of our problems can therefore be solved using the kernels for an infinite medium. In the present work we

calculate the kernels semi-classically using the method of Cohen, Harrison, and Harrison²⁶ to solve the Boltzmann transport equation. Our approach is different from those previously published^{10, 21, 22} in that the kernels $K_{\pm}^{\infty}(z, \xi)$ are calculated directly from the definition [2.45]; ie, we determine the current response in the x and y directions at a general point z in the slab due to a delta function electric field in the x direction at a point ξ .

Usually, the kernels associated with a given problem are calculated indirectly, using one of two techniques. The first, due originally to Reuter and Sondheimer¹⁰, assumes that the metal contains arbitrary electric fields $E_{\pm}(z)$ and determines the general current response $j_{\pm}(z)$ using, for example, Chamber's method¹⁸ to solve the Boltzmann transport equation. The resulting expression for $j_{\pm}(z)$ is then manipulated until it resembles [2.44] and the kernels are obtained by inspection. The second method^{21, 35} effectively calculates the space and time fourier transform of the kernels by determining the current response when the electric field in the metal varies as $\exp(ikz - i\omega t)$. The fourier transform of $K_{\pm}^{\infty}(z, \xi)$ is commonly labelled $\sigma_{\pm}(k, \omega)$ and is referred to as the frequency and wavenumber dependent conductivity tensor. The tensor plays a central role in the solution of problems involving specularly scattering surfaces^{10, 15, 21}

We present our simple, direct solution for the kernels in section 3.2. In section 3.3 we derive a sum rule that enables

us to check if the kernels have been calculated correctly. Finally, in section 3.4 we fourier transform the kernels and recover the frequency and wavenumber dependent conductivity tensor $\sigma_{\pm}(k, \omega)$ for a metal having a spherical Fermi surface^{21, 35}.

It should be noted that the direct solution can be readily adapted to handle any Fermi surface that has cylindrical symmetry about the z axis.

3.2 The Kernels in an Infinite Medium

Consider an infinite conducting medium having a d.c. magnetic field H directed along the z axis. According to the definition [2.45], the kernels $K_{\pm}^{\infty}(z, \xi)$ in this medium will be given by

$$K_{\pm}^{\infty}(z, \xi) = K_{xx}^{\infty}(z, \xi) \pm iK_{yx}^{\infty}(z, \xi) \quad [3.1]$$

where $K_{xx}^{\infty}(z, \xi)$ and $K_{yx}^{\infty}(z, \xi)$ are the current densities $j_x(z)$ and $j_y(z)$ due to the delta function electric field $\bar{E}(z) = \delta(z - \xi)\hat{x}$ (the time dependence is assumed to be $\exp(-i\omega t)$). Our problem, therefore, is to determine the current responses $j_x(z)$ and $j_y(z)$ due to the electric field $\bar{E}(z)$.

Two properties of the kernels substantially reduce the amount of work we must do. First, the current response at a point z only depends on the distance between z and ξ ; ie, the

kernels in this medium are translationally invariant:

$$K_{\pm}^{\infty}(z, \xi) = K_{\pm}^{\infty}(z - \xi) \quad [3.2]$$

We may therefore put the delta function electric field at $z = 0$ instead of $z = \xi$ with no loss of generality.

Second, when calculating the kernels we found that the only difference between the kernels calculated for $H = 0$ (ie, no magnetic field along the z axis) and the kernels calculated for $H \neq 0$ is that everywhere the frequency ω of the electric field appears in the $H = 0$ kernels, the factor $\omega \pm \omega_c$ appears in the $H \neq 0$ kernels. Here, ω_c is the cyclotron frequency defined by

$$\omega_c = \frac{eH}{m^*c} \quad [3.3]$$

where ω_c is in rad/sec, $e = |e|$ is the charge on the conduction electrons in esu, H is the d.c. field in Oersteds, m^* is the effective mass of the conduction electrons in gm, and c is the speed of light in cm/sec. We can therefore calculate the kernels for the simpler case of $H = 0$ and then generalize the result to $H \neq 0$.

With this in mind, we consider the problem shown in figure 7 where an infinite conducting medium contains only the delta function electric field

$$\vec{E}(z, t) = \delta(z)\hat{x}\exp(-i\omega t) \quad [3.4]$$

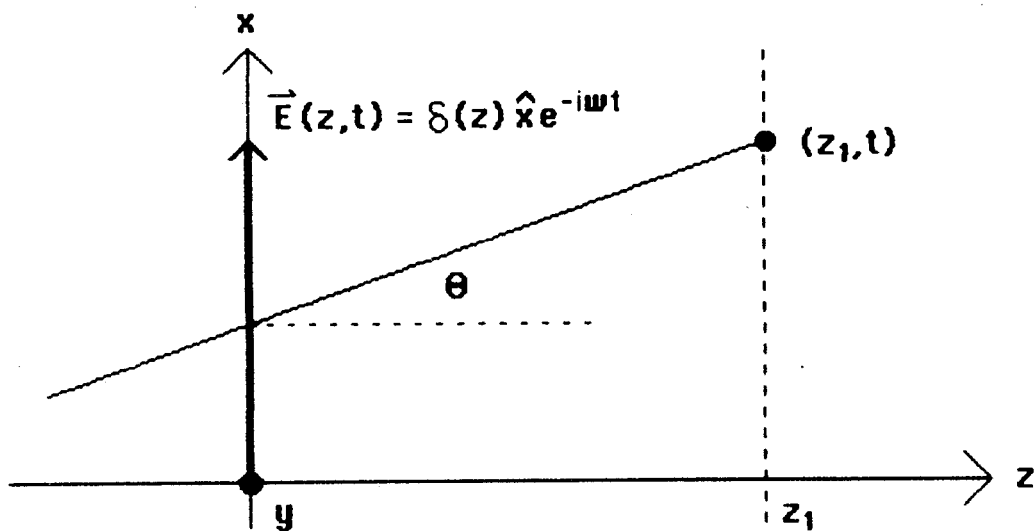


Fig. 7 The Infinite Medium Problem used to calculate the kernels $K_{\pm}^{\infty}(z, \xi)$. The metal has a delta function of electric field in the x direction at $z = 0$. We wish to calculate the current response at a general point z_1 .

Now, the current response at the point z , at time t is given by the semi-classical expression^{3,2}

$$\vec{j}(z,t) = -2e/(2\pi)^3 \int_{\vec{k}} \vec{v} g(z,\vec{k},t) d\vec{k} \quad [3.5]$$

where $g(z,\vec{k},t)$ is the deviation of the electron distribution function $f(\vec{r},\vec{k},t)$ from the equilibrium Fermi-Dirac distribution function f_0 for electrons of wave-vector \vec{k} , velocity \vec{v} , and position z at time t . The integral in $\vec{j}(z,t)$ is over all k -space.

The distribution function $g(z,\vec{k},t)$ is obtained from the Boltzmann transport equation, in the relaxation time approximation^{1,7}, using the method of Cohen, Harrison, and Harrison^{2,6} (see Appendix D):

$$g(z,\vec{k},t) = -(\partial f_0/\partial \epsilon) \int_{-\infty}^t e^{-(t-t')/\tau} d[\Delta\epsilon(t')] \quad [3.6]$$

$$d[\Delta\epsilon(t')] = -e\vec{v}(\vec{k}') \cdot \vec{E}(z',t') dt' \quad [3.7]$$

where τ is the relaxation time (the mean time a conduction electron can travel before suffering a collision) and $d[\Delta\epsilon(t')]$ is the energy picked up by an electron in the infinitesimal time interval $[t',t'+dt']$ as it travels along the unperturbed trajectory T_0 that passes through the phase space point (z,\vec{k}) at time t . The trajectory T_0 is the path that electrons would take to reach (z,\vec{k}) at time t if $\vec{E}(z,t) = 0$. In [3.7], (z',\vec{k}') is

the position of an electron on T_0 at a time $t' < t$.

To calculate $\bar{j}(z,t)$ at a point z_1 , we must first define the unperturbed trajectory T_0 . Note that we need only consider \bar{K} values on the Fermi surface because the term $(\partial f_0/\partial \epsilon)$ in $g(z,\bar{K},t)$ is very nearly $-\delta(\epsilon-\epsilon_F)$ where ϵ_F is the Fermi energy. This restricts the k -space integral in $\bar{j}(z,t)$ to an integral over the Fermi surface.

Now, our metal has a spherical Fermi surface. When $\bar{E}(z,t) = 0$, both the wave-vector \bar{K} and the velocity \bar{v} of an electron on the Fermi surface will be constant in time (ie, the electrons will travel along straight line trajectories in the slab). The \bar{K} and \bar{v} vectors are related by

$$m^*\bar{v} = \hbar\bar{K} \quad [3.8]$$

and their magnitudes are $|\bar{v}| = v_F$ and $|\bar{K}| = k_F$ where

$$k_F^3 = 3\pi^2 n \quad [3.9]$$

$$v_F = (\hbar/m^*)k_F \quad [3.10]$$

and n is the number density of the conduction electrons (typically, $n \approx 10^{22} \text{ cm}^{-3}$ so $k_F \approx 10^8 \text{ cm}^{-1}$ and $v_F \approx 10^7 \text{ cm/sec.}$). We shall write the \bar{K} vector of an electron passing through (z_1, t) as

$$k_x = k_F \sin\theta \cos\phi \quad [3.11]$$

$$k_y = k_F \sin\theta \sin\phi \quad [3.12]$$

$$k_z = k_F \cos\theta \quad [3.13]$$

where θ is the angle \vec{k} makes with the z axis and ϕ is the angle that the projection of \vec{k} onto the x-y plane makes with the x axis (see fig 7). The associated velocity vector \vec{v} is just

$$v_x = v_F \sin\theta \cos\phi \quad [3.14]$$

$$v_y = v_F \sin\theta \sin\phi \quad [3.15]$$

$$v_z = v_F \cos\theta \quad [3.16]$$

The expression for v_z gives us the particular straight line trajectory T_0 that passes through (z_1, t) :

$$z' = z_1 + v_F \cos\theta \cdot (t' - t) \quad [3.17]$$

where z' is the position of the electron along T_0 at any time t' .

Let us now apply the method of Cohen, Harrison, and Harrison to calculate the current response at z_1 . Note that in fig 7 we have explicitly chosen $z_1 > 0$. The derivation we are

about to give is valid for any value of z_1 (positive or negative) up until the final stages of calculation. Using the electric field expression [3.4] in [3.7] yields:

$$d[\Delta\epsilon(t')] = -ev_x(\bar{k}')\delta(z')e^{-i\omega t'} dt'$$

The k-vector is a constant along the trajectory so

$$v_x(\bar{k}') = v_x = v_F \sin\theta \cos\phi \text{ and}$$

$$d[\Delta\epsilon(t')] = -ev_F \sin\theta \cos\phi \delta(z') e^{-i\omega t'} dt' \quad [3.18]$$

The delta function $\delta(z')$ must now be written in terms of t' .

Using the definition of z' (equation [3.17]) and the delta function property

$$\delta(f(x)) = \sum_i \delta(x-x_i)/|f'(x_i)|; f(x_i) = 0 \quad [3.19]$$

we get

$$\delta(z') = \frac{\delta(t'-t_1)}{v_F |\cos\theta|} \quad [3.20]$$

where

$$t_1 = t - z_1/(v_F \cos\theta) \quad [3.21]$$

is the only root of z' . Inserting [3.20] in $d[\Delta\epsilon(t')]$ yields

$$d[\Delta\epsilon(t')] = -e \frac{\sin\theta}{|\cos\theta|} \cos\phi \delta(t'-t_1) e^{-i\omega t'} dt' \quad [3.22]$$

The distribution function $g(z, \mathbf{k}, t)$ is obtained by inserting [3.22] into [3.6] and carrying out the t' integration. The result is

$$g(z_1, \mathbf{k}, t) = g(z_1, \mathbf{k}) e^{-i\omega t} \quad [3.23]$$

where

$$g(z_1, \mathbf{k}) = e(\partial f_0 / \partial \epsilon) \frac{\sin\theta}{|\cos\theta|} \cos\phi e^{-[1-i\omega\tau]z_1 / (l \cos\theta)} \quad [3.24]$$

and we have defined the electron mean free path l by

$$l = v_F \cdot \tau \quad [3.25]$$

The current response in the x and y directions at z_1 are now given by [3.5],

$$j_x(z_1) = K_{xx}^{\infty}(z, \xi) = -2e / (2\pi)^3 \int_{\mathbf{k}} v_x(\mathbf{k}) g(z_1, \mathbf{k}) d\mathbf{k} \quad [3.26]$$

$$j_y(z_1) = K_{yx}^{\infty}(z, \xi) = -2e / (2\pi)^3 \int_{\mathbf{k}} v_y(\mathbf{k}) g(z_1, \mathbf{k}) d\mathbf{k} \quad [3.27]$$

Where we have suppressed the common $\exp(-i\omega t)$ time dependence of $\vec{j}(z_1, t)$ and $g(z_1, \mathbf{k}, t)$.

In our case, $j_x(z) = K_{xx}^\infty(z, \xi)$ and $j_y(z) = K_{yx}^\infty(z, \xi)$.

Since $K_\pm^\infty(z, \xi) = K_{xx}^\infty(z, \xi) \pm iK_{yx}^\infty(z, \xi)$ we can write down the circularly polarized kernels as

$$K_\pm^\infty(z_1) = -2e/(2\pi)^3 \int_{\vec{k}} v_\pm(\vec{k}) g(z_1, \vec{k}) d\vec{k} \quad [3.28]$$

where $v_\pm = v_x \pm iv_y$. Using the definitions of v_x and v_y given by [3.14] and [3.15],

$$v_\pm = v_F \sin\theta e^{\pm i\phi} \quad [3.29]$$

The circularly polarized kernels are therefore

$$K_\pm^\infty(z_1) = \frac{2e^2 v_F}{(2\pi)^3} \int_{\vec{k}} d\vec{k} \delta(\epsilon - \epsilon_F) \frac{\sin^3\theta}{|\cos\theta|} e^{\pm i\phi} \cos\phi e^{-[1-i\omega\tau] \frac{z_1}{l \cos\theta}} \quad [3.30]$$

where we have written $(\partial f_0 / \partial \epsilon)$ as $-\delta(\epsilon - \epsilon_F)$. We evaluate the integral in spherical polar coordinates ($d\vec{k} = k^2 \sin\theta dk d\theta d\phi$).

For a metal with a spherical Fermi surface,

$$(\epsilon - \epsilon_F) = (\hbar^2/2m^*)(k^2 - k_F^2)$$

so; by [3.19],

$$\delta(\epsilon - \epsilon_F) = (m^*/\hbar^2 k_F) \delta(k - k_F) = \delta(k - k_F) / (\hbar v_F)$$

and $K_{\pm}^{\infty}(z_1)$ becomes

$$K_{\pm}^{\infty}(z_1) = \frac{3}{4} \frac{\sigma_0}{l\pi} \left[\int_0^{2\pi} e^{\pm i\phi} \cos\phi d\phi \right] \left[\int_{\theta} d\theta \frac{\sin^3\theta}{|\cos\theta|} e^{-[1-i\omega\tau] \frac{z_1}{l \cos\theta}} \right] \quad [3.31]$$

where we have used the relations $v_F = (\hbar/m^*)k_F$, $k_F^3 = 3\pi^2 n$, $l = v_F \cdot \tau$, and the definition of the d.c. conductivity σ_0 ,

$$\sigma_0 = \frac{ne^2\tau}{m^*} \quad [3.32]$$

to re-write the leading coefficient in the form shown. The integral over ϕ in [3.31] is equal to π . One must be careful with the integral over θ because the limits depend on the value of z_1 . When $z_1 > 0$, only electrons with $v_z > 0$ will cross the delta function electric field and contribute to the current response at z_1 (see fig 7). Thus, when $z_1 > 0$, $0 \leq \theta \leq \pi/2$ and $|\cos\theta| = \cos\theta$. When $z_1 < 0$, $\pi/2 \leq \theta \leq \pi$ and $|\cos\theta| = -\cos\theta$.

Consider the case where $z_1 > 0$,

$$K_{\pm}^{\infty}(z_1) = \frac{3}{4} \frac{\sigma_0}{l} \int_0^{\pi/2} d\theta \frac{\sin^3\theta}{\cos\theta} e^{-[1-i\omega\tau] \frac{z_1}{l \cos\theta}} ; \quad z_1 > 0$$

Changing variable to $y = 1/\cos\theta$ ($\sin\theta d\theta = dy/y^2$) yields

$$K_{\pm}^{\infty}(z_1) = \frac{3}{4} \frac{\sigma_0}{l} \int_1^{\infty} \left(\frac{1}{y} - \frac{1}{y^3} \right) dy e^{-[1-i\omega\tau] \frac{z_1}{l} y} ; \quad z_1 > 0 \quad [3.33]$$

On the other hand, when $z_1 < 0$,

$$K_{\pm}^{\infty}(z_1) = \frac{3}{4} \frac{\sigma_0}{l} \int_{\pi/2}^{\pi} d\theta \frac{\sin^3\theta}{-\cos\theta} e^{-[1-i\omega\tau] \frac{z_1}{l \cos\theta}} ; \quad z_1 < 0$$

and changing variable to $y = -1/\cos\theta$ ($\sin\theta d\theta = -dy/y^2$) yields

$$K_{\pm}^{\infty}(z_1) = \frac{3}{4} \frac{\sigma_0}{\ell} \int_1^{\infty} \left(\frac{1}{y} - \frac{1}{y^3}\right) dy e^{-[1-i\omega\tau] \frac{|z_1|}{\ell} y} ; z_1 < 0 \quad [3.34]$$

Hence, for all z , we can define the circularly polarized kernels as

$$K_{\pm}^{\infty}(|z|) = \frac{3}{4} \frac{\sigma_0}{\ell} \int_1^{\infty} \left(\frac{1}{y} - \frac{1}{y^3}\right) dy e^{-[1-i\omega\tau] \frac{|z|}{\ell} y}$$

The kernels are even functions of z . This is to be expected because of the symmetry of the spherical Fermi surface (the distribution of electrons with $v_z > 0$ that generate currents in the space $z > 0$ looks the same at the distribution of electrons with $v_z < 0$ that contribute to the currents in the space $z < 0$).

Now, by translational invariance, if the delta function electric field is at $z = \xi$, the kernels are given by

$$K_{\pm}^{\infty}(|z-\xi|) = \frac{3}{4} \frac{\sigma_0}{\ell} \int_1^{\infty} \left(\frac{1}{y} - \frac{1}{y^3}\right) dy e^{-[1-i\omega\tau] \frac{|z-\xi|}{\ell} y}$$

and we may account for a d.c. magnetic field H along the z axis simply by replacing ω by $\omega \pm \omega_c$.

Hence, the circularly polarized kernels $K_{\pm}^{\infty}(z, \xi)$ are

$$K_{\pm}^{\infty}(z, \xi) = \frac{3}{4} \frac{\sigma_0}{\ell} \int_1^{\infty} \left(\frac{1}{y} - \frac{1}{y^3} \right) dy e^{-[1-i(\omega \pm \omega_c)\tau] \frac{|z-\xi|}{\ell} y} \quad [3.35]$$

3.2.1 A Closed Form for the Kernels

We can write $K_{\pm}^{\infty}(z, \xi)$ in closed form with very little effort. Define a variable x as

$$x = [1-i(\omega \pm \omega_c)\tau] |z-\xi| / \ell \quad [3.36]$$

(where the \pm subscript on x is suppressed). We write the kernels in terms of this new variable:

$$K_{\pm}^{\infty}(x) = \frac{3}{4} \frac{\sigma_0}{\ell} \int_1^{\infty} \left(\frac{1}{y} - \frac{1}{y^3} \right) dy e^{-xy}$$

Integrating the second term twice by parts yields

$$K_{\pm}^{\infty}(x) = \frac{3}{4} \frac{\sigma_0}{\ell} \left[\left(1 - \frac{1}{2} x^2\right) E_1(x) + \frac{1}{2} (x-1) e^{-x} \right] \quad [3.37]$$

where $E_1(x)$ is the exponential integral for a complex argument:

$$E_1(x) = \int_1^{\infty} \frac{e^{-xy}}{y} dy \quad [3.38]$$

The exponential integral is discussed in appendix E. The integral exists and is analytic for all x except when $\text{Re}[x] < 0$ ($E_1(x)$ goes to infinity at $x = 0$). From the form of x we see

that $\text{Re}[\chi] = |z-\xi|/l$ which is never negative and zero only when $z = \xi$. The kernels $K_{\pm}^{\infty}(z, \xi)$ are therefore well defined for all (z, ξ) and infinite at $z = \xi$.

3.3 A Sum Rule to Check the Kernels

There is a simple way to check if we have obtained the correct form of the kernels $K_{\pm}^{\infty}(z, \xi)$. If we assume that our infinite medium contains arbitrary electric fields $E_{\pm}(z)$ then the current response throughout the metal would be given by

$$j_{\pm}(z) = \int_{-\infty}^{\infty} K_{\pm}^{\infty}(|z - \xi|) E_{\pm}(\xi) d\xi \quad [3.39]$$

However, if the amplitude of $E_{\pm}(z)$ were a constant throughout all space (ie, $E_{\pm}(z) = E_{\pm}^0$) then $j_{\pm}(z)$ would be locally related to $E_{\pm}(z)$ by the a.c. conductivity $\sigma(\omega \pm \omega_c)$ defined by

$$\sigma(\omega \pm \omega_c) = \sigma_0 / [1 - i(\omega \pm \omega_c)\tau] \quad [3.40]$$

and we could write

$$j_{\pm}(z) = \sigma(\omega \pm \omega_c) E_{\pm}^0 \quad [3.41]$$

Results [3.40] and [3.41] are derived, for example, in chapter 1 of the solid state text of Ashcoft and Mermin³². We can also derive it using the methods presented in section 3.2 (we need

only replace the delta function electric field used in section 3.2 with the spatially constant electric field

$$\vec{E}(z, t) = E_0 \hat{x} \exp(-i\omega t).$$

But the current response generated by E_{\pm}^0 should also be given by

$$j_{\pm}(z) = \left[\int_{-\infty}^{\infty} K_{\pm}^{\infty}(|z - \xi|) d\xi \right] E_{\pm}^0 \quad [3.42]$$

Equating [3.41] and [3.42] gives the sum rule:

$$\sigma(\omega \pm \omega_c) = \int_{-\infty}^{\infty} K_{\pm}^{\infty}(|z - \xi|) d\xi \quad [3.43]$$

Let us evaluate the integral in [3.43]. The easiest way to do this is to use the integral form [3.35] of the kernels $K_{\pm}^{\infty}(z, \xi)$, change variable from ξ to $s = \xi - z$, and do the integral over s before the integral over y :

$$\begin{aligned} \int_{-\infty}^{\infty} K_{\pm}^{\infty}(|z-s|) d\xi &= \frac{3}{4} \frac{\sigma_0}{\ell} \int_{-\infty}^{\infty} d\xi \int_1^{\infty} dy \left(\frac{1}{y} - \frac{1}{y^3} \right) e^{-LAX \frac{|z-s|}{\ell} y} \\ &= \frac{3}{4} \frac{\sigma_0}{\ell} \int_1^{\infty} dy \left(\frac{1}{y} - \frac{1}{y^3} \right) 2 \int_0^{\infty} ds e^{-LAX \frac{s}{\ell} y} \\ &= \frac{3}{2} \sigma(\omega \pm \omega_c) \int_1^{\infty} \left(\frac{1}{y^2} - \frac{1}{y^4} \right) dy \\ &= \sigma(\omega \pm \omega_c) \end{aligned}$$

where we have written $[1 - i(\omega \pm \omega_c)\tau] = LAX$

and our kernels do indeed satisfy the sum rule.

3.4 The Conductivity Tensor

When we are solving for the rf electric fields in our slab under specular surface scattering conditions we will need to calculate the frequency and wavenumber dependent conductivity tensor $\sigma_{\pm}(k, \omega)$ which can be defined as the fourier transform of $K_{\pm}^{\infty}(|z|)$; ie,

$$\sigma_{\pm}(k, \omega) = \int_{-\infty}^{\infty} K_{\pm}^{\infty}(|z|) \exp(ikz) dz \quad [3.44]$$

The form of $\sigma_{\pm}(k, \omega)$ is well known³⁵ and can be obtained, for example, by calculating the current response in an infinite metal due to an electric field that varies in time and space as $\exp(ikz - i\omega t)$. We re-derive $\sigma_{\pm}(k, \omega)$ here for completeness.

Taking into account the absolute value sign in the kernel argument we write:

$$\begin{aligned} \sigma_{\pm}(k, \omega) &= \int_{-\infty}^0 K_{\pm}^{\infty}(-z) e^{ikz} dz + \int_0^{\infty} K_{\pm}^{\infty}(z) e^{ikz} dz \\ &= \int_0^{\infty} K_{\pm}^{\infty}(z) e^{-ikz} dz + \int_0^{\infty} K_{\pm}^{\infty}(z) e^{ikz} dz \end{aligned} \quad [3.46]$$

If we use the integral form [3.35] of the kernels in [3.46] and carry out the integration over z first. The result is

$$\sigma_{\pm}(k, \omega) = \frac{3}{4} \sigma(\omega \pm \omega_c) \int_1^{\infty} \left(\frac{1}{y} - \frac{1}{y^3} \right) dy \left[\frac{1}{y - v_{\pm}} + \frac{1}{y + v_{\pm}} \right] \quad [3.47]$$

where $v_{\pm} = ikl/[1 - i(\omega \pm \omega_c)\tau]$. If we now let $x = 1/y$ then [3.47] becomes

$$\sigma_{\pm}(k, \omega) = \frac{3}{4} \sigma(\omega \pm \omega_c) \int_0^1 (1 - x^2) dx \left[\frac{1}{1 - v_{\pm}x} + \frac{1}{1 + v_{\pm}x} \right] \quad [3.48]$$

The integrands in [3.48] may be simplified using long division. The resulting integrands can be easily integrated out to get:

$$\sigma_{\pm}(k, \omega) = \frac{3}{4} \sigma(\omega \pm \omega_c) k(v_{\pm}) \quad [3.49]$$

where

$$k(y) = \frac{1}{y^3} \left[2y - (1 - y^2) \ln \left(\frac{1+y}{1-y} \right) \right] \quad [3.50]$$

and this is precisely the same form of $\sigma_{\pm}(k, \omega)$ obtained by other authors.

3.4.1 Limiting Forms of $k(y)$

The function $k(y)$ takes on particularly simple forms in the

two limits $y \ll 1$ and $y \gg 1$.

Limit: $y \rightarrow 0$

The logarithm in $k(y)$ can be expanded in the Taylor series:

$$\begin{aligned} \frac{1}{2} \ln \left[\frac{1+y}{1-y} \right] &= \sum_{n=1}^{\infty} \frac{y^{(2n-1)}}{(2n-1)} \\ &= y + \frac{1}{3} y^3 + \frac{1}{5} y^5 + \frac{1}{7} y^7 + \dots \end{aligned}$$

hence, as $y \rightarrow 0$, we can write

$$(1-y^2) \ln \left[\frac{1+y}{1-y} \right] \approx 2y - \frac{4}{3} y^3 - \frac{4}{15} y^5$$

Substituting this into [3.50] yields

$$k(y) = \frac{4}{3} + \frac{4}{15} y^2 ; y \ll 1 \quad [3.51]$$

Limit: $y \gg 1$

When $y \gg 1$ we can write

$$\begin{aligned}\ln\left[\frac{1+y}{1-y}\right] &= \ln\left[-1 \cdot \frac{1+\frac{1}{y}}{1-\frac{1}{y}}\right] \\ &= \ln(-1) + \ln\left(1+\frac{1}{y}\right) - \ln\left(1-\frac{1}{y}\right) \\ &\simeq i\pi + \frac{2}{y}\end{aligned}$$

Substituting this into [3.50] and keeping terms to first order in $1/y$ yields:

$$k(y) = i\pi/y \qquad [3.52]$$

4. SOLUTION IN THE NORMAL SKIN EFFECT REGIME

4.1 Introduction

In this chapter we solve for the electric fields in the slab in the normal skin effect (NSE) regime where $\delta/l \gg 1$ and the current densities $j_{\pm}(z)$ are locally related to the electric fields $E_{\pm}(z)$ by Ohm's Law:

$$j_{\pm}(z) = \sigma_0 E_{\pm}(z) \quad [4.1]$$

While this problem has been considered in detail by several authors^{1,7,28,30,38,39} there are two useful reasons for solving it again in our notation. First, the NSE solutions provide a valuable check on the electric fields found by solving the boundary value problem of chapter 2 for specular and diffuse surface scattering. (the latter solutions, which are valid for any δ/l ratio, must reduce to the simpler NSE results when we set $\delta/l \gg 1$). Second, it's a good idea to review the behaviour of the transmission coefficients T_{\pm} and surface impedances z_{\pm}^S in the NSE regime for the benefit of readers unfamiliar with the usual microwave transmission theory.

The electric field solution is covered in section 4.2 while the NSE transmission theory is reviewed in section 4.3.

4.2 The NSE Solutions

In chapter 2 we found that the electric fields in our slab could be described by the boundary value problem:

$$E_{\pm}''(z) + [2i\mu_{\pm}/(\sigma_0\delta_0^2)]j_{\pm}(z) = 0 \quad [2.46]$$

$$j_{\pm}(z) = \int_0^d K_{\pm}(z, \xi) E_{\pm}(\xi) d\xi \quad [2.44]$$

$$h_{\pm}(0) = 1; h_{\pm}(d) = 0 \quad [2.48]$$

where differentiation with respect to z is denoted by a prime (') and the magnetic fields $h_{\pm}(z)$ are related to the electric fields $E_{\pm}(z)$ by

$$E_{\pm}'(z) = \pm(\omega\mu_{\pm}/c)h_{\pm}(z) \quad [4.2]$$

Replacing the non-local current density [2.44] with Ohms's Law [4.1] yields a second order differential equation for $E_{\pm}(z)$:

$$E''(z) + (2i\mu/\delta_0^2)E(z) = 0 \quad [4.3]$$

(for simplicity, the \pm subscripts have been suppressed on $E_{\pm}(z)$ and μ_{\pm}).

The solutions of [4.3] are

$$E(z) = Ae^{ikz} + Be^{-ikz} \quad [4.4]$$

where A and B are constants and

$$k^2 = 2i\mu/\delta_0^2 \quad [4.5]$$

The corresponding magnetic fields in the slab are given by [4.2],

$$h(z) = \pm(ick/\omega\mu)[Ae^{ikz} - Be^{-ikz}] \quad [4.6]$$

(again, \pm subscripts are omitted for simplicity).

The boundary conditions $h_{\pm}(0) = 1$; $h_{\pm}(d) = 0$, and equation [4.6], determine A and B; that is

$$h(0) = 1 = \pm(ick/\omega\mu)[A - B]$$

$$h(d) = 0 = \pm(ick/\omega\mu)[Ae^{ikd} - Be^{-ikd}]$$

gives us

$$A = \pm(\omega\mu/ick)e^{-ikd}/(e^{-ikd} - e^{ikd}) \quad [4.7]$$

$$B = Ae^{2ikd} \quad [4.8]$$

Following the notation of chapter 2, we shall refer to the electric field solutions that satisfy the boundary conditions [2.48] as $G_{\pm}(z)$. Substituting [4.7] and [4.8] into [4.4] shows

$$G_{\pm}(z) = \mp(\omega\mu/ick) \frac{\cosh(ik[d-z])}{\sinh(ikd)} \quad [4.9]$$

or, since

$$ik = \sqrt{-2i\mu_{\pm}}/\delta_0 \quad [4.10]$$

we can write $G_{\pm}(z)$ as

$$G_{\pm}(z) = \mp \frac{i}{2} \frac{\omega}{c} \delta_0 \sqrt{-2i\mu_{\pm}} \frac{\cosh(\sqrt{-2i\mu_{\pm}} [d-z]/\delta_0)}{\sinh(\sqrt{-2i\mu_{\pm}} d/\delta_0)} \quad [4.11]$$

(all \pm subscripts restored).

The circularly polarized transmission coefficients T_{\pm} and surface impedances z_{\pm}^S are now calculated using equations [2.75] and [2.79] (see section 2.5.1):

$$z_{\pm}^S = \mp \frac{i}{2} \frac{\omega}{c} \delta_0 \sqrt{-2i\mu_{\pm}} \coth(\sqrt{-2i\mu_{\pm}} d/\delta_0) \quad [4.12]$$

$$T_{\pm} = \frac{\omega}{c} \delta_0 \sqrt{-2i\mu_{\pm}} / \sinh(\sqrt{-2i\mu_{\pm}} d/\delta_0) \quad [4.13]$$

4.3 Predictions of the NSE Transmission Theory

Microwave transmission experiments are usually carried out in the thick slab limit where $d/\delta \gg 1$ (in Nickel, at 24 GHz, $\delta_0 \leq 0.8 \mu\text{m}$ while d is the order of $5 \mu\text{m}$ or more -- thinner slabs are very difficult to fabricate). When $d/\delta \gg 1$, the NSE expressions for T_{\pm} and z_{\pm}^S become

$$z_{\pm}^S \approx \mp \frac{i}{2} \frac{\omega}{c} \delta_0 \sqrt{-2i\mu_{\pm}} \quad [4.14]$$

$$T_{\pm} \approx 2 \frac{\omega}{c} \delta_0 \sqrt{-2i\mu_{\pm}} \exp(-\sqrt{-2i\mu_{\pm}} d/\delta_0) \quad [4.15]$$

(for large x , $\sinh(x) \approx \exp(x)/2$ and $\coth(x) \approx 1$)

Only the permeabilities μ_{\pm} vary with the d.c. magnetic field H_0 ; μ_{+} exhibits a monotonic variation with H_0 (see figure 8) while μ_{-} goes through a minimum when H_0 corresponds to FMAR and a maximum when H_0 corresponds to FMR[†] (see figure 9).

4.3.1 Variation of NSE Surface Impedance with Magnetic Field

The surface impedances z_{\pm}^S vary as the square root of the permeabilities μ_{\pm} . Since μ_{+} varies monotonically with H_0 , so will z_{+}^S (see figure 10). In contrast, z_{-}^S (which depends on the magnetically active permeability)

[†]In Nickel, at 24 GHz, $\mu_{-}(\text{FMAR}) \approx 0.03i$ while $\mu_{-}(\text{FMR}) \approx 32i$.

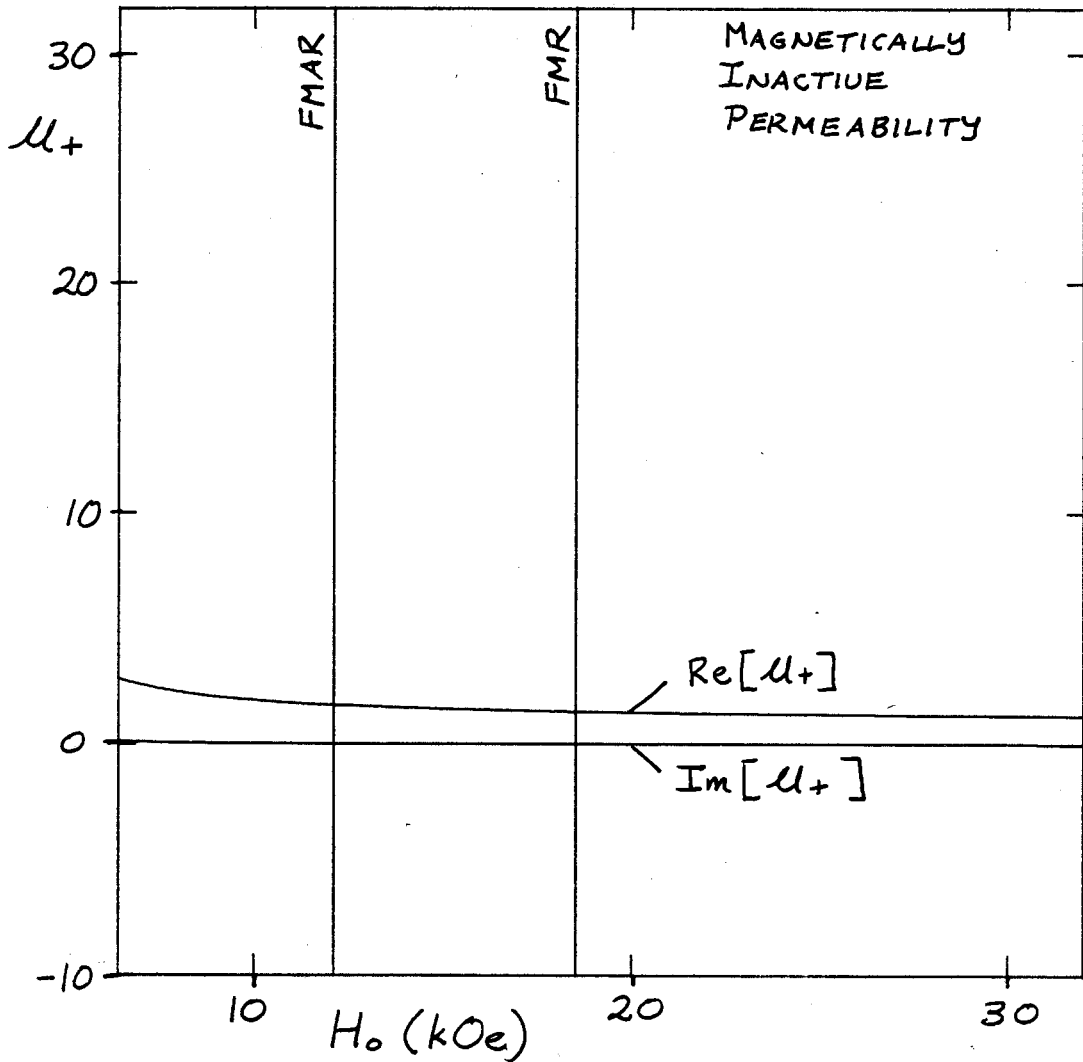


Fig. 8 Variation of the positive circularly polarized permeability μ_+ with H_0 in Nickel at 24 GHz. The plot was made using equation [2.31] from section 2.3 and the Nickel parameters of Appendix A. Note that μ_+ exhibits only a slow, monotonic variation with H_0 .

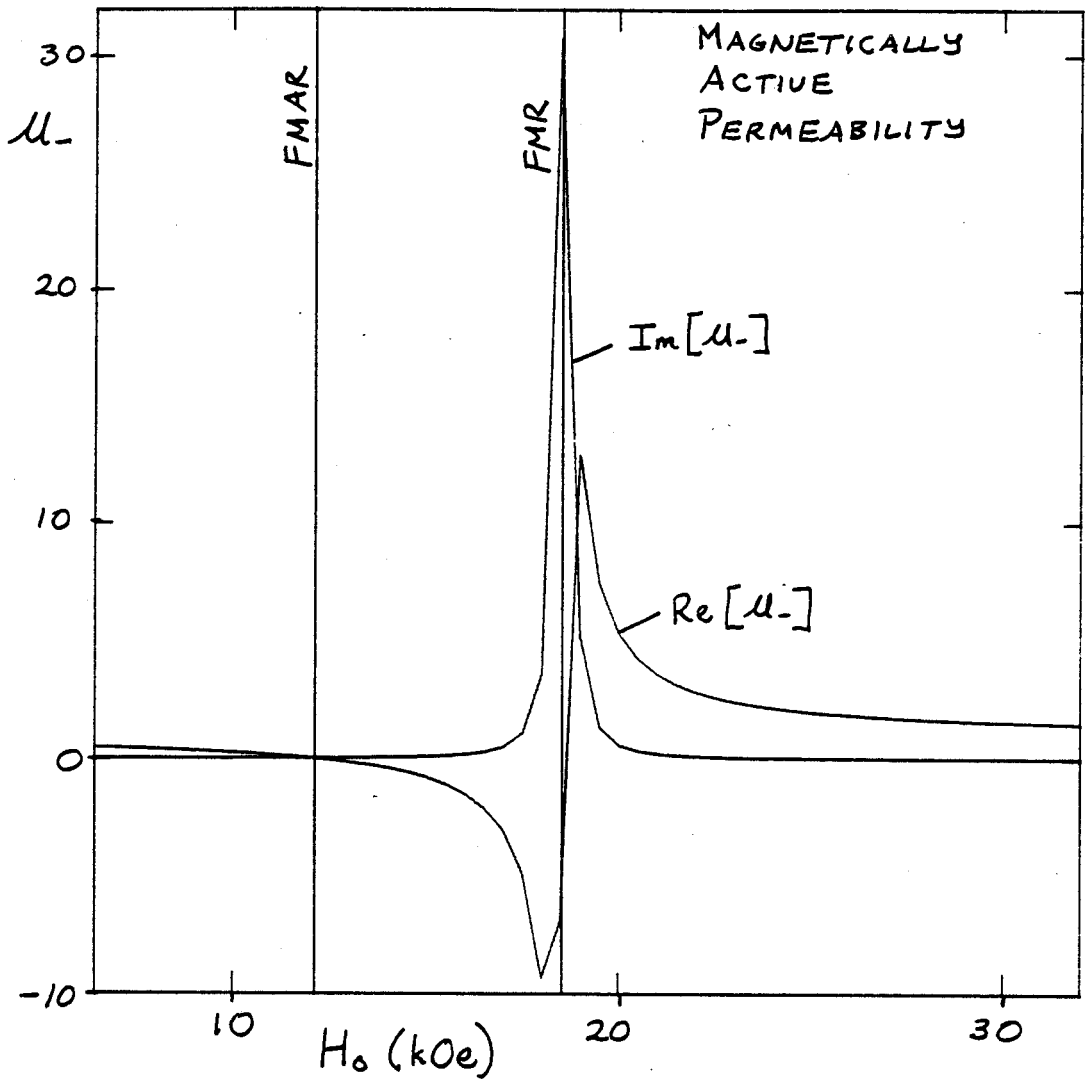


Fig. 9 Variation of the negative circularly polarized permeability μ_- with H_0 in Nickel at 24 GHz. The plot was made using equation [2.31] from section 2.3 and the Nickel parameters of Appendix A. Note that μ_- goes through a minimum when H_0 corresponds to FMAR and a maximum when H_0 corresponds to FMR.

μ_-) goes through a minimum at FMAR and a maximum at FMR (see figure 11).

4.3.2 Variation of NSE Transmission Coefficient with Magnetic Field

The permeabilities μ_{\pm} directly control the penetration of microwave radiation into the slab. If we let d/δ_0 become very large then the electric fields $G_{\pm}(z)$ near the $z = 0$ face of the slab can be written as

$$G_{\pm}(z) \approx \mp \frac{i}{2} \frac{\omega}{c} \delta_0 \sqrt{-2i\mu_{\pm}} \exp(-\sqrt{-2i\mu_{\pm}} z/\delta_0) \quad [4.16]$$

Hence, in a very thick slab the electric fields $G_{\pm}(z)$ decay exponentially near the front surface with a characteristic decay length

$$\delta_{\pm} = \delta_0 / \sqrt{-2i\mu_{\pm}} \quad [4.17]$$

which we identify as the effective NSE skin depth δ in a ferromagnetic metal.

Since μ_+ decreases slowly and monotonically, with H_0 then δ_+ will slowly increase with H_0 ; the penetration of positive circularly polarized radiation into the slab will tend to increase with H_0 . However μ_- has a strong H_0 dependence. Near FMAR (where μ_- is small and imaginary) δ_- goes through a

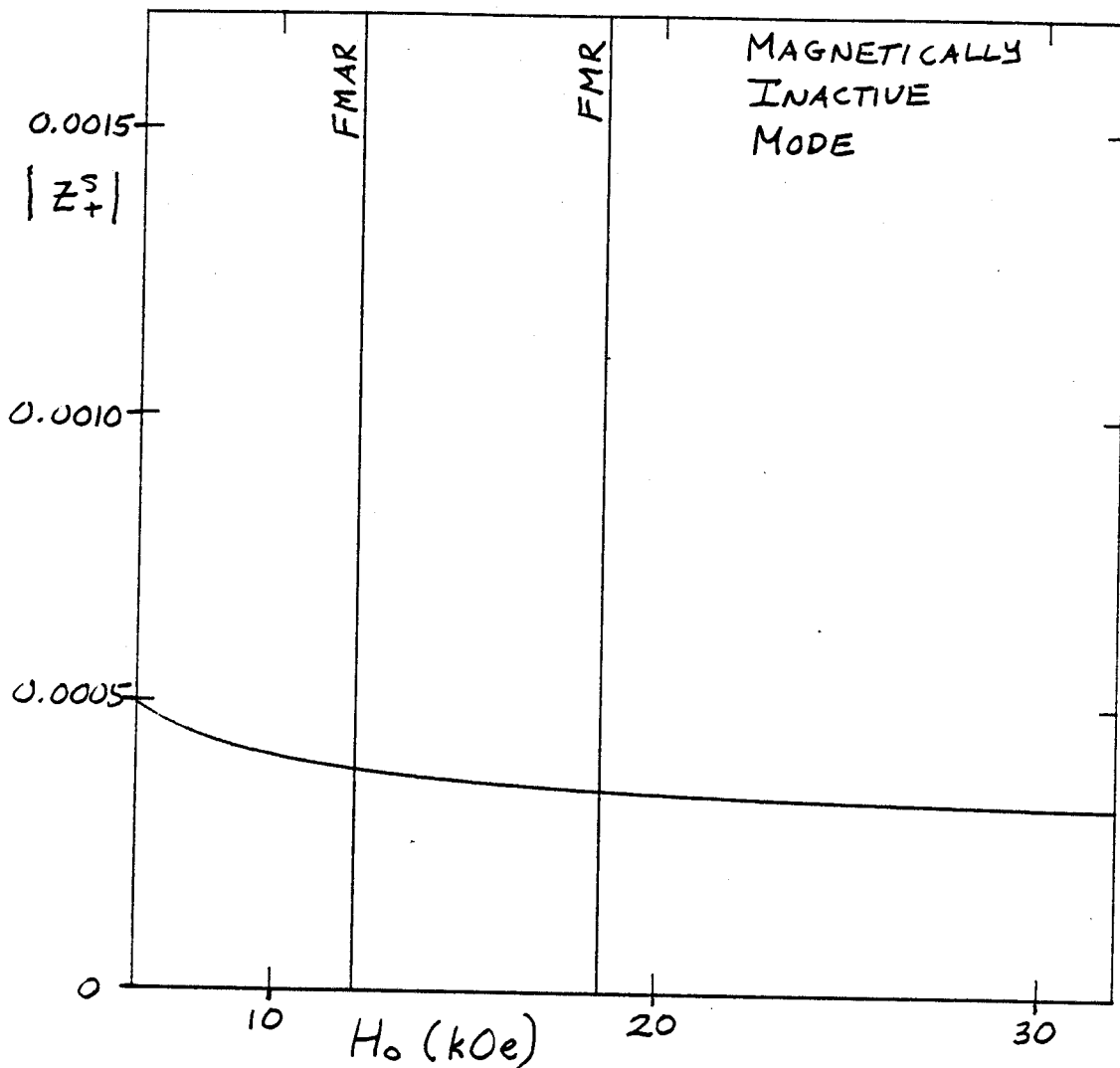


Fig. 10 Variation of the positive circularly polarized surface impedance $|z_+^S|$ with H_0 . The plot was made using the thick slab expression [4.14] and the parameters of Appendix A. The amplitude of z_+^S exhibits only a slow, monotonic variation with H_0 .

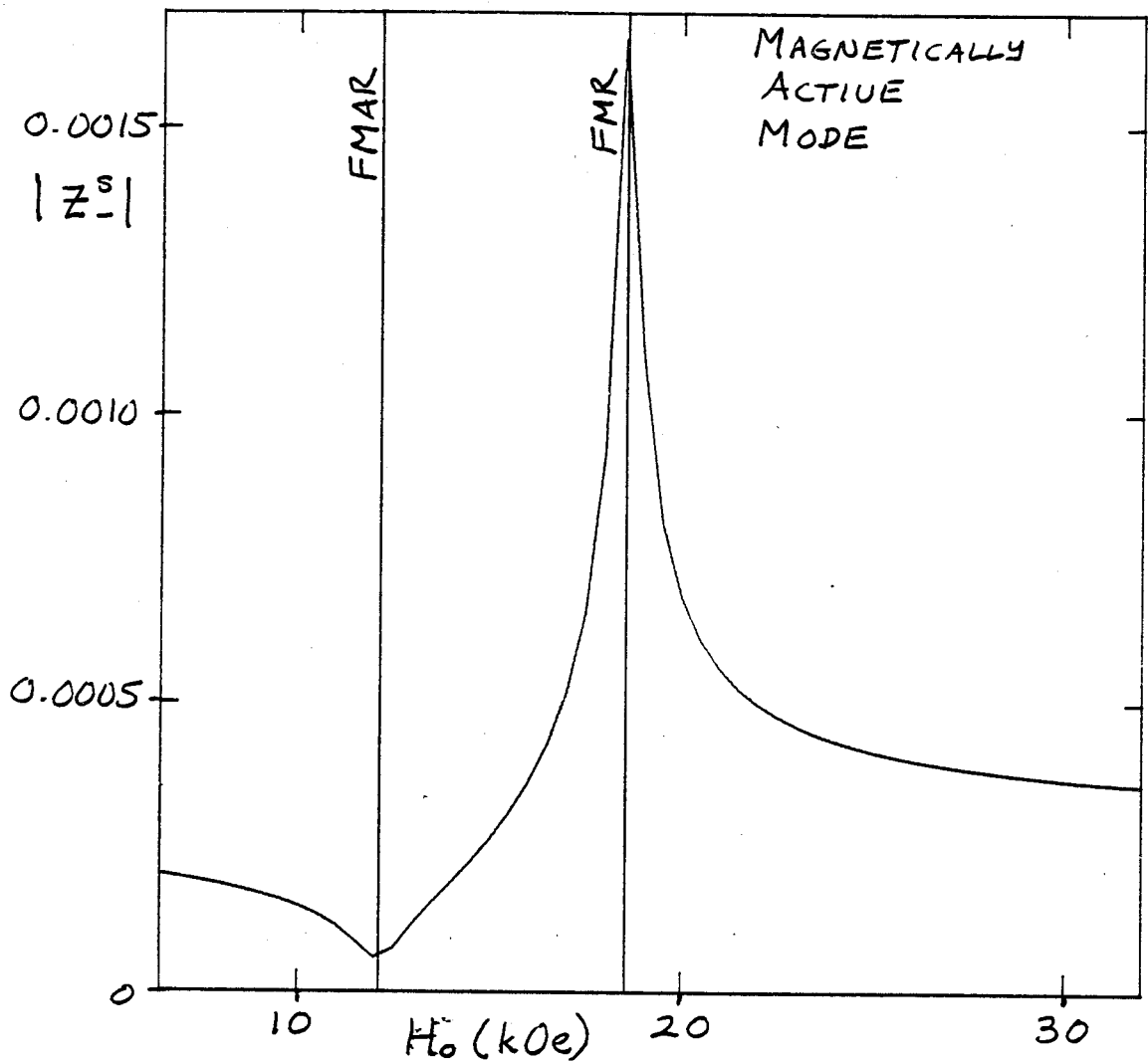


Fig. 11 Variation of the negative circularly polarized surface impedance $|z_-^S|$ with H_0 . The plot was made using the thick slab expression [4.14] and the parameters of Appendix A. The amplitude of z_-^S goes through a minimum at FMAR and a maximum at FMR.

maximum, becoming several times larger than δ_0 . Hence, negative circularly polarized radiation penetrates much deeper into a ferromagnetic metal at FMAR than into a non-magnetic metal. On the other hand, at FMR (where μ_- is large and imaginary) δ_- goes through a minimum, becoming several times smaller than δ_0 . At FMR, negative circularly polarized radiation is virtually excluded from a ferromagnetic metal. In Nickel, at 24 GHz, $\delta_0 \approx 0.8 \mu\text{m}$ while $\delta_-(\text{FMAR})/\delta_0 \approx 4$ and $\delta_-(\text{FMR})/\delta_0 \approx 0.125$

The depth to which incident radiation can penetrate into a metal slab before suffering appreciable attenuation has a direct bearing on the transmitted signal. In figure 12, we plot $|T_+|$ against H_0 for a $5 \mu\text{m}$ thick slab of Nickel using [4.15] and the parameters of Appendix A. As the effective rf skin depth δ_+ increases monotonically with H_0 , so does the transmission. In figure 13, we plot $|T_-|$ against H_0 for a $5 \mu\text{m}$ thick slab. The curve goes through a strong maximum at FMAR (where the skin depth δ_- is a maximum) and a deep minimum at FMR (where the skin depth is a minimum).

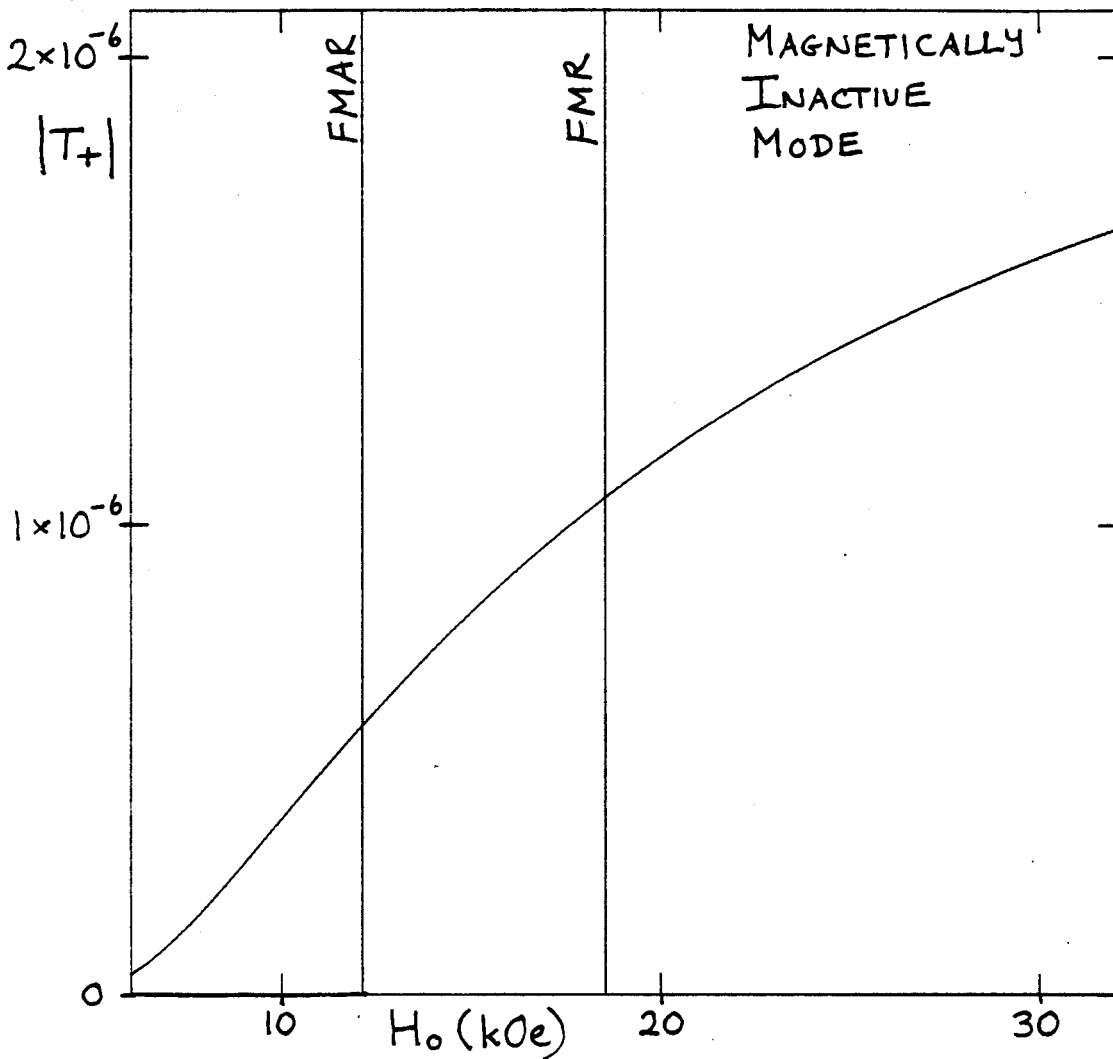


Fig. 12 Variation of the positive circularly polarized transmission coefficient $|T_+|$ with H_0 . The plot was made using the thick slab expression [4.15] and the parameters of Appendix A. The slab was assumed to be $5 \mu\text{m}$ thick. The amplitude of T_+ exhibits only a slow, monotonic variation with H_0 .

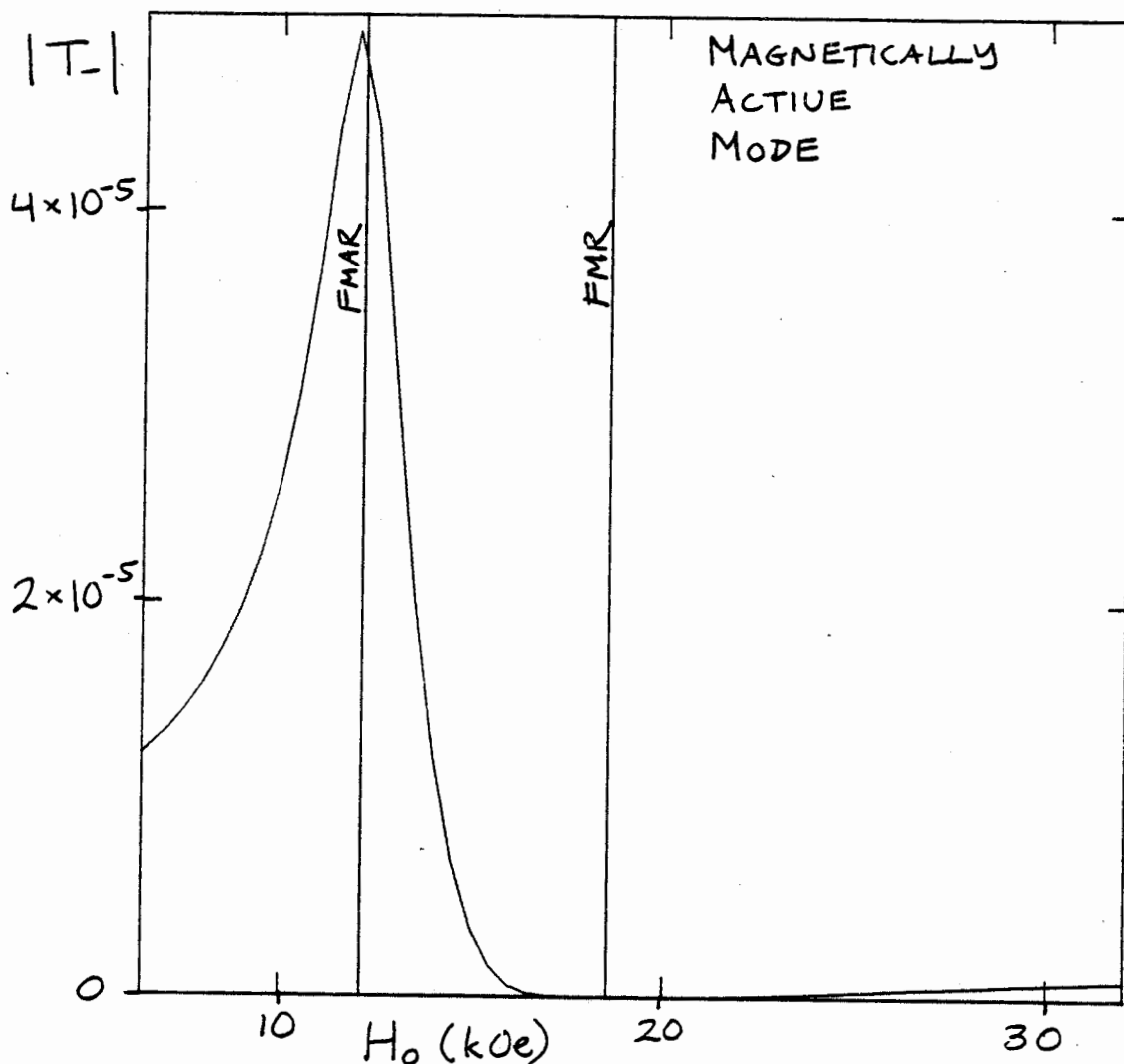


Fig. 13 Variation of the negative circularly polarized transmission coefficient $|T_-|$ with H_0 . The plot was made using the thick slab expression [4.15] and the parameters of Appendix A. The slab was assumed to be $5 \mu\text{m}$ thick. The amplitude of T_- goes through a strong maximum at FMAR and a deep minimum at FMR.

5. ELECTRIC FIELD SOLUTION FOR DIFFUSE SURFACE SCATTERING

5.1 Introduction

The general solution of the boundary value problem satisfied by the rf electric fields $E_{\pm}(z)$ in our slab has already been worked out in detail by Baraff^{22, 23} and others^{40, 41} for the case of diffuse surface scattering of the conduction electrons. However, the methods of solution are extremely complex and generally involve some sort of iterative process that converges like $\exp(-d/l)$. While the solutions have proven useful for determining various properties of the electric fields in the $d/l \gg 1$ limit, they are unsuitable for calculating the electric field distribution across the slab for arbitrary δ/l and slab thickness d^{\dagger} .

In view of this, we present an alternate method of solution. We solve the boundary value problem numerically, calculating the electric fields $E_{\pm}(z)$ approximately over a uniform grid of $N+1$ equally spaced points across the slab. In contrast to the analytic solutions, the numerical solution is easy to implement, valid for any δ/l ratio and slab thickness d ,

[†] Perhaps the best way to appreciate the difficulties involved in trying to implement one of the analytic solutions is to work through one of the papers of Baraff^{22, 23}

and readily extendable to include, for example, the effects of exchange or a different Fermi surface.

Our numerical solution is carried out in several steps. We begin in section 5.2 by writing out the boundary value problem for $E_{\pm}(z)$ that was derived in chapter 2. We then show that the kernels $K_{\pm}(z, \xi)$ appropriate for a slab with diffusely scattering faces are identical to the infinite medium kernels $K_{\pm}^{\infty}(|z-\xi|)$ discussed in chapter 3.

In section 5.3 we reduce the second order, integro-differential equations for $E_{\pm}(z)$ into a set of simultaneous equations for the $N+1$ electric field points across the slab. The boundary conditions are incorporated into the equations in section 5.4. We show how a change in the boundary conditions from $h_{\pm}(0) = 1, h_{\pm}(d) = 0$ to $E_{\pm}(0) = 1, h_{\pm}(d) = 0$ reduces the number of equations we must solve.

The coefficients of the simultaneous equations consist mainly of terms involving the integral of $K_{\pm}^{\infty}(|z-\xi|)$ over z and ξ . Symmetry relations amongst the integral terms are considered in section 5.5 while the various integrals are worked out in section 5.6. In section 5.7 we check to make sure we can recover the NSE solutions of chapter 4 from our numerical solution when the mean free path l and relaxation time τ go to zero. In section 5.8 we consider how to calculate the magnetic fields $h_{\pm}(z)$ and current densities $j_{\pm}(z)$ in the slab. Finally, in section 5.9, we consider the implementation of the numerical solution on a computer and discuss the convergence properties of

the solution.

5.1.1 Summation Convention

When we are developing the numerical solution to the boundary value problem we will frequently be writing equations that contain sums of the form

$$I_{i0}E_0 + I_{i1}E_1 + I_{i2}E_2 + I_{i3}E_3 + \dots + I_{iN}E_N$$

which we can write in the short notation

$$\sum_{j=0}^N I_{ij}E_j$$

An even shorter notation is to simply write the sum as

$$I_{ij}E_j$$

where we have adopted the convention that whenever an index is repeated in a given product we are to sum over the index. For example, the product $I_{ij}E_j$ is summed over j from 0 to N . This is called the Einstein summation convention. Whenever we write an expression using the summation convention we shall explicitly state the limits on the sum.

5.2 The Boundary Value Problem for Diffuse Scattering

We wish to solve the following boundary value problem for the rf electric fields $E_{\pm}(z)$ in our slab:

$$E_{\pm}''(z) + [2i\mu_{\pm}/(\sigma_0\delta_0^2)]j_{\pm}(z) = 0 \quad [2.46]$$

$$j_{\pm}(z) = \int_0^d K_{\pm}(z, \xi)E_{\pm}(\xi)d\xi \quad [2.44]$$

where the prime denotes differentiation with respect to z and $K_{\pm}(z, \xi)$ are the current kernels discussed in section 2.3 of chapter 2.

Before we can begin the solution, we need to know the form of the kernels. When the faces of the slab scatter electrons diffusely, the kernels $K_{\pm}(z, \xi)$ in [2.44] are just $K_{\pm}^{\infty}(|z-\xi|)$, the kernels we calculated in chapter 3 for an infinite medium. To see this, we refer to figure 14 where an infinite conducting medium is shown with a d.c. magnetic field H_0 directed along the z axis (note that for simplicity we have ignored curvature of the electron trajectories due to H_0 in figure 14).

In the absence of any electric fields and thermal gradients, the electrons in the infinite medium will be in thermal equilibrium with their surroundings; ie, their phase space distribution function $f(\vec{r}, \vec{k}, t)$ is just the Fermi-Dirac distribution function f_0 .

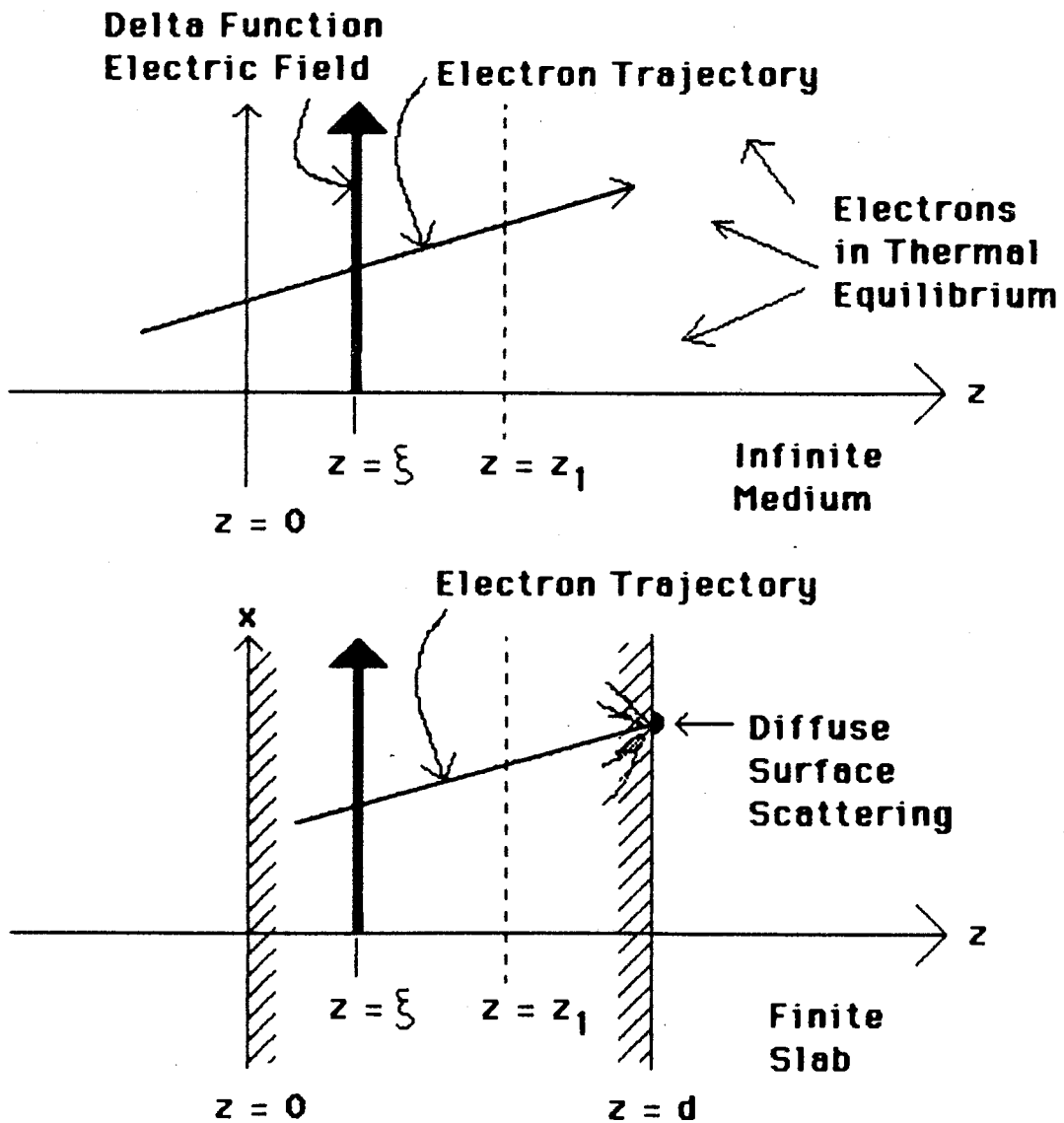


Fig. 14 The equivalence of a slab with diffusely scattering faces and an infinite medium. Inserting diffusely scattering boundaries at $z = 0$ and $z = d$ in an infinite medium leaves the current response $K_{\pm}^{\infty}(|z-\xi|)$ invariant in the region $0 \leq z \leq d$ provided $0 \leq \xi \leq d$. This correspondence only occurs in the perpendicular configuration where H_0 does not affect the motion of electrons in the z direction

Suppose we place a delta function electric field sheet at a point $z = \xi$ ($0 \leq \xi \leq d$) and calculate the current response $K_{\pm}^{\infty}(|z_1 - \xi|)$ at a point $z_1 > \xi$ ($0 \leq z_1 \leq d$). Only electrons from the region $z < \xi$ with $v_z > 0$ can pass through the electric field sheet and contribute to the current response at z_1 . All other electrons that pass through z_1 will remain in thermal equilibrium with their surroundings, continue to obey the Fermi-Dirac distribution function, and not contribute to $K_{\pm}^{\infty}(|z_1 - \xi|)$.

If we now insert diffusely scattering boundaries at $z = 0$ and $z = d$, the current response at z_1 will remain unchanged. By definition, any electron that collides with a diffusely scattering boundary emerges from the collision in thermal equilibrium with its surroundings^{11, 22}. We therefore conclude that $K_{\pm}(z, \xi) = K_{\pm}^{\infty}(|z - \xi|)$ in a finite slab with diffusely scattering surfaces.

It is important to note that this correspondence only occurs in the perpendicular configuration where the d.c. magnetic field H_0 does not affect the motion of the conduction electrons in the z direction.

Having determined the form of the kernels, we can write the

boundary value problem as

$$E''(z) + [2i\mu_{\pm}/(\sigma_0 \delta_0^2)] j(z) = 0 \quad [5.1]$$

$$j(z) = \int_0^d K(|z-\xi|) E(\xi) d\xi \quad [5.2]$$

$$h(0) = 1; h(d) = 0 \quad [5.3]$$

where (see page 70)

$$K(z) = \frac{3}{4} \frac{\sigma_0}{\ell} \int_0^{\infty} \left(\frac{1}{y} - \frac{1}{y_3} \right) dy e^{-LAX \frac{z}{\ell} y} \quad [5.4]$$

and, for convenience, we have dropped all \pm subscripts, the ∞ superscript on the kernels $K_{\pm}^{\infty}(|z-\xi|)$, and written $[1-i(\omega \pm \omega_c)\tau] = LAX$.

5.3 Reduction to a Set of Simultaneous Equations

The electric field distributions $E_{\pm}(z)$ will be calculated approximately on a uniform grid of $N+1$ equally spaced points z_i defined by

$$z_i = \Delta \cdot i \quad [5.5]$$

where $\Delta = d/N$ (see figure 15).

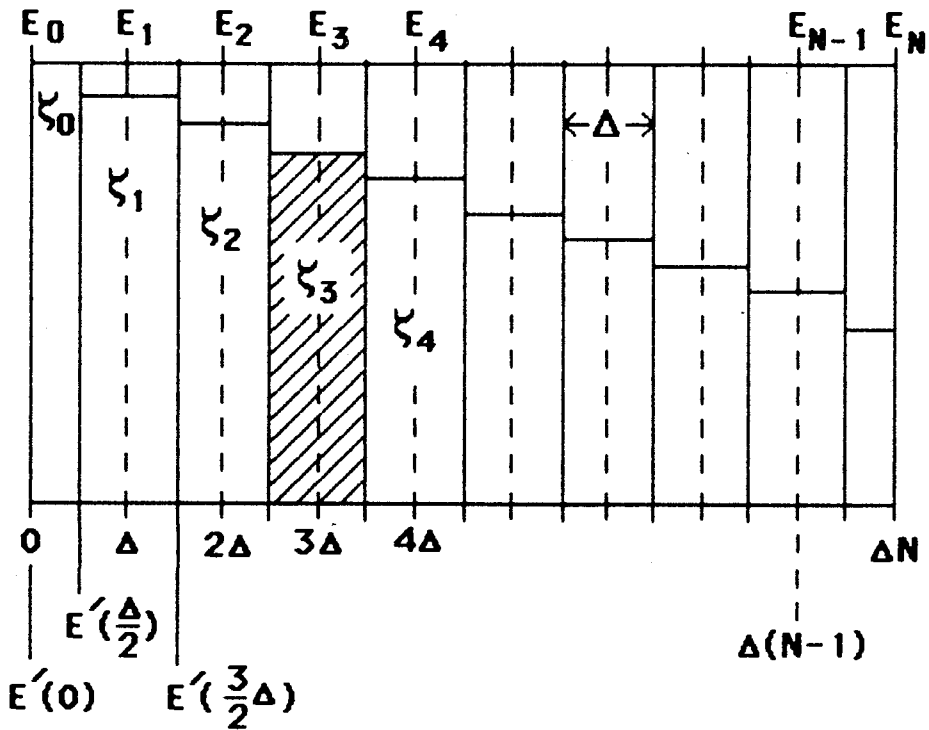


Fig. 15 The diffuse scattering problem is solved numerically by subdividing the slab up into a series of strips and calculating the approximate electric field and current density in each strip

We begin by dividing the slab up into $N+1$ strips such that each of the interior points z_1 to z_{N-1} are at the midpoint of strips of width Δ and the endpoints z_0 and z_N are at the edges of half strips of width $\Delta/2$. The strip containing the i th point z_i shall be referred to as ξ_i .

Integrating [5.1] over each strip ξ_i yields:

$$\xi_{i=0}: \quad E'(\Delta/2) - E'(0) = -2i\mu/(\sigma_0\delta_0^2) \cdot (\Delta \cdot j_0/2) \quad [5.6]$$

$$\xi_{i=1, N-1}: \quad E'(\Delta[i+1/2]) - E'(\Delta[i-1/2]) = -2i\mu/(\sigma_0\delta_0^2) \cdot (\Delta \cdot j_i) \quad [5.7]$$

$$\xi_{i=N}: \quad E'(d) - E'(d-\Delta/2) = -2i\mu/(\sigma_0\delta_0^2) \cdot (\Delta \cdot j_N/2) \quad [5.8]$$

where j_i ($i=0, N$) is the average current density in strip ξ_i ; ie,

$$\xi_{i=0}: \quad j_0 = (2/\Delta) \int_0^{\Delta/2} j(z) dz \quad [5.9]$$

$$\xi_{i=1, N-1}: \quad j_i = (1/\Delta) \int_{z_i-\Delta/2}^{z_i+\Delta/2} j(z) dz \quad [5.10]$$

$$\xi_{i=N}: \quad j_N = (2/\Delta) \int_{d-\Delta/2}^d j(z) dz \quad [5.11]$$

Equations [5.6]-[5.8] express the average current density in the strip ξ_i in terms of a difference between electric field

derivatives at the edges of the strip. Referring to figure 15 we see that the electric field derivatives at the edges of each strip may be approximated using the electric field values $E(z_i) = E_i$ and the usual central difference formulae for numerical differentiation⁴²:

$$E'(\Delta[i-1/2]) = (E_i - E_{i-1})/\Delta; \quad i=1,N \quad [5.12]$$

$$E'(\Delta[i+1/2]) = (E_{i+1} - E_i)/\Delta; \quad i=0,N-1 \quad [5.13]$$

Using [5.12]-[5.13] we can re-write [5.6]-[5.8] as

$$\xi_{i=0}: \quad E_1 - E_0 - \Delta \cdot E'(0) = -2i\mu/(\sigma_0 \delta_0^2) \cdot \Delta^2 \cdot j_0/2 \quad [5.14]$$

$$\xi_{i=1,N-1}: \quad E_{i+1} - 2E_i + E_{i-1} = -2i\mu/(\sigma_0 \delta_0^2) \cdot \Delta^2 \cdot j_i \quad [5.15]$$

$$\xi_{i=N}: \quad \Delta \cdot E'(d) - E_N + E_{N-1} = -2i\mu/(\sigma_0 \delta_0^2) \cdot \Delta^2 \cdot j_N/2 \quad [5.16]$$

The average current densities j_i can be expressed in terms of the electric fields E_i . If we assume that the electric field $E(z)$ in a strip ξ_j is constant, and equal to E_j , then the

current density $j(z)$ defined by equation [5.2] can be written as

$$\begin{aligned}
 j(z) &= \int_0^d K(|z-\xi|)E(\xi)d\xi \\
 &= \left[\int_0^{\Delta/2} K(|z-\xi|)d\xi \right] E_0 \\
 &\quad + \left[\int_{\Delta/2}^{3\Delta/2} K(|z-\xi|)d\xi \right] E_1 \\
 &\quad + \dots \\
 &\quad + \left[\int_{d-\Delta/2}^d K(|z-\xi|)d\xi \right] E_N
 \end{aligned}$$

or, more compactly,

$$j(z) = K_j(z)E_j \quad [5.17]$$

where the double index j is summed from 0 to N and we have defined

$$K_j(z) = \int_{\xi_j} K(|z-\xi|)d\xi \quad [5.18]$$

as the integral of the kernel over the the strip ξ_j . Physically, $K_j(z)$ is just the current response at a point z due to a unit amplitude electric present in the strip ξ_j .

Inserting [5.17] into the expressions [5.9]-[5.11] for the average current density in a strip ξ_i gives us

$$\xi_{i=0}: \quad j_0 = (2/\Delta) I_{0j} E_j \quad [5.19]$$

$$\xi_{i=1, N-1}: \quad j_i = (1/\Delta) I_{ij} E_j \quad [5.20]$$

$$\xi_{i=N}: \quad j_N = (2/\Delta) I_{Nj} E_j \quad [5.21]$$

where, again, the double index j is summed from 0 to N . The quantities I_{ij} are defined as

$$I_{ij} = \int_{\xi_i} \int_{\xi_j} K(|z-\xi|) d\xi dz \quad [5.22]$$

and shall be referred to as integrated current elements.

Physically, I_{ij} is the net current response in the strip ξ_i due to a unit amplitude electric field in the strip ξ_j . The I_{ij} are evaluated in section 5.4.

We obtain a set of simultaneous equations for the $N+1$ electric field points by substituting [5.19]-[5.21] into

[5.14]-[5.16]:

$$\xi_{i=0}: \quad E_1 - E_0 - \Delta \cdot E'(0) = -2i\mu/(\sigma_0 \delta_0^2) \cdot \Delta \cdot I_{0j} E_j \quad [5.23]$$

$$\xi_{i=1, N-1}: \quad E_{i+1} - 2E_i + E_{i-1} = -2i\mu/(\sigma_0 \delta_0^2) \cdot \Delta \cdot I_{ij} E_j \quad [5.24]$$

$$\xi_{i=N}: \quad \Delta \cdot E'(d) - E_N + E_{N-1} = -2i\mu/(\sigma_0 \delta_0^2) \cdot \Delta \cdot I_{Nj} E_j \quad [5.25]$$

where j is summed from 0 to N . The equations are written out in matrix notation in figure 16.

5.4 Incorporation of Boundary Conditions

The boundary conditions $h(0) = 1$ and $h(d) = 0$ are incorporated into the simultaneous equations through the electric field derivatives at the front and the rear of the slab. Using equation [4.2] we find

$$E'(0) = \pm(\omega\mu/c)h(0) = \pm(\omega\mu/c) \quad [5.26]$$

$$E'(d) = \pm(\omega\mu/c)h(d) = 0 \quad [5.27]$$

This leads to a set of $N+1$ simultaneous equations for the $N+1$ electric field values E_i . Once the integrated current elements I_{ij} have been calculated, the equations can be solved

$$\begin{bmatrix} -1 & 1 & 0 & 0 & \dots & 0 & 0 & 0 \\ 1 & -2 & 1 & 0 & \dots & \dots & \dots & \dots \\ 0 & 1 & -2 & 1 & \dots & \dots & \dots & \dots \\ \dots & \dots & \dots & \dots & \dots & \dots & \dots & \dots \\ 0 & 0 & 0 & 0 & \dots & 0 & 0 & 1 & -1 \end{bmatrix} + \frac{2i\mu\Delta}{\sigma_0\delta_0} \begin{bmatrix} I_{00} & I_{01} & I_{02} & \dots & I_{0,N-1} & I_{0N} \\ I_{10} & I_{11} & I_{12} & \dots & I_{1,N-1} & I_{1N} \\ \dots & \dots & \dots & \dots & \dots & \dots \\ \dots & \dots & \dots & \dots & \dots & \dots \\ I_{N0} & I_{N1} & I_{N2} & \dots & I_{N,N-1} & I_{N,N} \end{bmatrix} \begin{bmatrix} E_0 \\ E_1 \\ \dots \\ \dots \\ E_N \end{bmatrix} = \Delta \begin{bmatrix} E'(0) \\ 0 \\ \dots \\ 0 \\ -E'(d) \end{bmatrix}$$

Fig. 16 Matrix equation for the N+1 electric field values E_i across the slab.

by Gaussian elimination or by some other numerical method. However, the speed and accuracy of any algorithm used to solve simultaneous equations depends on the number of equations. In general, the more equations to solve, the longer the solution takes, and the more chance there is of accumulated round-off and/or truncation error spoiling the results. It is therefore desirable to keep the number of equations to solve as small as possible.

In our case, we may reduce the number of equations by one if we change the front surface boundary condition from $h(0) = 1$ to $E(0) = 1$. In that case, $E_0 = 1$ and the simultaneous equations [5.23]-[5.25] become

$$\Delta \cdot E'(0) = E_1 - 1 + 2i\mu/(\sigma_0 \delta_0^2) \cdot \Delta \cdot (I_{00} + I_{0k} E_k) \quad [5.28]$$

$$E_2 - 2E_1 + 1 + 2i\mu/(\sigma_0 \delta_0^2) \cdot \Delta \cdot (I_{10} + I_{1k} E_k) = 0 \quad [5.29]$$

$$E_{i+1} - 2E_i + E_{i-1} + [2i\mu_{\pm}/(\sigma_0 \delta_0^2)] \cdot \Delta \cdot (I_{i0} + I_{ik} E_k) = 0 \quad [5.30]$$

$$-E_N + E_{N-1} + [2i\mu_{\pm}/(\sigma_0 \delta_0^2)] \cdot \Delta \cdot (I_{N0} + I_{Nk} E_k) = 0 \quad [5.31]$$

where i runs from 2 to $N-1$ in [5.30] and the double index k is summed over from 1 to N in all four equations. Equations [5.29]-[5.31] uniquely determine the electric field values E_1 to E_N . The equations are written out in matrix form in figure 17. The remaining equation [5.28] will give us $E'(0)$ once the

$$\begin{bmatrix} -2 & 1 & 0 & 0 & \dots & \dots & \dots & \dots & \dots & \dots \\ 1 & -2 & 1 & 0 & \dots & \dots & \dots & \dots & \dots & \dots \\ 0 & 1 & -2 & 1 & \dots & \dots & \dots & \dots & \dots & \dots \\ \dots & \dots & \dots & \dots & 1 & -2 & 1 & 0 & \dots & \dots \\ \dots & \dots & \dots & \dots & \dots & \dots & 0 & 1 & -2 & 1 \\ 0 & 0 & 0 & \dots & \dots & \dots & 0 & 0 & 1 & -1 \end{bmatrix} + \frac{2i\mu\Delta}{\sigma_0\delta_0} \begin{bmatrix} I_{11} & I_{12} & \dots & I_{1,N-1} & I_{1N} \\ I_{21} & I_{22} & \dots & \dots & \dots \\ \dots & \dots & \dots & \dots & \dots \\ \dots & \dots & \dots & \dots & \dots \\ I_{N1} & I_{N2} & \dots & I_{N,N-1} & I_{N,N} \end{bmatrix} \begin{bmatrix} E_1 \\ E_2 \\ \dots \\ \dots \\ E_N \end{bmatrix} = - \frac{2i\mu\Delta}{\sigma_0\delta_0} \begin{bmatrix} I_{10} \\ I_{20} \\ \dots \\ \dots \\ I_{N0} \end{bmatrix} - \begin{bmatrix} 1 \\ 0 \\ \dots \\ \dots \\ 0 \end{bmatrix}$$

Fig. 17 Modified Matrix Equation for the N electric field values E_1 to E_N when the boundary conditions are changed to $E(0) = 1$ and $h(d) = 0$.

equations have been solved for E_1 to E_N . This can be used in equation [4.2] to determine the value of $h(0)$ corresponding to $E(0) = 1$. To recover the electric fields associated with the original boundary conditions $h(0) = 1$, $h(d) = 0$ we simply divide the solutions E_i ($i=1,N$) by $h(0)$, and define E_0 as $1/h(0)$.

5.5 The Integrated Current Elements

All that remains is to define the $(N+1)^2$ integrated current elements I_{ij} ($i=0,N; j=0,N$) defined in section 5.3 as

$$I_{ij} = \int_{\xi_i} \int_{\xi_j} K(|z-\xi|) d\xi dz \quad [5.22]$$

where \int_{ξ_i} represents an integration over z in the strip ξ_i and \int_{ξ_j} represents an integration over ξ in the strip ξ_j . The translational invariance of the kernel considerably reduces the number of elements I_{ij} we must calculate. For a slab divided up as shown in figure 15, we will find that all $(N+1)^2$ elements can be obtained by symmetry from only $2N$ elements.

Consider the total integrated current matrix $[I_{ij}]$ shown in figure 18 for $N = 5$. Since z and ξ enter the kernel only through the $|z-\xi|$ then

$$I_{ij} = I_{ji} \quad [5.32]$$

and the matrix is symmetric. This reduces the number of

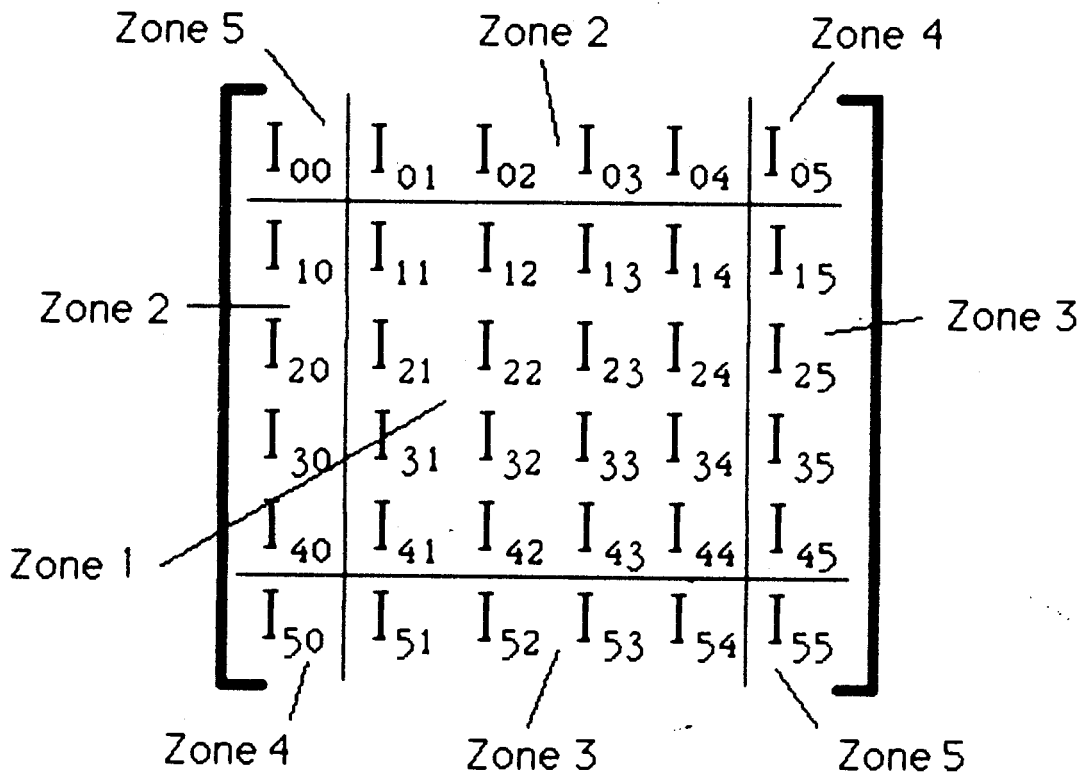


Fig. 18 The Total Integrated Current Matrix for $N = 5$. The matrix is divided into 5 zones. The elements within each zone are related to one another by symmetry. Using symmetry, all $(N+1)^2$ elements may be obtained from only $2N$ of the elements.

elements to calculate by roughly one half. We may further reduce this number by subdividing $[I_{ij}]$ into the 5 zones shown in figure 18 and considering what symmetry relationships exist amongst the various I_{ij} in each zone.

Zone 1: Both Strips Have Width Δ

This is the largest zone with a total of $(N-1)^2$ elements given by

$$I_{ij} = \int_{z_i - \frac{\Delta}{2}}^{z_i + \frac{\Delta}{2}} \int_{z_j - \frac{\Delta}{2}}^{z_j + \frac{\Delta}{2}} K(|z-\xi|) d\xi dz \quad [5.33]$$

where i and j can take on values from 1 to $N-1$.

The translational invariance of the kernel causes the I_{ij} to depend only on the absolute distance between the strips ξ_i and ξ_j . This gives the symmetry relationship

$$I_{ij} = I_{|i-j|+1,1} \quad [5.34]$$

and we can see that all $(N-1)^2$ elements may be found by by calculating only the $(N-1)$ elements $I_{11}, I_{21}, I_{31}, \dots, I_{N-1,1}$ and then applying [5.34]. The symmetry relationship says that all elements along a diagonal in zone 1 of $[I_{ij}]$ are identical; ie, $I_{11} = I_{22} = I_{33} = \dots = I_{N-1,N-1}, I_{12} = I_{23} = I_{34} = \dots = I_{N-2,N-1}$, etc.

The proof of [5.34] is simple. We change variables in [5.33] from (z, ξ) to (z', ξ') where $\xi' = z_{i+1} - z$ and

$z' = z_{i+1} - \xi$. The result is

$$I_{ij} = \int_{|z_i - z_j| + \frac{\Delta}{2}}^{|z_i - z_j| + \frac{3\Delta}{2}} \int_{\frac{\Delta}{2}}^{\frac{3\Delta}{2}} K(|z' - \xi'|) d\xi' dz' \quad [5.35]$$

which is just $I_{|i-j|+1,1}$ (we write $|z_i - z_j|$ instead of $(z_i - z_j)$ in the integration limits because [5.32] demands $I_{ij} = I_{ji}$).

Note that while [5.35] proves the symmetry relation [5.34], calculation of the I_{ij} is made easier if we employ translational invariance once more to write [5.35] as

$$I_{ij} = \int_{|z_i - z_j| - \frac{\Delta}{2}}^{|z_i - z_j| + \frac{\Delta}{2}} \int_{-\frac{\Delta}{2}}^{\frac{\Delta}{2}} K(|z - \xi|) d\xi dz \quad [5.36]$$

(we can also obtain [5.36] directly from [5.33] by the transformation $z' = z_i - \xi$ and $\xi' = z_i - z$).

Hence the $(N-1)$ elements $I_{11}, I_{21}, I_{31}, \dots, I_{N-1,1}$ needed to calculate all $(N-1)^2$ elements I_{ij} of zone 1 are given by

$$I_{i1} = \int_{z_i - 3\Delta/2}^{z_i - \Delta/2} \int_{-\Delta/2}^{\Delta/2} K(|z - \xi|) d\xi dz \quad [5.37]$$

Zones 2 and 3: One Strip has Width Δ , the Other has Width $\Delta/2$

There are $2(N-1)$ elements $I_{i0} = I_{0i}$ ($i=1, N-1$) in zone 2 and $2(N-1)$ elements $I_{Ni} = I_{iN}$ ($i=1, N-1$) in zone 3 (see figure 18).

By definition

$$I_{i0} = \int_{z_i - \frac{\Delta}{2}}^{z_i + \frac{\Delta}{2}} \int_0^{\frac{\Delta}{2}} K(|z-\xi|) d\xi dz \quad [5.38]$$

$$I_{Ni} = \int_{d-\Delta/2}^d \int_{z_i - \Delta/2}^{z_i + \Delta/2} K(|z-\xi|) d\xi dz \quad [5.39]$$

and the translational invariance of the kernel may be used to relate the elements of zones 2 and 3 by

$$I_{Ni} = I_{N-i,0} \quad [5.40]$$

and only the (N-1) elements $I_{10}, I_{20}, \dots, I_{N-1,0}$ need be calculated to find all 4(N-1) elements. The proof of [5.40] requires a change of variable in [5.39] from (z, ξ) to (z', ξ') using $z' = d - \xi$ and $\xi' = d - z$.

Zones 4 and 5: Both strips have width $\Delta/2$

There are the four elements $I_{00}, I_{0N}, I_{N0},$ and I_{NN} . Again, by the translational invariance of the kernel,

$$I_{00} = I_{NN} = \int_0^{\Delta/2} \int_0^{\Delta/2} K(|z-\xi|) d\xi dz \quad [5.41]$$

$$I_{N0} = I_{0N} = \int_{d-\Delta/2}^d \int_0^{\Delta/2} K(|z-\xi|) d\xi dz \quad [5.42]$$

and only two of the four elements need to be calculated.

5.6 Evaluation of the Integrated Current Elements

In total, only $2N$ elements must be calculated in order to fill the entire $(N+1) \times (N+1)$ integrated current matrix of figure 18 ($N-1$ elements for zone 1, $N-1$ elements for zones 2 and 3, and 2 elements for zones 4 and 5). In figure 19 we show how to fill the $N = 5$ current matrix of figure 18 using the symmetry relationships.

The $2N$ elements are found by evaluating [5.37], [5.38], [5.41], and [5.42] using the kernel $K(|z-\xi|)$ defined by [5.4]. We consider the integrated current elements of each zone in turn:

Zone 1: ($N-1$) elements I_{i1} ; $i = 1, N-1$

The current elements I_{i1} are given by equation [5.37]. When $i \neq 1$ the electric field strip does not coincide with the integrated current strip and we may set $K(|z-\xi|) = K(z-\xi)$ in [5.37]. The integrals over z and ξ are then easily carried out

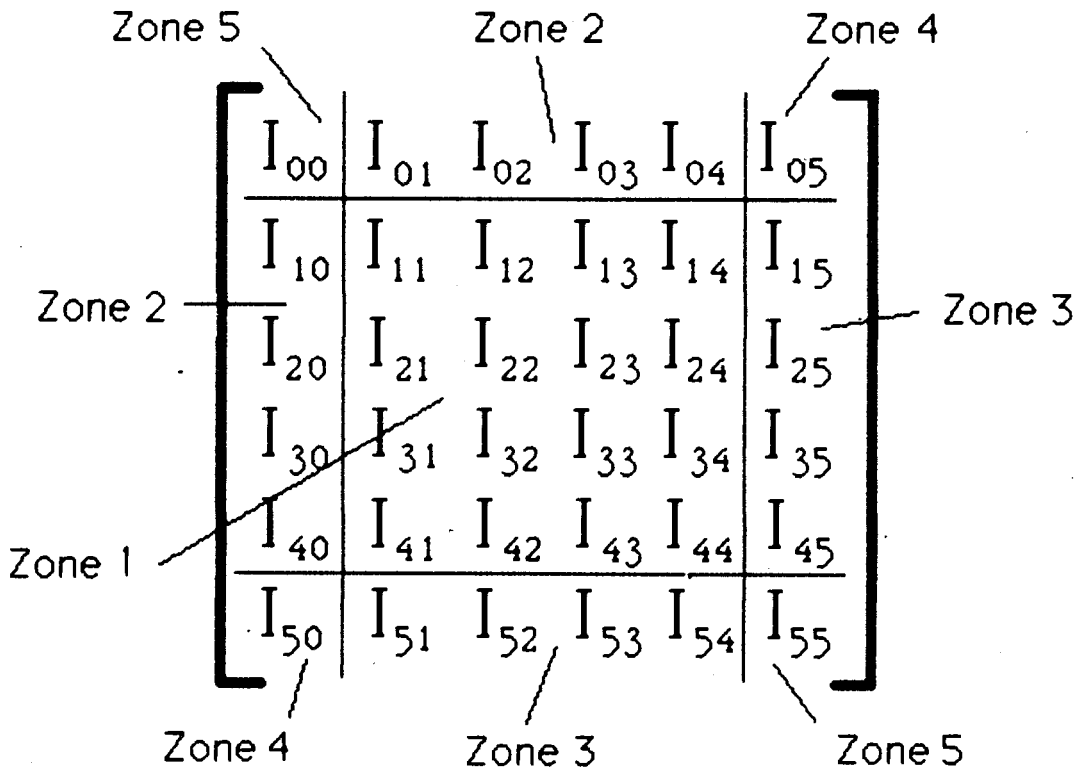


Fig. 20 The Total Integrated Current Matrix for $N = 5$. The matrix is filled according to the symmetry relationships derived in section 5.5 Only $2N$ of the $(N+1)^2$ elements are needed to fill the matrix

to get

$$I_{i1} = -\frac{3}{4} \frac{\sigma_0 l}{LAX^3} \int_1^{\infty} \left(\frac{1}{y^3} - \frac{1}{y^5} \right) dy \left[e^{-LAX \left(\frac{z_i - \Delta}{l} \right) y} - e^{-LAX \left(\frac{z_i - 2\Delta}{l} \right) y} - e^{-LAX \left(\frac{z_i}{l} \right) y} + e^{-LAX \left(\frac{z_i - \Delta}{l} \right) y} \right]$$

or, defining the function $G(x)$ as

$$G(x) = \int_1^{\infty} \left(\frac{1}{y^3} - \frac{1}{y^5} \right) dy e^{-xy} \quad [5.43]$$

we can write

$$I_{i1} = \frac{3}{4} \frac{\sigma_0 l}{LAX^3} [G(A_1) - 2G(A_2) + G(A_3)]; \quad i \neq 1 \quad [5.45]$$

where

$$A_1 = LAX \cdot (z_i) / l$$

$$A_2 = LAX \cdot (z_i - \Delta) / l$$

$$A_3 = LAX (z_i - 2\Delta) / l$$

The function $G(x)$ is discussed in section 5.6.2. Note that this function is not the same as the electric field functions $G_{\pm}(z)$

defined in chapter 2.

When $i = 0$ the two strips overlap and we must break up the integral over ξ in [5.37] into two parts depending on whether $z - \xi > 0$ or $z - \xi < 0$. The result is

$$= \int_{-\Delta/2}^{\Delta/2} dz' \left[\int_{-\Delta/2}^z K(z' - \xi) d\xi + \int_z^{\Delta/2} K(\xi - z') d\xi \right]$$

$$= \frac{\sigma_0}{LAX} \left[\Delta + \frac{3}{2} \frac{l}{LAX} \left\{ G(LAX \frac{\Delta}{l}) - \frac{1}{4} \right\} \right] \quad [5.46]$$

where $G(x)$ is defined by [5.43] and we have used the fact $G(0) = 1/4$.

Zones 2 and 3: (N-1) elements I_{i0} ; $i = 1, N-1$

The current elements I_{i0} are given by [5.38] and evaluated exactly like the I_{i1} ($i \neq 1$); ie, we set $K(|z-\xi|) = K(z-\xi)$ and integrate. The result is

$$I_{i0} = \frac{3}{4} \frac{\sigma_0 l}{LAX^3} [G(A_4) - G(A_5) + G(A_6) - G(A_7)] \quad [5.47]$$

where

$$A_4 = LAX (z_i + \Delta/2)/l$$

$$A_5 = LAX (z_i)/l$$

$$A_6 = LAX (z_i - \Delta)/l$$

$$A_7 = LAX (z_i - \Delta/2)/l$$

Zones 4 and 5: 2 elements I_{00} and I_{N0}

I_{00} is given by [5.41] and I_{N0} is given by [5.42]. We evaluate I_{00} in the same way we evaluated I_{11} (see equation [5.46]):

$$I_{00} = \int_0^{\Delta/2} dz' \left[\int_0^z K(z'-\xi) d\xi + \int_z^{\Delta/2} K(\xi-z') d\xi \right]$$

$$= \frac{\sigma_0}{LAX} \left[\frac{\Delta}{2} + \frac{3}{2} \frac{l}{LAX} \left\{ G(LAX \frac{\Delta}{2l}) - \frac{1}{4} \right\} \right] \quad [5.48]$$

We evaluate I_{N0} like I_{i1} ($i \neq 1$) by replacing $K(|z-\xi|)$ by $K(z-\xi)$ and integrating:

$$I_{N0} = \frac{3}{4} \frac{\sigma_0 l}{LAX^2} [G(A_8) - 2G(A_9) + G(A_{10})] \quad [5.49]$$

where

$$A_8 = LAX (d/l)$$

$$A_9 = LAX (d - \Delta/2)/l$$

$$A_{10} = LAX (d - \Delta)/l$$

5.6.1 Summary of Integrated Current Elements

Zone 1: (N-1) elements I_{i1} ; $i = 1, N-1$

$$I_{i1} = \frac{\sigma_0}{LAX} \left[\Delta + \frac{3}{2} \frac{l}{LAX} \left\{ G\left(LAX \frac{\Delta}{l}\right) - \frac{1}{4} \right\} \right] \quad [5.46]$$

$$I_{i1} = \frac{3}{4} \frac{\sigma_0 l}{LAX^2} [G(A_1) - 2G(A_2) + G(A_3)]; \quad i \neq 1 \quad [5.45]$$

where

$$A_1 = LAX \cdot (z_i) / l$$

$$A_2 = LAX \cdot (z_i - \Delta) / l$$

$$A_3 = LAX (z_i - 2\Delta) / l$$

Symmetry Relations: $I_{ij} = I_{|i-j|+1,1}$; $(i, j=1, N-1)$

Zones 2 and 3: (N-1) elements I_{i0} ; $i = 1, N-1$

$$I_{i0} = \frac{3}{4} \frac{\sigma_0 l}{LAX^2} [G(A_4) - G(A_5) + G(A_6) - G(A_7)] \quad [5.47]$$

where

$$A_4 = LAX (z_i + \Delta/2)/l$$

$$A_5 = LAX (z_i)/l$$

$$A_6 = LAX (z_i - \Delta)/l$$

$$A_7 = LAX (z_i - \Delta/2)/l$$

Symmetry Relations: $I_{i0} = I_{0i}$; $I_{Ni} = I_{N-i,0}$; $I_{Ni} = I_{iN}$

Zones 4 and 5: 2 elements I_{00} and I_{N0}

$$I_{00} = \frac{\sigma_0}{LAX} \left[\frac{\Delta}{2} + \frac{3}{2} \frac{l}{LAX} \left\{ G(LAX \frac{\Delta}{2l}) - \frac{1}{4} \right\} \right] \quad [5.48]$$

$$I_{N0} = \frac{3}{4} \frac{\sigma_0 l}{LAX^2} [G(A_8) - 2G(A_9) + G(A_{10})] \quad [5.49]$$

where

$$A_8 = LAX (d/l)$$

$$A_9 = LAX (d - \Delta/2)/l$$

$$A_{10} = LAX (d - \Delta)/l$$

Symmetry Relations: $I_{00} = I_{NN}$; $I_{N0} = I_{ON}$

5.6.2 The Function $G(x)$

The function $G(x)$ was defined as

$$G(x) = \int_1^{\infty} \left(\frac{1}{y^3} - \frac{1}{y^5} \right) e^{-xy} dy \quad [5.50]$$

repeatedly integrating [5.50] by parts yields:

$$G(x) = \left[\left((x-1)x - 10 \right) x + 6 \right] \frac{e^{-x}}{24} + \frac{1}{2} x^2 \left(1 - \frac{1}{12} x^2 \right) E_1(x) \quad [5.51]$$

where

$$E_1(x) = \int_1^{\infty} \frac{e^{-xy}}{y} dy = \int_x^{\infty} \frac{e^{-t}}{t} dt \quad [5.52]$$

is the exponential integral for a complex argument. A numerical procedure for evaluating $E_1(x)$ is discussed in Appendix E.

The exponential integral has a branch cut along the negative real axis and goes to infinity as x goes to zero. It's

analytic everywhere else. In equations [5.46]-[5.49] for the integrated current elements, all the arguments for $G(\chi)$ had positive real parts. Hence, $\text{Re}[\chi]$ is always greater than zero, the G functions needed for the evaluation of the I_{ij} will be analytic, and the I_{ij} will be well defined quantities free from any singularities.

5.7 Recovery of the NSE results

In the limit $\delta/l \gg 1$, the non-local current density expression for a slab with diffusely scattering faces

$$j(z) = \int_0^d K(|z-\xi|) E(\xi) d\xi \quad [5.2]$$

(\pm subscripts suppressed) must reduce to the a.c. form of Ohm's Law:

$$j(z) = \sigma(\omega \pm \omega_c) E(z)$$

where

$$\sigma(\omega \pm \omega_c) = \frac{\sigma_0}{1 - i(\omega \pm \omega_c)\tau}$$

Formally, this is the same as requiring that the kernels $K(|z-\xi|)$ reduce to $\sigma(\omega \pm \omega_c)\delta(z-\xi)$, where $\delta(z-\xi)$ is the Dirac delta function. This gives us a way of checking if our numerical solution will properly reproduce the NSE regime

results. In the NSE regime, the integrated current elements would be defined by

$$I_{ij} = \int_{\xi_i} \int_{\xi_j} \sigma(\omega \pm \omega_c) \delta(z - \xi) d\xi dz \quad [5.53]$$

ie, the net current response in the strip ξ_i is zero unless the unit amplitude electric field is also located in the strip ξ_i . All off-diagonal elements of the integrated current matrix $[I_{ij}]$ will therefore be zero and the diagonal elements will be given by

$$I_{00} = I_{NN} = (\Delta/2) \sigma(\omega \pm \omega_c) \quad [5.54]$$

$$I_{ii} = \Delta \cdot \sigma(\omega \pm \omega_c); \quad i=1, N-1 \quad [5.55]$$

From the definitions [5.46]-[5.49] we see that if we let l go to zero then all the off-diagonal elements will indeed go to zero and the diagonal elements properly reduce to the forms given by [5.54] and [5.55]. The numerical solution will therefore reduce to the NSE solutions of chapter 4 as the mean free path l becomes small.

5.8 The Magnetic Field and Current Density in the Slab

Once the rf electric field distribution has been determined, the rf current densities $j(z_i) = j_i$ at the grid points z_i can be obtained at once from the average current density expressions [5.19] - [5.21]. The rf magnetic fields $h(z_i) = h_i$ at each interior grid point z_i may be obtained by combining the central difference formula for numerical differentiation with the relation between $E'(z)$ and $h(z)$; viz,

$$h_i = \pm \frac{c}{\omega \mu_{\pm}} \frac{[E_{i+1} - E_{i-1}]}{2\Delta} ; i = 1, N-1 \quad [5.56]$$

(\pm subscripts on h_i and E_i suppressed).

If the magnetic field points do not have to be on the same grid as the electric field points, we can calculate the magnetic fields at the edges of each strip ξ_i using the differentiation formula [5.13]:

$$h_{\pm}(z_i + \frac{\Delta}{2}) = \pm \frac{c}{\omega \mu_{\pm}} \frac{[E_{i+1} - E_i]}{\Delta} ; i = 0, N-1 \quad [5.57]$$

(see figure 15).

5.9 Implementation on a Computer

A computer program was written in FORTRAN IV to set-up and solve the modified matrix equation shown in figure 17. When run on an IBM 3081GX, under the Michigan Terminal System (MTS), the program took approximately 2.5 minutes of CPU time to calculate and write out the electric field distributions $G_{\pm}(z)$ corresponding to $d = 5 \mu\text{m}$, $l = 25 \mu\text{m}$, and $N = 100$. Doubling the number of electric field points to $N = 200$ increased the execution time to 4 minutes while setting $N = 700$, increased execution time to 40 minutes.

The program spent the bulk of it's time calculating the $2N$ integrated current elements needed to fill the $N \times N$ equation matrix. For example, when $N = 100$ the program took about 2 minutes out of it's 2.5 minute running time to evaluate the integrated current elements. Only 15 seconds were needed to set-up and solve the matrix equations for $G_{\pm}(z)$ and another 15 seconds were needed for I/O. The main bottleneck is the numerical evaluation of the exponential integral $E_1(\chi)$. (see Appendix E for details of our algorithm). A more efficient algorithm for calculating $E_1(\chi)$ could substantially reduce execution time.

In contrast to the evaluation of the integrated current elements, the solution of the $N \times N$ matrix equation for the electric fields E_1 to E_N in the slab is very fast and efficient because the matrix is diagonally dominant (ie, the diagonal

elements of the matrix are much greater than the off diagonal elements). Matrices of this form can be solved by straightforward Gaussian elimination with backward substitution, the solutions being stable against growth of rounding and truncation errors⁴².

5.9.1 Convergence of the Numerical Solution

Since the execution time of the diffuse scattering program depends on N , it's important to determine how large N must be to accurately calculate the transmission coefficients T_{\pm} . To this end, we used the program to evaluate $G_{\pm}(z)$ and T_{\pm} for various slab thicknesses d , conduction mean free paths l , and electric field points N when $H_0 = 18.55$ kOe (corresponding to FMR in Nickel at 24 GHz). Based on the results of these calculations we concluded that our numerical method will calculate T_{\pm} to within 2 or 3 percent provided N is just large enough to resolve the electric field distribution in the slab. Roughly speaking, this requires Δ , the spacing between successive electric field points in the slab, to be comparable to the rf skin depth δ (ie, $\Delta = d/N \leq \delta$). In practice, we have found a good estimate of the minimum value of N to use for a given slab thickness d is given by

$$N = 2d/|\delta_{\pm}| \quad [5.58]$$

where

$$\delta_{\pm} = \delta_0 / \sqrt{-2i\mu_{\pm}} \quad [4.17]$$

is the effective NSE skin depth for a ferromagnetic metal (see section 4.3.2 in chapter 4).

The convergence of T_{\pm} is illustrated in figures 20 to 22. In figure 20 we plot $|T_{\pm}|$ vs. N for $d = 5 \mu\text{m}$, $l = 25 \mu\text{m}$, and $13 \leq N \leq 200$. In figure 21 we plot $\log_{10}|G_{-}(z)|$ vs. z for $d = 5 \mu\text{m}$, $l = 25 \mu\text{m}$, and $N = 25, 50, 100$, and 200 . In figure 22 we plot $\log_{10}|G_{+}(z)|$ vs. z for $d = 5 \mu\text{m}$, $l = 25 \mu\text{m}$, and $N = 13, 25, 50$, and 200 .

In Nickel, at 24 GHz, $|\delta_{-}(\text{FMR})| \approx 0.1 \mu\text{m}$ while $|\delta_{+}(\text{FMR})| \approx 0.4 \mu\text{m}$. Thus, equation [5.58] predicts that we will need $N = 100$ to get a good estimate of T_{-} and $N = 25$ to get a good estimate of T_{+} .

From figure 20 we see that T_{-} indeed converges to a fixed value near $N \approx 100$ while T_{+} converges to a fixed value near $N \approx 25$. Referring to figures 21 and 22 we see that the values of N that cause the transmission coefficients to stabilize correspond to the values of N that just start to resolve the electric field distributions $G_{\pm}(z)$ in the slab.

In practice, we tended to use $N = 100$ when carrying out transmission calculations on slabs of thickness $d \leq 5 \mu\text{m}$ and $N = 200$ for calculations on slabs of thickness $5 \leq d \leq 10 \mu\text{m}$. For thicker slabs we used $N = 2d/|\delta_{-}|$.

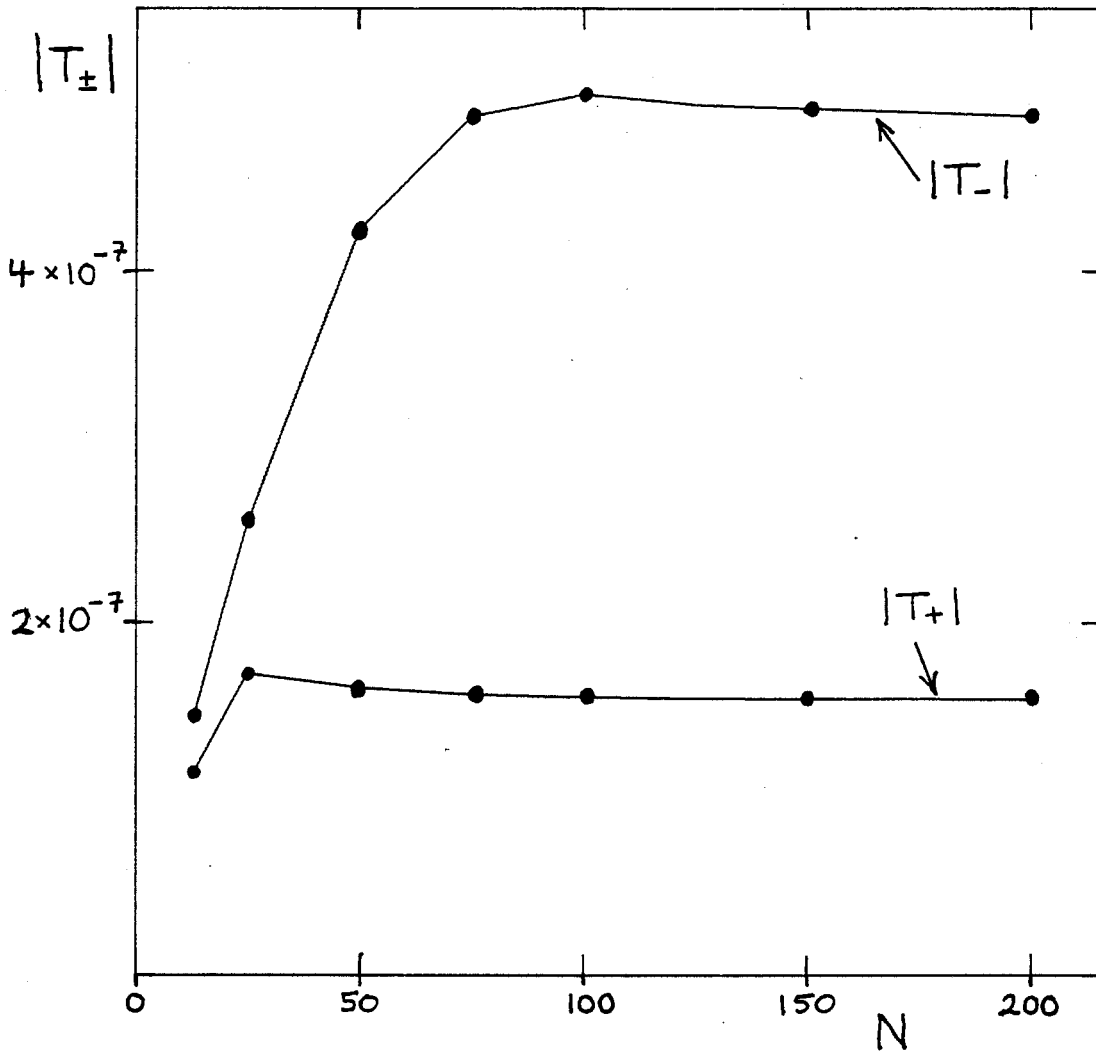


Fig. 20 Plot of $|T_{\pm}|$ vs. N calculated for diffuse surface scattering, $d = 5 \mu\text{m}$, $l = 25 \mu\text{m}$, and the Nickel parameters of Appendix A. Here N is the number of electric field points calculated across the slab.

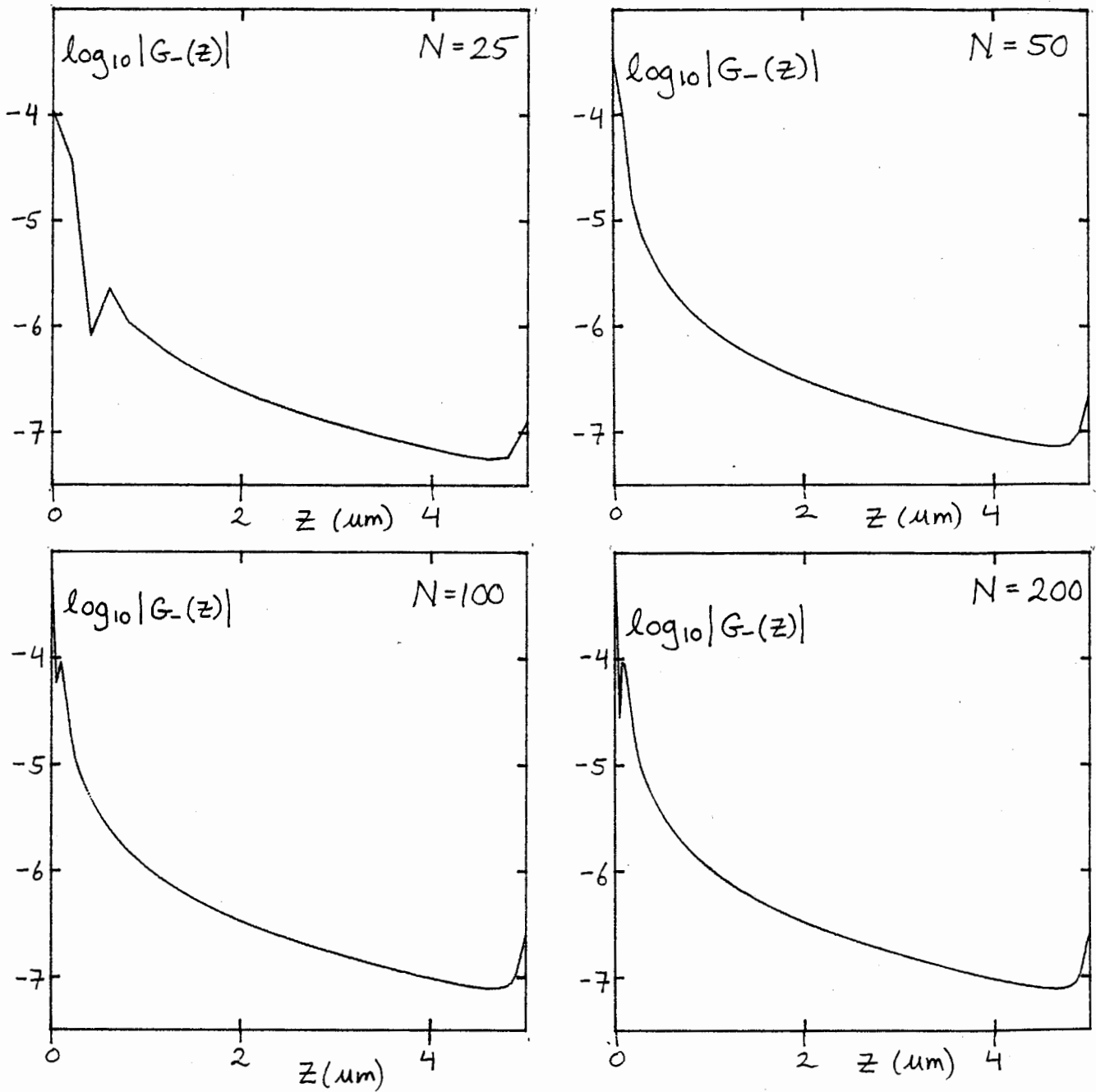


Fig. 21 Plot of $\log_{10}|G_-(z)|$ vs. z calculated for diffuse surface scattering, $d = 5 \mu\text{m}$, $l = 25 \mu\text{m}$, the Nickel parameters of Appendix A and $N = 25, 50, 100,$ and 200 .

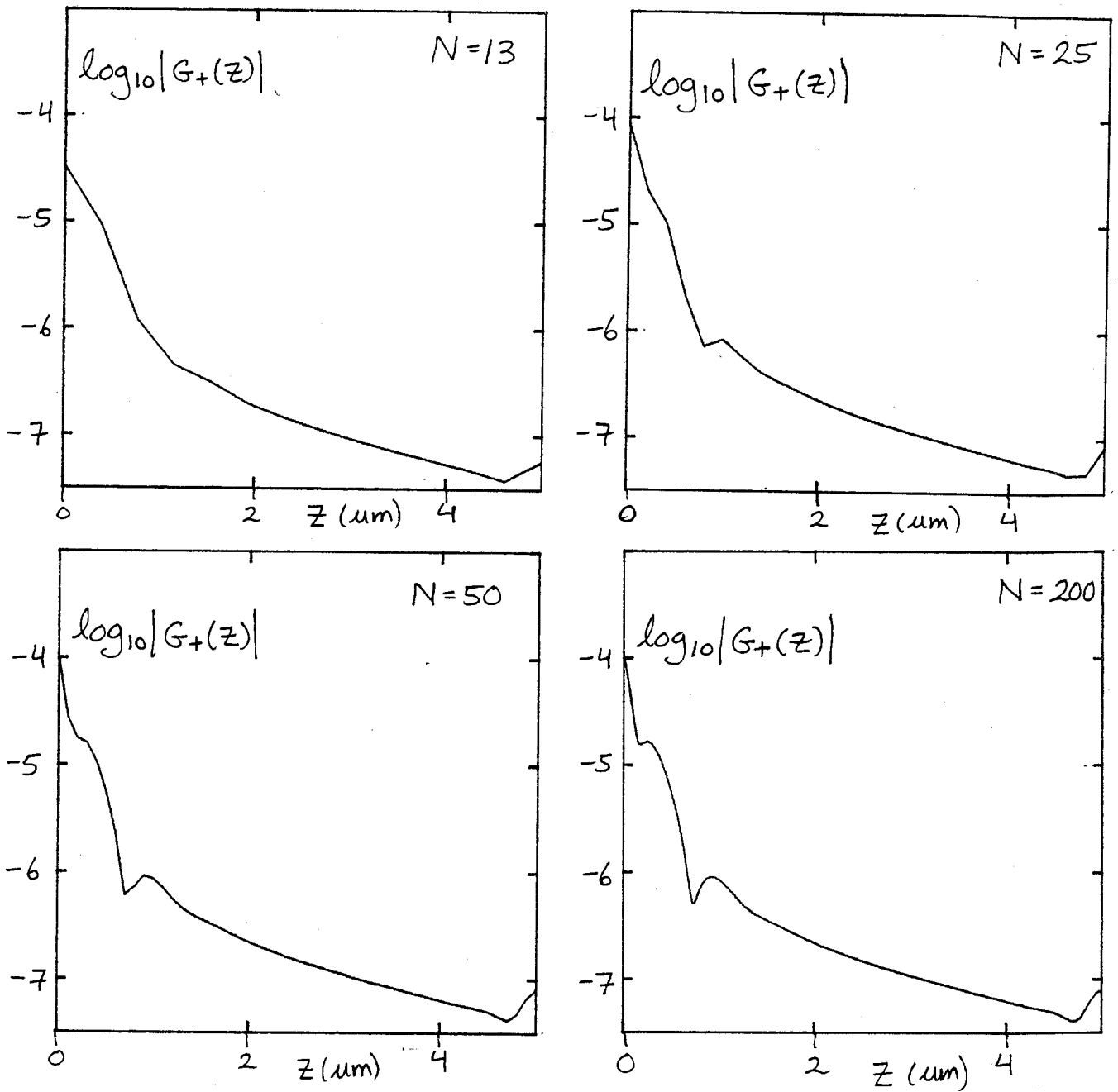


Fig. 22 Plot of $\log_{10}|G_+(z)|$ vs. z calculated for diffuse surface scattering, $d = 5 \mu\text{m}$, $l = 25 \mu\text{m}$, the Nickel parameters of Appendix A and $N = 13, 25, 50,$ and 200 .

6. ELECTRIC FIELD SOLUTION FOR SPECULAR SURFACE SCATTERING

6.1 Introduction

When the surfaces of our slab specularly scatter conduction electrons, Platzmann and Bushcbaum^{2,1} have shown that we can solve the boundary value problem of chapter 2 using fourier transforms methods; the resulting electric field solutions $E_{\pm}(z)$ being expressed as fourier cosine series. Unfortunately, the series solutions tend to converge VERY slowly, making them unsuitable for calculating the electric fields in the slab, and for calculating the microwave transmission through the slab, for arbitrary values of δ/l and d . In order to get around this problem we have re-cast the series solutions into two new forms. One is a much faster converging series suitable for calculating the electric fields in the slab and the other is an integral solution suitable for very fast calculation of the transmission coefficients only.

We describe the solution to our boundary value problem in section 6.2. In section 6.3 we discuss how to transform the series solution into a faster converging form In section 6.4 we show how to convert the series solutions for $G_{\pm}(d)$ into an integral form that can be used to calculate the transmission

coefficients T_{\pm} . An algorithm for calculating the transmission using the integral form is discussed in section 6.5. The integral form was suggested by the technique used by Kogan, Turov, and Ustinov¹⁵ to derive an analytic expression for $G_{\pm}(d)$ in the thick slab limit ($d/\delta \gg 1$, $d/l \gg 1$). In section 6.6 we derive an analytic closed form for the transmission coefficients of a thick ($d/l \gg 1$) slab. This form will prove to be very useful when analyzing the calculated results for specular and diffuse scattering (see chapter 7).

6.2 Solution of the Boundary Value Problem

The boundary value problem we wish to solve was defined on page 54 as

$$E_{\pm}''(z) + [2i\mu_{\pm}/(\sigma_0\delta_0^2)]j_{\pm}(z) = 0 \quad [2.46]$$

$$j_{\pm}(z) = \int_0^d K_{\pm}(z, \xi)E_{\pm}(\xi)d\xi \quad [2.44]$$

$$h_{\pm}(0) = 1; h_{\pm}(d) = 0 \quad [2.48]$$

with the magnetic fields related to the electric fields by

$$E'_{\pm}(z) = \pm(\omega\mu_{\pm}/c) h_{\pm}(z) \quad [6.1]$$

When the surfaces of the slab specularly scatter conduction electrons, Platzmann and Bushcbaum²¹ have shown that the non-local current density expression [2.44] can be replaced by

$$j_{\pm}(z) = \int_{-\infty}^{\infty} K_{\pm}^{\infty}(z, \xi) E_{\pm}(\xi) d\xi \quad [6.2]$$

provided we make $j_{\pm}(z)$ and $E_{\pm}(z)$ even, periodic functions of z with period $2d$ and $h_{\pm}(z)$ an odd, periodic function of z with period $2d$. With the rf fields and currents in this form we can easily solve the boundary value problem via fourier transform methods.

The proof of [6.2] is simple enough. When the surfaces of our slab specularly scatter electrons, the current response at a point z_1 in our finite slab, due to a delta function rf electric field at a point ξ , is identical to the current response at z_1 in an infinite medium filled with an array of delta function electric field sheets placed symmetrically about the planes $z = \pm 2nd$ ($n = 0, 1, 2, 3, \dots$) at the points ξ' .

To see this we note that any possible path a conduction electron can follow to get from $\bar{\xi}$ to \bar{r} in the finite slab corresponds to a unique direct path in the infinite medium that connects z_1 to one or more of the electric field sheets. (see figure 23). We therefore conclude that if arbitrary electric fields $E_{\pm}(z)$ generate current densities $j_{\pm}(z)$ in the finite slab then the even extension of $E_{\pm}(z)$ throughout an infinite conducting medium, plus the condition $E_{\pm}(z \pm 2d) = E_{\pm}(z)$,

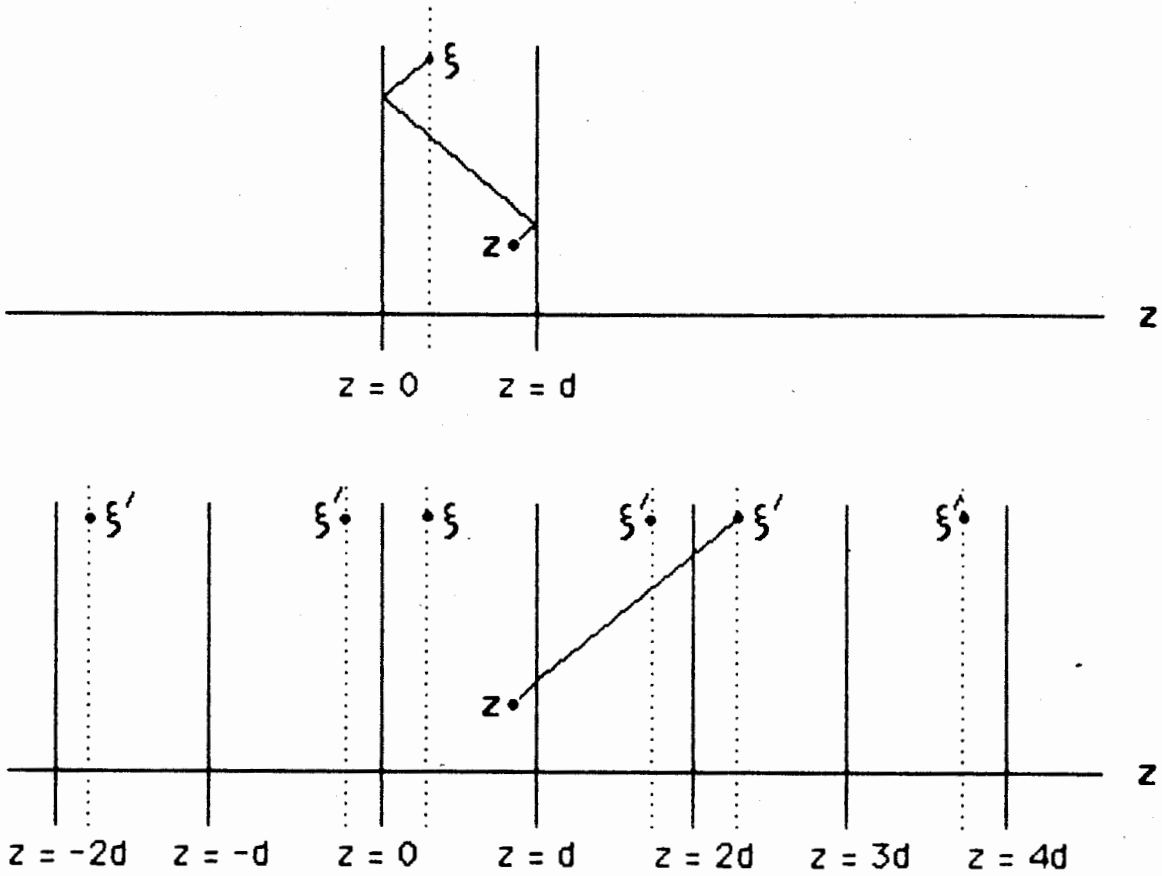


Fig. 23 The current response at \bar{r} in a finite slab, due to a delta function electric field at a point $\bar{\xi}$, is identical to the current response in an infinite medium filled with a periodic, symmetric array of delta function electric fields provided the surfaces of the finite slab specularly scatter conduction electrons and the d.c. magnetic field is perpendicular to the plane of the slab. Only then is there a one to one correspondence between an electron trajectory connecting \bar{r} to $\bar{\xi}$ in the finite slab and some direct path in the infinite medium connecting \bar{r} to one of the electric field points.

generates an identical current response in the region $0 \leq z \leq d$ (see figure 24). Result [6.2] follows immediately because the current response in an infinite medium due to any kind of electric field $E_{\pm}(z)$ is just

$$j_{\pm}(z) = \int_{-\infty}^{\infty} K_{\pm}^{\infty}(z, \xi) E_{\pm}(\xi) d\xi \quad [6.2]$$

where $K_{\pm}^{\infty}(|z-\xi|)$ are the kernels for an infinite medium (see chapter 3).

The solution of the boundary value problem for $E_{\pm}(z)$ is easily carried out using the periodic rf fields and the non-local current density [6.2]. Since $E_{\pm}(z)$ and $j_{\pm}(z)$ are even functions of z and periodic with period $2d$, we can represent them by the fourier cosine series:

$$E_{\pm}(z) = \sum_{n=0}^{\infty} E_{\pm}^n \cos(q_n z) \quad [6.3]$$

$$j_{\pm}(z) = \sum_{n=0}^{\infty} j_{\pm}^n \cos(q_n z) \quad [6.4]$$

where, $q_n = (n\pi)/d; n = \text{integer}$ [6.5]

and the fourier coefficients are defined by

$$E_{\pm}^n = \frac{2 - \delta_{0n}}{d} \int_0^d E_{\pm}(z) \cos(q_n z) dz \quad [6.6]$$

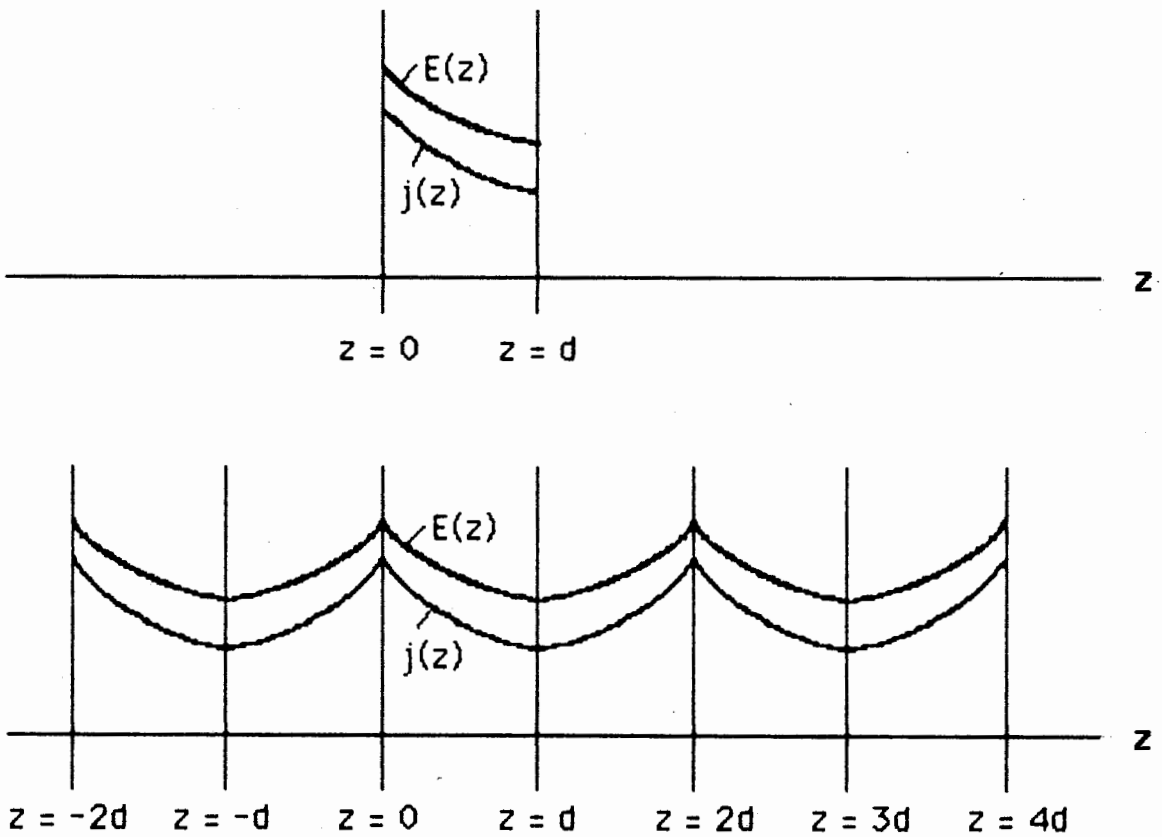


Fig. 24 The current density generated in the finite slab due to an arbitrary electric field is identical to the current response in the region $0 \leq z \leq d$ of an infinite medium filled with the even, periodic extension of the electric field. The period being $2d$.

$$j_{\pm}^n = \frac{2 - \delta_{0n}}{d} \int_0^d j_{\pm}(z) \cos(q_n z) dz \quad [6.7]$$

where δ_{0n} is the kronecker delta ($\delta_{0n} = 1$ if $n = 0$, otherwise $\delta_{0n} = 0$).

Multiply [2.46] by $\cos(q_n z)$ and integrate by parts from $z = 0$ to $z = d$:

$$\int_0^d E_{\pm}''(z) \cos(q_n z) dz + \frac{2i\mu_{\pm}}{\sigma_0 \delta_0^2} \int_0^d j_{\pm}(z) \cos(q_n z) dz = 0$$



$$\frac{2 - \delta_{0n}}{d} [E_{\pm}'(d)(-1)^n - E_{\pm}'(0)] - q_n^2 E_{\pm}^n + \frac{2i\mu_{\pm}}{\sigma_0 \delta_0^2} j_{\pm}^n = 0 \quad [6.8]$$

But the boundary conditions [2.48] demand $E_{\pm}'(0) = \pm \omega \mu_{\pm} / c$ and $E_{\pm}'(d) = 0$ so [6.8] becomes

$$q_n^2 E_{\pm}^n - \frac{2i\mu_{\pm}}{\sigma_0 \delta_0^2} j_{\pm}^n = \mp \frac{\omega \mu_{\pm}}{c} \left[\frac{2 - \delta_{0n}}{d} \right] \quad [6.9]$$

The fourier coefficients j_{\pm}^n are obtained in a rather

devious way. First, we substitute [6.3] into [6.2] to get:

$$\begin{aligned}
 j_{\pm}(z) &= \sum_{n=0}^{\infty} \int_{-\infty}^{\infty} K_{\pm}^{\infty}(1z-s1) E_{\pm}^n \cos(q_n \xi) d\xi \\
 &= \sum_{n=0}^{\infty} \frac{1}{2} \int_{-\infty}^{\infty} K_{\pm}^{\infty}(1z-s1) E_{\pm}^n \left[e^{iq_n \xi} + e^{-iq_n \xi} \right] d\xi
 \end{aligned}$$

then we re-arrange the integral over ξ using

$$\begin{aligned}
 \int_{-\infty}^{\infty} K_{\pm}^{\infty}(1z-s1) e^{iq_n \xi} d\xi &= \int_{-\infty}^{\infty} K_{\pm}^{\infty}(1z-s1) e^{iq_n(\xi-z)} e^{iq_n z} d\xi \\
 &= \left[\int_{-\infty}^{\infty} K_{\pm}^{\infty}(1u) e^{iq_n u} du \right] e^{iq_n z}
 \end{aligned}$$

and

$$\int_{-\infty}^{\infty} K_{\pm}^{\infty}(1z-s1) e^{-iq_n \xi} d\xi = \left[\int_{-\infty}^{\infty} K_{\pm}^{\infty}(1u) e^{iq_n u} du \right] e^{-iq_n z}$$

Hence,

$$j_{\pm}(z) = \sum_{n=0}^{\infty} \left[\int_{-\infty}^{\infty} K_{\pm}^{\infty}(1u) e^{iq_n u} du \right] E_{\pm}^n \cos(q_n z) \quad [6.10]$$

and we identify the fourier coefficients j_{\pm}^n as

$$j_{\pm}^n = \sigma_{\pm}(q_n, \omega) E_{\pm}^n \quad [6.11]$$

where $\sigma_{\pm}(q, \omega)$ is the frequency and wavenumber dependent conductivity tensor defined by

$$\sigma_{\pm}(q, \omega) = \int_{-\infty}^{\infty} K_{\pm}^{\infty}(|z|) \exp(iqz) dz \quad [3.44]$$

The integral [6.12] was evaluated in section 3.4 (pp. 74-75) for the infinite medium current kernels $K_{\pm}^{\infty}(|z-\xi|)$ appropriate for a metal with a spherical Fermi surface. The result was

$$\sigma_{\pm}(q, \omega) = \frac{3}{4} \frac{\sigma_0}{LAX} k\left(\frac{iql}{LAX}\right) \quad [3.49]$$

where

$$LAX = [1 - i(\omega \pm \omega_c)\tau]$$

and

$$k(y) = \frac{1}{y^3} \left[2y - (1-y^2) \ln\left(\frac{1+y}{1-y}\right) \right] \quad [3.50]$$

(we assume $\ln(t) = \ln|t| + \text{Arg}(t)$; $-\pi < \text{Arg}(t) \leq \pi$).

Hence,

$$j_{\pm}^n = \frac{3}{4} \frac{\sigma_0}{LAX} k(y_{\pm}^n) \cdot E_{\pm}^n \quad [6.13]$$

where,
$$y_n^\pm = \frac{iq_n l}{LAX} = \frac{in\pi l}{LAX \cdot d} \quad [6.14]$$

and substituting [6.11] into [6.9] gives

$$E_\pm^n = \mp \frac{\omega \mu_\pm}{c \cdot d} \frac{2 - \delta_{0n}}{q_n^2 - \frac{3}{2} \frac{i\mu_\pm}{LAX \cdot \delta_0^2} k(y_n^\pm)} \quad [6.15]$$

Finally then, the electric fields $G_\pm(z)$ that satisfy the boundary value problem [2.46] - [2.48] are

$$G_\pm(z) = \mp \frac{\omega \mu_\pm}{c} \frac{1}{d} \sum_{n=0}^{\infty} \frac{(2 - \delta_{0n}) \cos(q_n z)}{q_n^2 - \frac{3}{2} \frac{i\mu_\pm}{LAX \cdot \delta_0^2} k(y_n^\pm)} \quad [6.16]$$

The transmission coefficients T_\pm and the surface impedances z_\pm^S are given by [2.75] and [2.79],

$$T_\pm \approx \pm 2iG_\pm(d) \quad [2.75]$$

$$z_\pm^S = G_\pm(0) \quad [2.79]$$

Thus, for specular surface scattering,

$$T_\pm = - \frac{2i\omega \mu_\pm}{c} \frac{1}{d} \sum_{n=0}^{\infty} \frac{(2 - \delta_{0n}) \cdot (-1)^n}{q_n^2 - \frac{3}{2} \frac{i\mu_\pm}{LAX \cdot \delta_0^2} k(y_n^\pm)} \quad [6.17]$$

$$Z_{\pm}^S = \mp \frac{\omega \mu_{\pm}}{c} \frac{1}{d} \sum_{n=0}^{\infty} \frac{(2 - \delta_{0n})}{q_n^2 - \frac{3}{2} \frac{i \mu_{\pm}}{LAX \cdot \delta_0^2} k(y_n^{\pm})} \quad [6.18]$$

6.3 Evaluation of the Series Solutions

The series solutions for $G_{\pm}(z)$ are easier to work with if we express them directly in terms of the summation index n and pack-up as much of the series as we can into constants that are independent of n . A little manipulation of [6.16] yields:

$$G_{\pm}(z) = A_{\pm} \left[-\frac{3}{8\beta_{\pm}} + \sum_{n=1}^{\infty} \frac{\cos(q_n z)}{n^2 - \beta_{\pm} k(y_n^{\pm})} \right] \quad [6.19]$$

where

$$A_{\pm} = \mp \frac{2\omega \mu_{\pm}}{c} \left(\frac{d}{\pi z} \right) \quad [6.20]$$

$$\beta_{\pm} = \frac{3}{2} \frac{i \mu_{\pm}}{LAX} \left(\frac{d}{\pi \delta_0} \right)^2 \quad [6.21]$$

$$y_n^{\pm} = \frac{in\pi}{LAX} \left(\frac{l}{d} \right) \quad [6.22]$$

$$LAX = 1 - i(\omega \pm \omega_c) \tau \quad [6.23]$$

and we have separated the $n = 0$ term from the infinite sum and simplified it using the fact $k(0) = 4/3$ (see section 3.4.1 on page 75).

The series solution [6.19] converges very slowly. For example, when we tried to evaluate $G_-(d)$ at FMR for $d = 5 \mu\text{m}$, $l = 1 \mu\text{m}$, and the Nickel parameters of appendix A, we had to sum over 80,000 terms to obtain an answer stable to just three digits! Obviously, this makes the series solutions unsuitable for calculating the electric fields in the slab: not only would the amount of computer time be prohibitive but the chance of round-off and/or truncation error spoiling the results becomes a very big problem when one must sum a great many terms.

Fortunately, we can convert the infinite series representation for $G_{\pm}(z)$ into a form suitable for numerical evaluation by means of a simple trick.

Consider what happens to the denominator of the infinite sum in [6.19] as the summation index n is increased. Since y_n is directly proportional to n , increasing n increases y_n . Eventually, we will reach a point where $y_n \gg 1$ and, using the results of section 3.4 (p.75), $k(y_n)$ will reduce to $i\pi/y_n$. In that case, the numerator of the summand in [6.19] becomes

$$n^2 - \beta k(y_n) \approx n^2 - \frac{3}{2} \frac{i\mu}{\pi^2} \left(\frac{d^3}{\epsilon_0^2 l} \right) \frac{1}{n} \quad [6.24]$$

Hence, if we let n get large enough, the denominator will eventually reduce to n^2 . If we assume that this happens when $n = p$, where p is some large integer that satisfies the condition,

$$p^2 \gg |\beta k(y_p)| = \left| \frac{3}{2} \frac{i\mu}{\pi^2} \left(\frac{d^3}{s_0^2 l} \right) \frac{1}{p} \right| \quad [6.25]$$

we can write the infinite series in [6.19] as

$$\sum_{n=1}^{\infty} \frac{\cos(q_n z)}{n^2 - \beta k(y_n)} \approx \sum_{n=1}^p \frac{\cos(q_n z)}{n^2 - \beta k(y_n)} + \sum_{n=p+1}^{\infty} \frac{\cos(q_n z)}{n^2} \quad [6.26]$$

But the second sum on the RHS of [6.26] is just the known series⁴³

$$\sum_{n=1}^{\infty} \frac{\cos(nx)}{n^2} = \frac{1}{2} \left[\frac{\pi^2}{3} - \pi x + \frac{1}{2} x^2 \right]; \quad 0 \leq x \leq 2\pi \quad [6.27]$$

So, with $x = \pi(z/d)$ (ie, $nx = q_n z$), we can write

$$\begin{aligned} \sum_{n=p+1}^{\infty} \frac{\cos(q_n z)}{n^2} &= \sum_{n=1}^{\infty} \frac{\cos(q_n z)}{n^2} - \sum_{n=1}^p \frac{\cos(q_n z)}{n^2} \\ &= -\frac{\pi^2}{2} \left[\left(\frac{z}{d} \right) - \frac{1}{2} \left(\frac{z}{d} \right)^2 - \frac{1}{3} \right] - \sum_{n=1}^p \frac{\cos(q_n z)}{n^2} \end{aligned} \quad [6.28]$$

Substituting this result in [6.26] yields

$$\begin{aligned} \sum_{n=1}^{\infty} \frac{\cos(q_n z)}{n^2 - \beta k(y_n)} &\approx \sum_{n=1}^P \left[\frac{1}{n^2 - \beta k(y_n)} - \frac{1}{n^2} \right] \cos(q_n z) \\ &\quad - \frac{\pi^2}{2} \left[\left(\frac{z}{d}\right) - \frac{1}{2} \left(\frac{z}{d}\right)^2 - \frac{1}{3} \right] \\ &= \sum_{n=1}^P \left[\frac{\beta k(y_n)}{n^2 (n^2 - \beta k(y_n))} \right] \cos(q_n z) - \frac{\pi^2}{2} \left[\left(\frac{z}{d}\right) - \frac{1}{2} \left(\frac{z}{d}\right)^2 - \frac{1}{3} \right] \end{aligned} \quad [6.29]$$

and the solutions for $G_{\pm}(z)$ take on the form

$$\begin{aligned} G_{\pm}(z) &= -A_{\pm} \left\{ \frac{3}{8\beta_{\pm}} + \frac{\pi^2}{2} \left[\left(\frac{z}{d}\right) - \frac{1}{2} \left(\frac{z}{d}\right)^2 - \frac{1}{3} \right] \right\} \\ &\quad + A_{\pm} \sum_{n=1}^P \left[\frac{\beta_{\pm} k(y_n^{\pm})}{n^2 (n^2 - \beta_{\pm} k(y_n^{\pm}))} \right] \cos(q_n z) \end{aligned} \quad [6.30]$$

6.3.1 An Estimation of the Sum Limit p

It is a relatively simple matter to obtain a value for the sum limit p, defined by [6.25] as

$$p^2 \gg \left| \frac{3}{2} \frac{i\mu}{\pi^2} \left(\frac{d^3}{s_0^2 l} \right) \frac{1}{P} \right|$$

(\pm subscripts suppressed). We write the expression for p as

$$p^2 = 10^m \cdot \frac{3}{2} \frac{|\mu|}{\pi^2} \left(\frac{d^3}{s_0^2 l} \right) \frac{1}{P} \quad [6.31]$$

where m is an integer equal to 2 or more. Solving for p yields

$$p = 10^{m/3} \left[\frac{3}{2} \frac{|\mu|}{\pi^2} \right]^{1/3} \frac{d}{(\delta_0^2 l)^{1/3}} \quad [6.32]$$

which shows that the number of terms we will have to add together to obtain a good estimate of the sum depends on the permeability through $|\mu_{\pm}|^{1/3}$ and on the slab thickness d .

However, the estimate of p DOES NOT depend on the rf skin depth δ_0 or conduction mean free path l because the product $(\delta_0^2 l)$ is a constant in a metal as long as the microwave frequency ω is fixed:

$$\delta_0^2 l = \left(\frac{c^2}{2\pi\omega\sigma_0} \right) l = \frac{c^2}{2\pi\omega} \left(\frac{l}{\sigma_0} \right)$$

and

$$\frac{\sigma_0}{l} = \frac{n e^2}{m^* v_F}$$

Let's evaluate p for the case of Nickel at 24 GHz. Using the parameters of Appendix A we find $(\delta_0^2 l) \approx 4.2 \times 10^{-3} \mu\text{m}^3$. Taking the slab thickness to be $d = 5 \mu\text{m}$ and $\mu = \mu_-(\text{FMR}) = 32i$ (the maximum value that μ_{\pm} will take on), we get

$$p = (52.8) \cdot 10^{m/3} \quad [6.33]$$

Being very conservative, and taking $m = 4$, we find $p = 1138$.

Using [6.30] with $p = 1138$, we evaluated $G_-(d)$ at FMR for $d = 5 \mu\text{m}$, $l = 1 \mu\text{m}$, and for the Nickel parameters of appendix A. The answer we obtained was stable to over 4 decimal places (ie, summing more terms in the series did not change the answer in the fourth place).

The new series [6.30] is a big improvement over the original series [6.19]. Remember, to evaluate $G_-(d)$ to only 3 places using [6.19] we had to sum over 80,000 terms.

6.3.2 A More Formal Way of Evaluating the Series

It is interesting to note that we can arrive at nearly the same expression for $G_{\pm}(z)$ that we developed in the last section by another, more formal, route.

When confronted with a slowly converging series, one can increase the convergence by means of the "comparison method", a standard technique from numerical analysis that's analagous to evaluating a singular integral by subtracting off the singular part and treating it separately⁴⁴.

The comparison method involves introducing a known series with the same rate of convergence as the series one wishes to accelerate. For our case we have, by [6.19], a slowly converging series of the form

$$\sum_{n=1}^{\infty} \frac{\cos(g_n z)}{n^2 - \beta k(y_n)}$$

[6.34]

which looks very much like the known series

$$\sum_{n=1}^{\infty} \frac{\cos(q_n z)}{n^2} \quad [6.35]$$

To increase the convergence of [6.34] we therefore add and subtract [6.35] from [6.34] to get:

$$\sum_{n=1}^{\infty} \frac{\cos(q_n z)}{n^2 - \beta k(y_n)} = \sum_{n=1}^{\infty} \frac{\cos(q_n z)}{n^2} + \sum_{n=1}^{\infty} \frac{\beta k(y_n) \cos(q_n z)}{n^2 (n^2 - \beta k(y_n))} \quad [6.36]$$

The known series [6.35] is just

$$\sum_{n=1}^{\infty} \frac{\cos(q_n z)}{n^2} = -\frac{\pi^2}{2} \left[\left(\frac{z}{d}\right) - \frac{1}{2} \left(\frac{z}{d}\right)^2 - \frac{1}{3} \right]; \quad 0 \leq \frac{z}{d} \leq 1 \quad [6.27]$$

so that the accelerated form of $G_{\pm}(z)$ becomes

$$G_{\pm}(z) = -A_{\pm} \left\{ \frac{3}{8\beta_{\pm}} + \frac{\pi^2}{2} \left[\left(\frac{z}{d}\right) - \frac{1}{2} \left(\frac{z}{d}\right)^2 - \frac{1}{3} \right] \right\} + A_{\pm} \sum_{n=1}^{\infty} \left[\frac{\beta_{\pm} k(y_n^{\pm})}{n^2 (n^2 - \beta_{\pm} k(y_n^{\pm}))} \right] \cos(q_n z) \quad [6.37]$$

which is exactly the same as the approximate form [6.30] we developed in section 6.3 except that the sum limit p has been

replaced by ∞ .

Therefore, what we did in sections 6.3-6.3.1 was to accelerate the convergence of the original series solution [6.19] using the comparison method and put an upper bound p on the number of terms needed to obtain a good estimate of $G_{\pm}(z)$.

6.4 Integral Form for the Transmission Coefficient

If we only want to calculate the transmission coefficients $T_{\pm} \approx \pm 2iG_{\pm}(d)$, we can dispense with the series solution for $G_{\pm}(d)$ altogether and use the techniques of complex variable to re-cast the original series solution [6.17] for T_{\pm} into an integral form which can be easily, and accurately, evaluated on a computer. The integral form is valid for any δ/l ratio and slab thickness d and is much faster to calculate than the series solutions. The integral form was suggested by the method used by Kogan, Turov, and Ustinov¹⁵ to derive an analytic expression for $G_{\pm}(d)$ in the thick slab limit ($d/\delta \gg 1$, $d/l \gg 1$).

One begins the conversion by writing the original series solution [6.17] for T_{\pm} in terms of the variable y_{\pm}^n defined by [6.14]; ie,

$$T_{\pm} = -\frac{2i\omega\mu_{\pm}}{c \cdot d} \sum_{n=0}^{\infty} \frac{(2 - \delta_{0n}) \cdot (-1)^n}{q_n^2 - \frac{3}{2} \frac{i\mu_{\pm}}{L \times \delta_0^2} \cdot k(y_{\pm}^n)} \quad [6.17]$$

is re-written as

$$T_{\pm} = -\frac{2i\omega\mu}{c} \frac{1}{d} \frac{l^2}{LAX^2} \sum_{n=-\infty}^{\infty} \frac{(-1)^n}{y_n^2 + \alpha k(y_n)} \quad [6.38]$$

where

$$y_n = \frac{iq_n l}{LAX}$$

$$LAX = 1 - i(\omega \pm \omega_c)\tau$$

$$\alpha = \frac{3}{2} \frac{i\mu}{LAX^3} \left(\frac{l}{\delta_0}\right)^2 \quad [6.39]$$

(all \pm subscripts suppressed) Note that the sum over n in [6.38] has been adjusted to run from $n = -\infty$ to $n = \infty$. This is permissible because $k(y)$ is an even function of y . We have also redefined y_n from $iq_n l / LAX$ to $q_n l / (iLAX)$ so we don't have to carry an extra minus sign around later on (see p. 150). This change in y_n does not alter the form of the sum.

Now, suppose now that we had some complex valued function $f(y)$ with infinitely many simple poles at the y_n required for the evaluation of the sum in [6.38]. If we chose a suitable contour that enclosed all these simple poles, and required that the residue of $f(y)$ at any of the points y_n be

$$\text{Res}[f(y_n)] = R_n = \frac{(-1)^n}{y_n^2 + \alpha k(y_n)} \quad [6.40]$$

then we could use Cauchy's Residue Theorem to write,

$$\begin{aligned} \frac{1}{2\pi i} \oint_C f(y) dy &= \sum_{n=-\infty}^{\infty} R_n + \sum \text{Res}[f(y)] \\ &= \sum_{n=-\infty}^{\infty} \frac{(-1)^n}{y_n^2 + \alpha k(y_n)} + \sum \text{Res}[f(y)] \end{aligned} \quad [6.41]$$

where the residue term on the RHS is due to any additional poles contained in $f(y)$.

A suitable choice for $f(y)$ is something like

$$f(y) = \frac{A}{\sin(By)(y^2 + \alpha k(y))} \quad [6.42]$$

where A and B are parameters to be determined. The function $f(y)$, as defined by [6.42], has simple poles at $By = n\pi$ and additional poles at the roots of $y^2 + \alpha k(y)$ (we discuss these roots later).

Assuming that the roots of $y^2 + \alpha k(y)$ do not coincide with any of the roots of $\sin(By)$, we can evaluate the residue R_n at $By = n\pi$ using:

$$R_n = \lim_{\sin(By) \rightarrow n\pi} \left[\frac{A}{y^2 + \alpha k(y)} \cdot \frac{(y - \frac{n\pi}{B})}{\sin(By)} \right] \quad [6.43]$$

L'Hospital's Rule gives

$$R_n = \frac{A}{\left(\frac{n\pi}{B}\right)^2 + \alpha k\left(\frac{n\pi}{B}\right)} \cdot \frac{1}{B \cos(n\pi)}$$

$$= \frac{(-1)^n}{B} \cdot \frac{A}{\left(\frac{n\pi}{B}\right)^2 + \alpha k\left(\frac{n\pi}{B}\right)} \quad [6.44]$$

and in order to make R_n equal to the n th term of the sum in [6.38] we define

$$\frac{n\pi}{B} = y_n \Rightarrow B = iLAX \cdot \left(\frac{d}{\ell}\right) \quad [6.45]$$

and

$$A = B \quad [6.46]$$

The function $f(y)$ is therefore:

$$f(y) = \frac{LAX \left(\frac{d}{\ell}\right)}{\sinh\left(LAX \cdot \frac{d}{\ell} y\right) (y^2 + \alpha k(y))} \quad [6.47]$$

(where we have used $\sin(ix) = i\sinh(x)$). The infinite sum required to evaluate T_{\pm} can thus be written as

$$\sum_{n=-\infty}^{\infty} \frac{(-1)^n}{y_n^2 + \alpha k(y_n)} = \frac{1}{2\pi i} \oint_c f(y) dy - \sum \text{Res}[f(y)] \quad [6.48]$$

where $\sum \text{Res}[f(y)]$ is the sum of residues associated with the roots of $y^2 + \alpha k(y)$.

6.4.1 Evaluation of The Contour Integral

In order to define a suitable integration contour, we must consider the location of all the simple poles at the points y_n , the roots of $y^2 + \alpha k(y)$, and the location of any branch points associated with $f(y)$. The simple poles at $y_n = n\pi l / (iL\alpha X d)$ will all lie along a straight line inclined at an angle $\theta = \text{Arctan}([\omega \pm \omega_c] \tau)$ to the imaginary axis. Any roots y_i of $y^2 + \alpha k(y)$ must occur in pairs $(y_i, -y_i)$ because $k(y)$ is an even function of y . Further, the roots y_i cannot lie along the real axis because a is, in general, complex. Finally, the function $f(y)$ has branch points at $y = -1$ and $y = 1$ owing to the presence of the complex logarithm term

$$\ln \left[\frac{1+y}{1-y} \right]$$

in $k(y)$. We shall assume $\ln(t) = \ln|t| + \text{Arg}(t)$, where $-\pi < \text{Arg}(t) \leq \pi$, so $\ln(t)$ will have a branch cut along the negative real axis (see figure 25). Using the bilinear transformation $t = (1+y)/(1-y)$ it's a simple matter to convince oneself that the single branch cut in the complex t plane

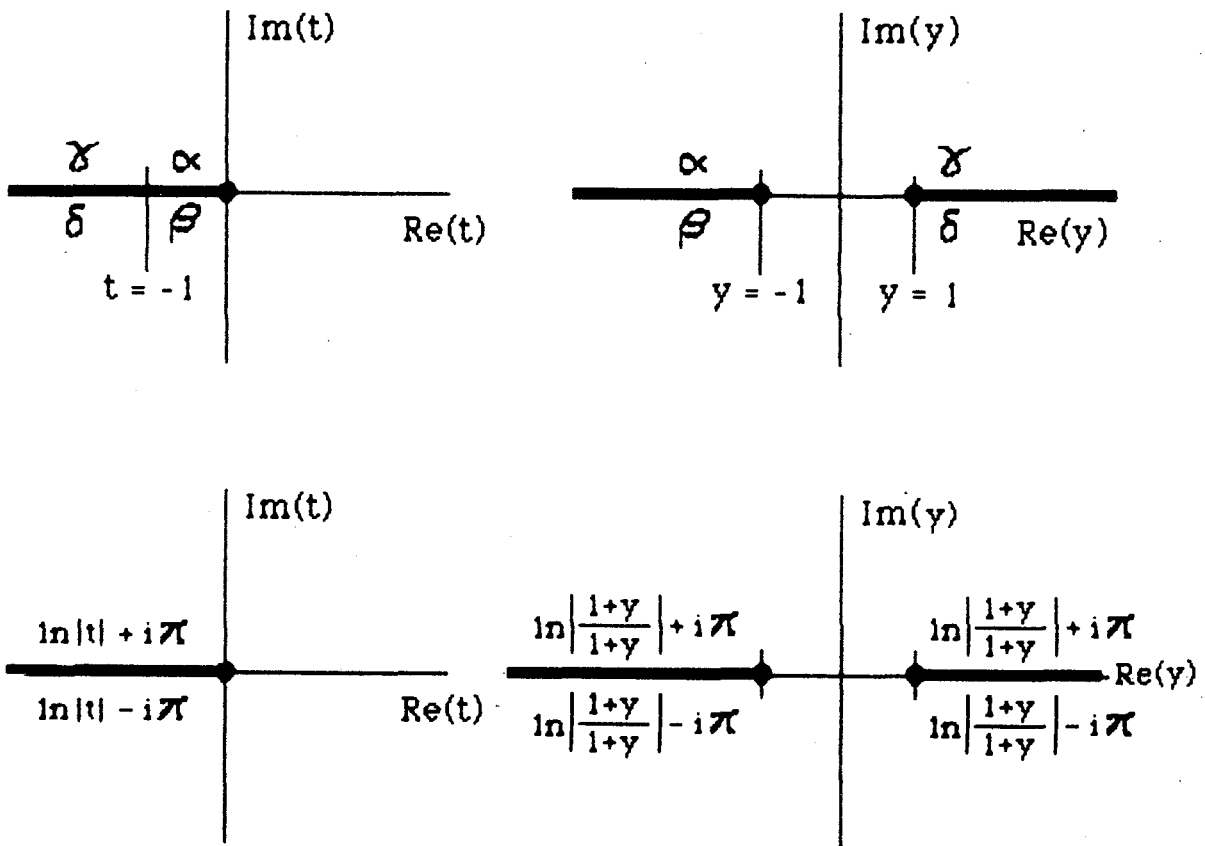


Fig. 25 If we define $\ln(t) = \ln|t| + \text{Arg}(t)$; $-\pi < \text{Arg}(t) \leq \pi$, then $\ln(t)$ has a branch cut along the negative real axis and $\ln((1+y)/(1-y))$ has two branch cuts: one along the line $(-\infty, -1]$, the other along the line $[1, \infty)$. The values that $\ln(t)$ and $\ln((1+y)/(1-y))$ take on along their respective branch cuts is shown above.

associated with $\ln(t)$ leads to two branch cuts in the complex y plane associated with $\ln((1+y)/(1-y))$. See figure 25.

Therefore, a suitable contour that avoids the branch cuts, but encloses all the simple poles at the y_n , and all the roots of $y^2+ak(y)$, is shown in figure 26.

From the form of $f(y)$ we can see that the contour integral goes to zero along the outer circular arcs of the contour and around the vanishingly small circles about the branch points $y = \pm 1$. Therefore,

$$\oint_C f(y)dy = \int_1^{\infty} f(y)dy + \int_{-\infty}^{-1} f(y)dy + \int_{-1}^{\infty} f(y)dy + \int_{\infty}^1 f(y)dy$$

(top of +ve cut)
(top of -ve cut)
(bottom of -ve cut)
(bottom of +ve cut)

and bearing in mind the limiting values that $\ln((1+y)/(1-y))$

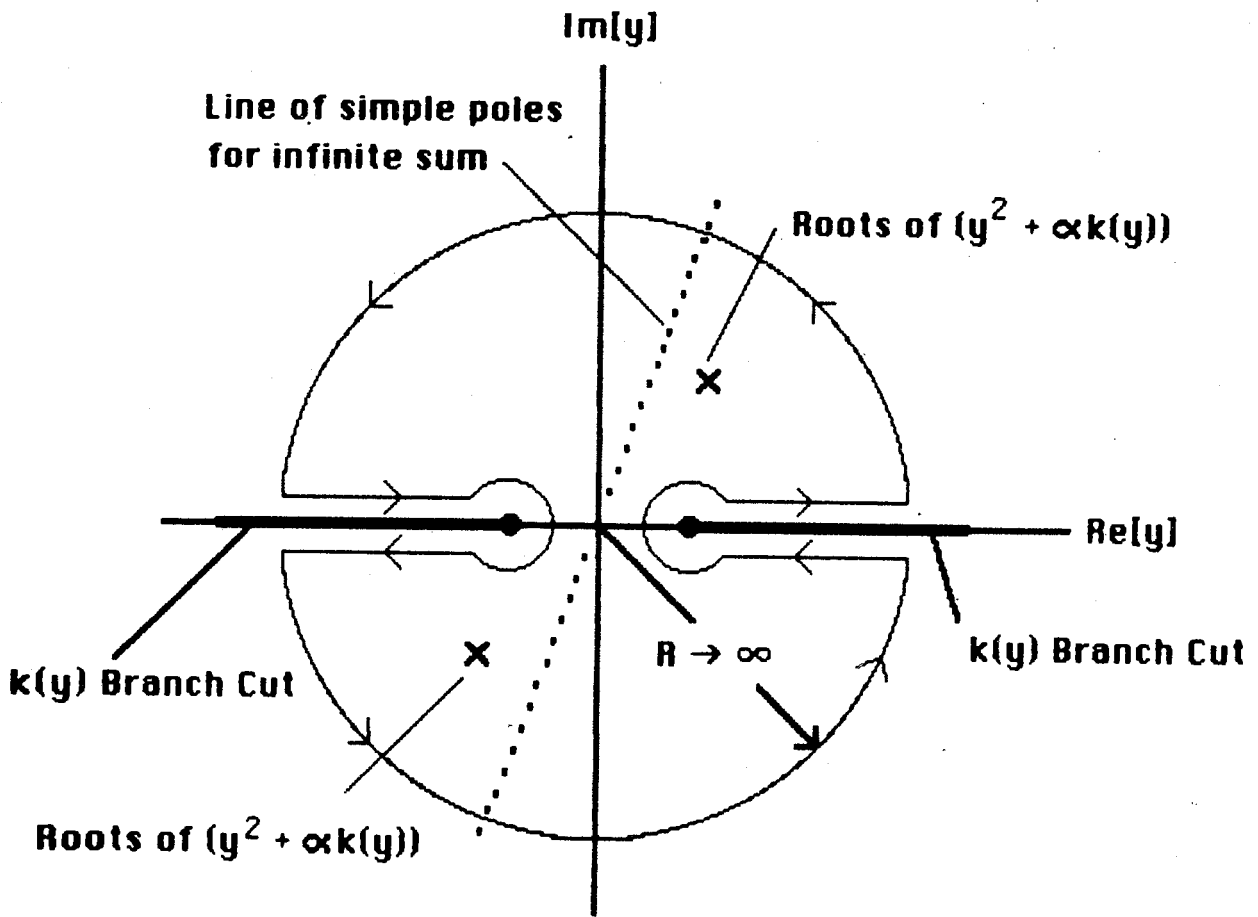


Fig. 26 The contour used to evaluate the contour integral associated with the transmission coefficients.

takes on along the branch cuts,

$$\begin{aligned}
 \oint_C f(y) dy &= LAX \cdot \left(\frac{d}{\ell}\right) \int_1^{\infty} \frac{dy}{\sinh(LAX \cdot \frac{d}{\ell} y) (y^2 + \alpha [t(y) - i\pi \frac{(1-y^2)}{y^3}])} \\
 &+ LAX \cdot \left(\frac{d}{\ell}\right) \int_{-\infty}^{-1} \frac{dy}{\sinh(LAX \cdot \frac{d}{\ell} y) (y^2 + \alpha [t(y) - i\pi \frac{(1-y^2)}{y^3}])} \\
 &+ LAX \cdot \left(\frac{d}{\ell}\right) \int_{-1}^{-\infty} \frac{dy}{\sinh(LAX \cdot \frac{d}{\ell} y) (y^2 + \alpha [t(y) + i\pi \frac{(1-y^2)}{y^3}])} \\
 &+ LAX \cdot \left(\frac{d}{\ell}\right) \int_{\infty}^1 \frac{dy}{\sinh(LAX \cdot \frac{d}{\ell} y) (y^2 + \alpha [t(y) + i\pi \frac{(1-y^2)}{y^3}])}
 \end{aligned}$$

... [6.49]

where y is now real and $k(y)$ is redefined as the real function $t(y)$:

$$t(y) = \frac{1}{y^3} \left[2y - (1-y^2) \ln \left| \frac{1+y}{1-y} \right| \right] \tag{6.50}$$

If we adjust all integrals in [6.49] to run from $y = 1$ to $y = \infty$

we find,

$$\oint_{\mathcal{C}} f(y) dy = 2 \cdot LAX \cdot \left(\frac{d}{\ell}\right) \int_1^{\infty} \frac{y^3 dy}{\sinh(LAX \frac{d}{\ell} y)} \cdot \left[\frac{1}{y^3(y^2 + \alpha \tau(y)) - i\pi(1-y^2)\alpha} - \frac{1}{y^3(y^2 + \alpha \tau(y)) + i\pi\alpha(1-y^2)} \right] \quad [6.51]$$

or, combining the terms in the square brackets and simplifying,

$$\oint_{\mathcal{C}} f(y) dy = 4\pi i \cdot LAX \cdot \left(\frac{d}{\ell}\right) \alpha \int_1^{\infty} \Theta(y) \operatorname{csch}(LAX \frac{d}{\ell} y) dy \quad [6.52]$$

where we have defined $\Theta(y)$ as

$$\Theta(y) = \frac{y^3(1-y^2)}{[y^5 + \alpha y^3 \tau(y)]^2 + \pi^2 (y^2-1)^2 \alpha^2} \quad [6.53]$$

6.4.2 Residue Evaluation

The roots of $y^2 + ak(y)$ contribute a sum of residues $\Sigma \operatorname{Res}[f(y)]$ to the infinite sum [6.48]. Using the argument principle⁴⁵, Reuter and Sondheimer¹⁰, and later Baraff²⁴, were able to establish that the even function $y^2 + ak(y)$ had at most four roots occurring in the two pairs $y_1, -y_1$ and $y_2, -y_2$. When $|a|$ is below some limiting value there will be one pair of roots, when $|a|$ is above the limiting value there will be two pairs of roots (the precise value of $|a|$ at the change over is

unimportant -- the algorithm we have developed to extract the roots can distinguish between the two cases).

The residue of $f(y)$ associated with the root y_1 is just

$$\begin{aligned} \text{Res}[f(y_1)] &= \lim_{y \rightarrow y_1} \left[\frac{y - y_1}{y^2 + \alpha k(y)} \cdot \frac{LAX \cdot \left(\frac{d}{l}\right)}{\sinh\left(LAX \frac{d}{l} y\right)} \right] \\ &= LAX \cdot \frac{d}{l} \frac{1}{\sinh\left(LAX \frac{d}{l} y_1\right) [2y_1 + \alpha k'(y_1)]} \end{aligned} \quad [6.54]$$

where

$$\frac{dk(y)}{dy} = k'(y) = -\frac{3}{y} k(y) + \frac{2}{y^2} \ln \left[\frac{1+y}{1-y} \right] \quad [6.55]$$

The residues associated with $-y_1$ is found by replacing y_1 in [6.54] with $-y_1$. We find, $\text{Res}(f(y_1)) = \text{Res}(f(-y_1))$ so that the residues associated with the root pair $(y_1, -y_1)$ are given by

$$\text{Res}[f(y_1)] + \text{Res}[f(-y_1)] = \frac{2 \cdot LAX \cdot \left(\frac{d}{l}\right)}{\sinh\left(LAX \frac{d}{l} y_1\right) [2y_1 + \alpha k'(y_1)]} \quad [6.56]$$

Similarly, the residues associated with the root pair $(y_2, -y_2)$

are

$$\text{Res}[f(yz)] + \text{Res}[f(-yz)] = \frac{2 \cdot LAX \cdot \left(\frac{d}{\ell}\right)}{\sinh\left(LAX \frac{d}{\ell} yz\right) [2yz + \alpha k'(yz)]} \quad [6.57]$$

Hence,

$$\sum \text{Res}[f(y)] = \sum_i \frac{2 \cdot LAX \cdot \left(\frac{d}{\ell}\right)}{\sinh\left(LAX \frac{d}{\ell} y_i\right) [2y_i + \alpha k'(y_i)]} \quad [6.58]$$

where i runs from 1 to 2, depending on the number of root pairs we extract from $y^2 + \alpha k(y)$

6.4.3 The Net Integral Solution

Referring to equation [6.48] we see that the infinite sum needed to evaluate T_{\pm} is given by

$$\sum_{n=-\infty}^{\infty} \frac{(-1)^n}{y_n^2 + \alpha k(y_n)} = \frac{1}{2\pi i} \oint_c f(y) dy - \sum \text{Res}[f(y)]$$

Using equation [6.52] for the contour integral, and equation

[6.58] for the sum of residues, we get

$$\sum_{n=-\infty}^{\infty} \frac{(-1)^n}{y_n^2 + \alpha k(y_n)} = 2 \cdot LAX \cdot \left(\frac{d}{l}\right) \left[\alpha \int_1^{\infty} \Theta(y) \operatorname{csch}\left(LAX \frac{d}{l} y\right) dy \right. \\ \left. - \sum_i \frac{\operatorname{csch}\left(LAX \frac{d}{l} y_i\right)}{2y_i + \alpha k'(y_i)} \right] \quad [6.59]$$

so that, by equation [6.38], the transmission coefficients T_{\pm} are given by

$$T_{\pm} = \frac{4i\omega\mu_{\pm}}{c} \cdot \frac{l}{LAX} \left[\alpha_{\pm} \int_1^{\infty} \Theta(y) \operatorname{csch}\left(LAX \frac{d}{l} y\right) dy \right. \\ \left. - \sum_i \frac{\operatorname{csch}\left(LAX \frac{d}{l} y_i\right)}{2y_i + \alpha_{\pm} k'(y_i)} \right] \quad [6.60]$$

6.5 Implementation of The Integral Solution

In order to evaluate T_{\pm} using the integral form [6.60] we must numerically evaluate the integral from 1 to ∞ and extract the roots of $y^2 + \alpha k(y)$.

6.5.1 Numerical Evaluation of the Integral

A fast and accurate way of evaluating the integral in [6.60] is to use Gauss-Laguerre quadrature⁴⁴ (see Appendix F) which approximates real integrals over a semi-infinite interval using a finite sum:

$$\int_0^{\infty} e^{-x} F(x) dx \approx \sum_{i=1}^n A_i F(x_i) \quad [6.61]$$

(x and F(x) are real valued and the x_i are a set of unequally spaced points along the x axis). The integral in [6.60] is cast in a form similar to [6.61] as follows:

First, change variable from y to v using y = v + 1,

$$\int_1^{\infty} \mathbb{H}(y) \operatorname{csch}\left(LAX \frac{d}{l} y\right) dy = \int_0^{\infty} \mathbb{H}(1+v) \operatorname{csch}\left(LAX \frac{d}{l} [1+v]\right) dv$$

then re-write the csch term as

$$\operatorname{csch}\left(LAX \frac{d}{l} [1+v]\right) = \frac{2 e^{-LAX \frac{d}{l} v}}{1 - e^{-2 \cdot LAX \cdot \frac{d}{l} (1+v)}} e^{-LAX \cdot \frac{d}{l}}$$

Next, let (d/l)y = x and LAX = [1-i(ω±ω_c)τ] to get

$$P(x) = \mathbb{H}\left(\frac{l}{d} x + 1\right) \frac{e^{i(\omega \pm \omega_c) \tau \cdot x}}{1 - e^{-2LAX(x + d/l)}}$$

which allows us to write

$$\int_0^{\infty} \Theta(1+v) \operatorname{csch}\left(L\lambda x \frac{d}{d} [1+v]\right) dv = 2 \frac{d}{d} e^{-L\lambda x \frac{d}{d}} \left[\int_0^{\infty} P(x) e^{-x} dx \right] \quad [6.62]$$

and the integral on the RHS of [6.62] can be evaluated by splitting $P(x)$ into real and imaginary parts:

$$\int_0^{\infty} P(x) e^{-x} dx = \int_0^{\infty} \operatorname{Re}[P(x)] e^{-x} dx + i \int_0^{\infty} \operatorname{Im}[P(x)] e^{-x} dx$$

and applying Gauss-Laguerre quadrature⁴⁴ to the resulting pair of real valued integrals: Note that Gauss-Laguerre quadrature is not the only method available for evaluating our integrals. We chose this quadrature method because it is both fast and accurate. Often, the contour integral could be evaluated to more than 8 significant digits using a 32 point quadrature; ie, we could get an accurate answer knowing the value of the integrand at just 32 unequally spaced points along the semi-infinite interval $[0, \infty)$.

6.5.2 Numerical Extraction of the Roots of $y^2 + ak(y)$

The roots of $y^2 + ak(y)$ can be easily extracted in the NSE and extreme ASE regimes.

In the NSE regime, where l is small, $y = ql/(iLAX)$ is small and $k(y) \approx 4/3$ (see section 3.4). Thus,

$$y^2 + ak(y) \approx y^2 + (4/3)a = 0 \quad [6.63]$$

and the NSE roots are given by

$$y_1 = i\sqrt{(4/3)a}; \quad (\text{NSE}) \quad [6.64]$$

(in the NSE regime there are no second pair of roots $(y_2, -y_2)$).

In the extreme ASE regime, l is large, $y = ql/(iLAX)$ is large, and $k(y) \approx i\pi/y$ (see section 3.4). Thus,

$$y^2 + ak(y) \approx y^2 + i\pi a/y = 0 \quad [6.65]$$

so,

$$y_1^3 = -i\pi a; \quad (\text{extreme ASE}) \quad [6.66]$$

(Note that only one or two of the three possible ASE roots actually satisfy [6.65] -- see Baraff²⁴).

For intermediate values of δ/l we can estimate y_1 using the interpolation formula due to Southgate^{15, 46} that correctly reproduces the NSE roots and the extreme ASE roots and approximates y_1 in the intermediate δ/l regime. In terms of our

notation, the interpolation formula is:

$$y_1 \approx \frac{i \sqrt{\frac{4}{3} \alpha}}{\left[1 + \frac{4}{3\pi} \sqrt{\frac{4}{3} \alpha} \right]^{1/3}} \quad [6.67]$$

Noting that $a \ll 1$ in the NSE regime, and $a \gg 1$ in the extreme ASE regime, shows that [6.67] reduces to [6.64] and [6.66] in the appropriate regimes.

After an extensive, empirical study[†] of the number and location of the roots pairs $(y_1, -y_1)$, $(y_2, -y_2)$ for arbitrary values of a we have developed an algorithm that correctly extracts y_1 and y_2 for any value of a .

Basically, we use the Southgate formula [6.67] to get an approximate value of y_1 . A better value for y_1 is found by applying Newton's root extraction method to $y^2 + ak(y)$ with the y_1 guess as the starting value. For a complex valued function, Newton's method becomes

$$y_1^{(new)} = y_1 - \frac{y_1^2 + \alpha k(y_1)}{2y_1 + \alpha k'(y_1)} \cdot \frac{1}{\text{Re}[y_1]}$$

where the additional factor of $1/\text{Re}[y_1]$ is needed to insure stability of the algorithm when y is complex. Once y_1 is found, a good starting value for y_2 , when it existed, was found to be

[†]The study consisted of plotting three dimensional surface diagrams of $|1/(y^2 + ak(y))|$ vs $\text{Re}(y)$ and $\text{Im}(y)$ for various values of a . The roots showed up as sharp spikes on the 3-d surfaces.

given by

$$y_2^{(\text{guess})} = 2\bar{y}_1$$

(where \bar{y}_1 denotes the complex conjugate of y_1). The starting value for y_2 was then used in Newton's formula and iterated until it either resulted in a stable for y_2 (if y_2 existed) or the value of $-y_1$ (if y_2 did not exist).

6.6 Closed Forms for the Transmission Coefficients in the Thick Slab Limit ($d/l \gg 1$)

When $d/l \gg 1$ we can considerably simplify the integral expressions derived for T_{\pm} in section 6.4. The thick slab forms of T_{\pm} prove very useful for explaining the transmission behaviour as a function of δ/l and slab thickness d (see chapter 7).

From section 6.4.3 (p. 159) we had:

$$T_{\pm} = \frac{4i\omega\mu}{c} \frac{l}{LAX} \left[\alpha \int_0^{\infty} \Theta(y) \operatorname{csch}\left(LAX \frac{d}{l} y\right) dy - \sum_i \frac{\operatorname{csch}\left(LAX \frac{d}{l} y_i\right)}{2y_i + \alpha k'(y_i)} \right] \quad [6.60]$$

where the sum over i runs from $i=1$ to 1 or $i=1$ to 2 depending on

whether we extract 1 or 2 roots from $y^2 + ak(y)$ (see section 6.5.2 pp. 161-164).

If we assume a very thick slab ($d/l \gg 1$) then the csch terms reduce to

$$\operatorname{csch}\left(LAX \frac{d}{l} y\right) = \frac{2e^{-LAX \frac{d}{l} y}}{1 - e^{-2LAX \frac{d}{l} y}} \approx 2e^{-LAX \frac{d}{l} y}$$

so,

$$T_{\pm}\left(\frac{d}{l} \gg 1\right) \approx \frac{8i\omega\mu}{c} \frac{l}{LAX} \left[\alpha \int_1^{\infty} \Theta(y) e^{-LAX \frac{d}{l} y} dy - \sum_i \frac{e^{-LAX \frac{d}{l} y_i}}{2y_i + \alpha k'(y_i)} \right] \quad [6.68]$$

Consider the integral term in [6.68]. If we change variable from y to v using $y = 1 + v$ then the integral becomes

$$\alpha \int_1^{\infty} \Theta(y) e^{-LAX \frac{d}{l} y} dy = \alpha e^{-LAX \frac{d}{l}} \int_0^{\infty} \Psi(v) e^{-LAX \frac{d}{l} v} dv \quad [6.69]$$

where $\Psi(v) = \Theta(1+v)$.

In the $d/l \gg 1$ limit, the exponent $\exp(-LAX(d/l)v)$ rapidly goes to zero as v increases from zero. If we were doing the

integral numerically, we would find that most of the contribution to the integral would occur for small values of v . We can therefore approximate the integral when $d/l \gg 1$ by replacing $\Psi(v)$ with it's expansion for small v . From [6.53] we had

$$\textcircled{+} (1+v) = \Psi(v) = \frac{(1+v)^3 (1 - [1+v]^2)}{[(1+v)^5 + \alpha(1+v)^3 z(1+v)]^2 + \pi^2 \alpha^2 ([1+v]^2 - 1)^2}$$

where

$$z(y) = \frac{1}{y^3} \left[2y - (1-y^2) \ln \left| \frac{1+y}{1-y} \right| \right]$$

If we let $(1+v)^n \approx 1+nv$ and keep terms only to the lowest order in v , we get:

$$\begin{aligned} \Psi(v) &\approx \frac{(1+3v)(1-1-2v)}{[1+5v + \alpha(2+2v+2v \ln |\frac{2+v}{v}|)]^2 + \pi^2 (2v)^2 \alpha^2} \\ &\approx \frac{-2v}{[1+2\alpha + v(5+2\alpha + 2\alpha \ln |\frac{2+v}{v}|)]^2 + 4\pi^2 \alpha^2 v^2} \\ &\approx \frac{-2v}{(1+2\alpha)^2} \quad (\text{to lowest order in } v) \end{aligned}$$

and the integral [6.69] is given by

$$\begin{aligned} \int_0^{\infty} \Psi(v) e^{-L\alpha X \frac{d}{l} v} dv &\approx \int_0^{\infty} \frac{-2v e^{-L\alpha X \frac{d}{l} v}}{(1+2\alpha)^2} dv \\ &= -\frac{2}{(1+2\alpha)^2} \left(\frac{l}{L\alpha X}\right)^2 \frac{1}{d^2} \int_0^{\infty} x e^{-x} dx \\ &= -\frac{1}{2\alpha^2} \left(\frac{l}{L\alpha X \cdot d}\right)^2 \frac{1}{\left(1 + \frac{1}{2\alpha}\right)^2} \end{aligned}$$

Thus, when $d/l \gg 1$,

$$\begin{aligned} T_{\pm} \left(\frac{d}{l} \gg 1\right) &= \frac{8i\omega\mu}{c} \frac{l}{L\alpha X} \left[-\frac{1}{2\alpha} \frac{l^2}{L\alpha X^2 \cdot d^2} \frac{e^{-L\alpha X \frac{d}{l}}}{\left(1 + \frac{1}{2\alpha}\right)^2} \right. \\ &\quad \left. - \sum_i \frac{e^{-L\alpha X \frac{d}{l} y_i}}{2y_i + \alpha k'(y_i)} \right] \end{aligned}$$

or, using the definition [6.39] of α ,

$$\alpha = \frac{3}{2} \frac{i\omega}{L\alpha X^3} \left(\frac{l}{\delta_0}\right)^2$$

we can re-write $T_{\pm}(d/l \gg 1)$ in the simple form:

$$T_{\pm}\left(\frac{d}{l} \gg 1\right) = -\frac{8i\omega\mu_{\pm}}{c} \frac{l}{LAX} \sum_i \frac{e^{-LAX \frac{d}{l} y_i}}{2y_i + \alpha k'(y_i)}$$

$$-\frac{8}{3} \frac{\omega}{c} \frac{(\delta_0^2 l)}{d^2} \frac{e^{-LAX \frac{d}{l}}}{\left[1 - \frac{iLAX^3}{3\mu_{\pm}} \left(\frac{\delta_0}{l}\right)^2\right]}$$

[6.70]

7. RESULTS AND DISCUSSION

7.1 Introduction

The numerical procedures described in chapters 5 and 6 have been used to calculate the transmission of 24 GHz radiation through our model Nickel ferromagnet for the two cases of specular and diffuse surface scattering. The transmission coefficients T_{\pm} , the surface impedances z_{\pm}^S , and the electric field distributions $G_{\pm}(z)$ were calculated as functions of H_0 for a wide range of experimentally accessible slab thicknesses d and conduction mean free paths l (ie, $1 \leq d \leq 50 \mu\text{m}$ and $0.006 \leq l \leq 50 \mu\text{m}$).

Section 7.2 contains representative plots of T_{\pm} and z_{\pm}^S vs H_0 for $d = 2, 5, \text{ and } 10 \mu\text{m}$ and $0.006 \leq l \leq 25 \mu\text{m}$. The plots serve to demonstrate how T_{+} and T_{-} vary with H_0 , d , and l for specular and diffuse surface scattering.

In section 7.3 we discuss the variation of T_{\pm} with l using the forms of T_{\pm} calculated in section 6.6 for the case of specular surface scattering and a thick slab ($d/l \gg 1$).

In section 7.4 we again use the thick slab expressions for T_{\pm} to understand how the transmission scales with d and l in the ASE regime.

In section 7.5 the experimentally measurable, linearly polarized, transmission coefficient T is plotted as a function of H_0 for $d = 2, 5, \text{ and } 10 \mu\text{m}$ and $l \geq 1 \mu\text{m}$. When $\delta/l \leq 1$ (the ASE regime) T exhibits amplitude oscillations as a function of H_0 . We identify the oscillations as Gantmakher-Kaner oscillations⁴⁷ or GKO. The GKO are superimposed over transmission features associated with the metal's magnetic response but do not, in general, obscure the latter transmission features. Section 7.5 concludes with a short discussion on the feasibility of experimental verification of our calculated results.

7.2 Calculated Results

7.2.1 Variation of the Surface Impedance with H_0 and l

In figure 27 we plot $|z_{\pm}^S|$ vs H_0 for $d = 5 \mu\text{m}$ and $0.006 \leq l \leq 25 \mu\text{m}$.

We note three major features:

(i) Regardless of the value of l , the magnetically active surface impedance, z_{-}^S , goes through a minimum at FMAR and a maximum at FMR. The magnetically inactive surface impedance, z_{+}^S , exhibits a slow monotonic decrease with H_0 .

(ii) Both $|z_{-}^S|$ and $|z_{+}^S|$ vary with l only when $\delta/l > 1$. When $\delta/l \leq 1$ (the ASE regime), the surface impedances are virtually independent of the mean free path.

(iii) Neither $|z_{-}^S|$ nor $|z_{+}^S|$ depend strongly on the type of surface scattering. The curves calculated for specular and diffuse scattering are identical in the NSE regime and differ by a factor of 1.13 in the ASE regime.

The variation of z_{\pm}^S with H_0 and l has been investigated in detail by a number of authors^{9-10, 28, 48-50} for both specular and diffuse surface scattering in the the NSE regime ($\delta/l \gg 1$) and the extreme ASE regime ($\delta/l \ll 1$).

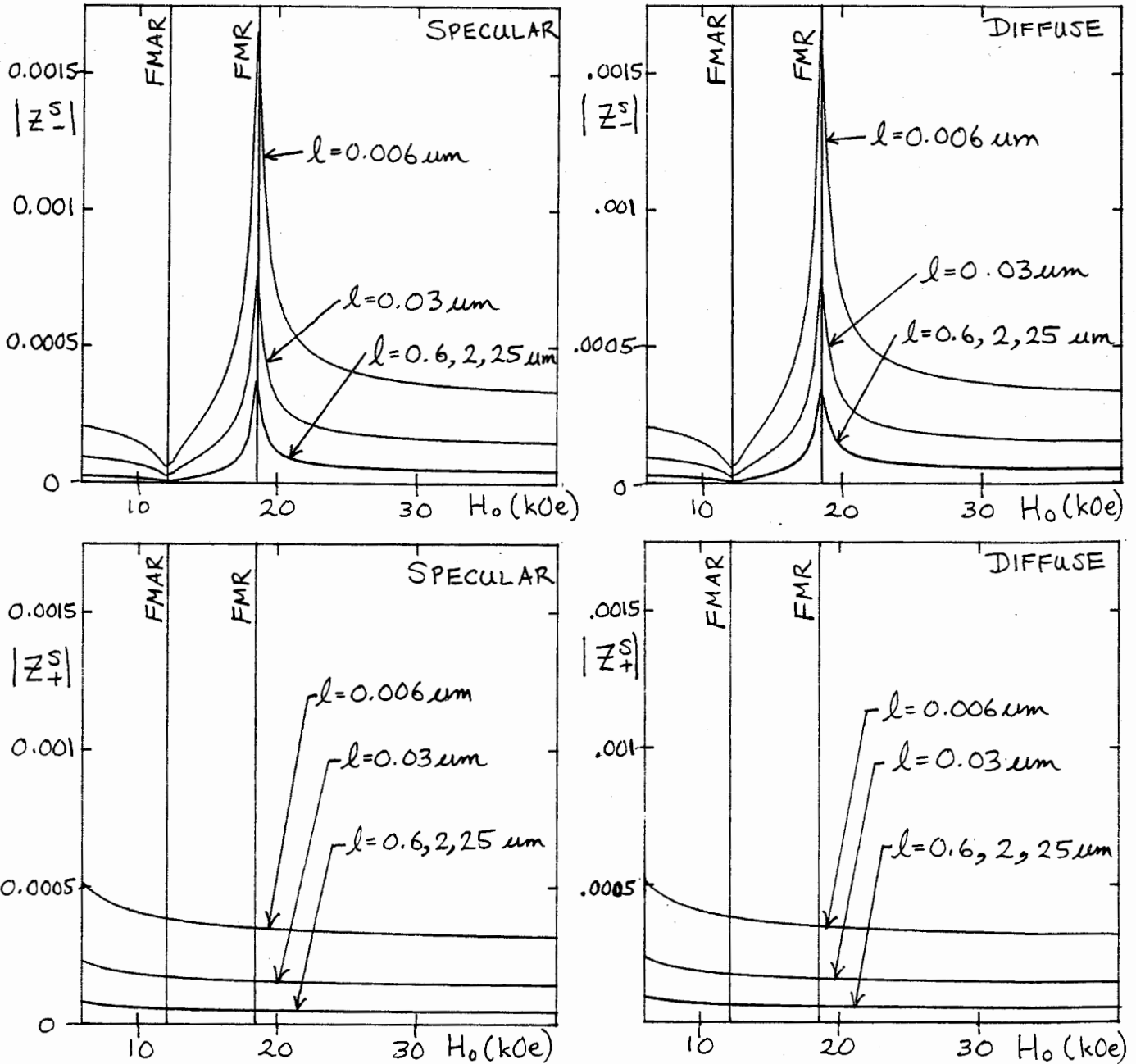


Fig. 27 Plots of $|z_{\pm}^S|$ vs H_0 for $d = 5 \mu\text{m}$ and for both specular and diffuse surface scattering. The calculations were carried out using the Nickel parameters of Appendix A. In Nickel, at 24 GHz, the cross over between the normal and anomalous skin effect regimes occurs when $l \approx 0.8 \mu\text{m}$.

In the NSE regime, the surface impedances in a thick slab ($d/\delta \gg 1$) can be written as

$$z_{\pm}^S \approx \mp \frac{i}{2} \frac{\omega}{c} \delta_0 \sqrt{-2i\mu_{\pm}} \quad [4.14]$$

(see chapter 4). In the extreme ASE regime, the surface impedances for the case of a thick slab and specular surface scattering are given by^{4,8}

$$Z_{\pm}^S(\delta/l \ll 1, \text{specular}) = \pm \frac{\omega}{c} \left(\frac{2}{3\pi}\right)^{1/3} (\delta_0^2 l)^{1/3} \left(1 + \frac{i}{\sqrt{3}}\right) \mu_{\pm}^{2/3} \quad [7.1]$$

while the corresponding surface impedances for diffuse surface scattering are given by^{9, 4,8}

$$Z_{\pm}^S\left(\frac{\delta}{l} \ll 1, \text{diffuse}\right) = \frac{9}{8} Z_{\pm}^S\left(\frac{\delta}{l} \ll 1, \text{specular}\right) \quad [7.2]$$

In both the NSE regime and the extreme ASE regime, our calculated values of z_{\pm}^S agree with the z_{\pm}^S predicted by the thick slab expressions [4.14], [7.1], and [7.2] whenever $d/\delta > 3$ or 4. In fact, the closed forms for z_{\pm}^S provided a useful check on the computer programs written to implement the numerical solutions or our boundary value problem.

Although integral expressions exist^{4,8} that can be used to calculate z_{\pm}^S for any mean free path l , to our knowledge we are the first to explicitly calculate the variation of z_{\pm}^S with H_0 in a ferromagnetic metal when $\delta/l \approx 1$ (the NSE-ASE transition

region). In doing so we have come across two interesting results. First, the surface impedances are predicted to stop changing with l when $\delta/l \leq 1$ (see figure 27). This implies that the rf electric fields in the skin layer (which govern z_{\pm}^S) are essentially constant when l exceeds δ . Second, since z_{\pm}^S are insensitive to changes in l in the ASE regime, it might be possible to analyze surface impedance data obtained in the ASE regime ($\delta/l \leq 1$) using existing theory^{48, 50} developed for the limiting case of $\delta/l \ll 1$ (extreme ASE regime). The latter theory is much easier to work with mathematically than the general theory required to treat the case of $\delta/l \leq 1$ directly.

7.2.2 Variation of T_- with H_0 , l and d

In figure 28 we plot $\log_{10}|T_-|$ vs. H_0 for $0.006 \mu\text{m} \leq l \leq 25 \mu\text{m}$ and slab thicknesses $d = 2 \mu\text{m}$ (fig. 28), $d = 5 \mu\text{m}$ (fig. 29), and $d = 10 \mu\text{m}$ (fig. 30).

The variation of T_- with l is qualitatively the same for all three slab thicknesses. Basically, we can see that when $\delta/l > 1$, the transmission is nearly independent of the type of surface scattering. When $l = 0.006 \mu\text{m}$ (roughly corresponding to the mean free path in Nickel at room temperature) the calculated transmission curves agree with the transmission calculated using the NSE transmission coefficients [4.13] derived in chapter 4. A transmission maximum occurs at a value of H_0 corresponding to FMAR and a deep minimum occurs at a value of H_0 corresponding to

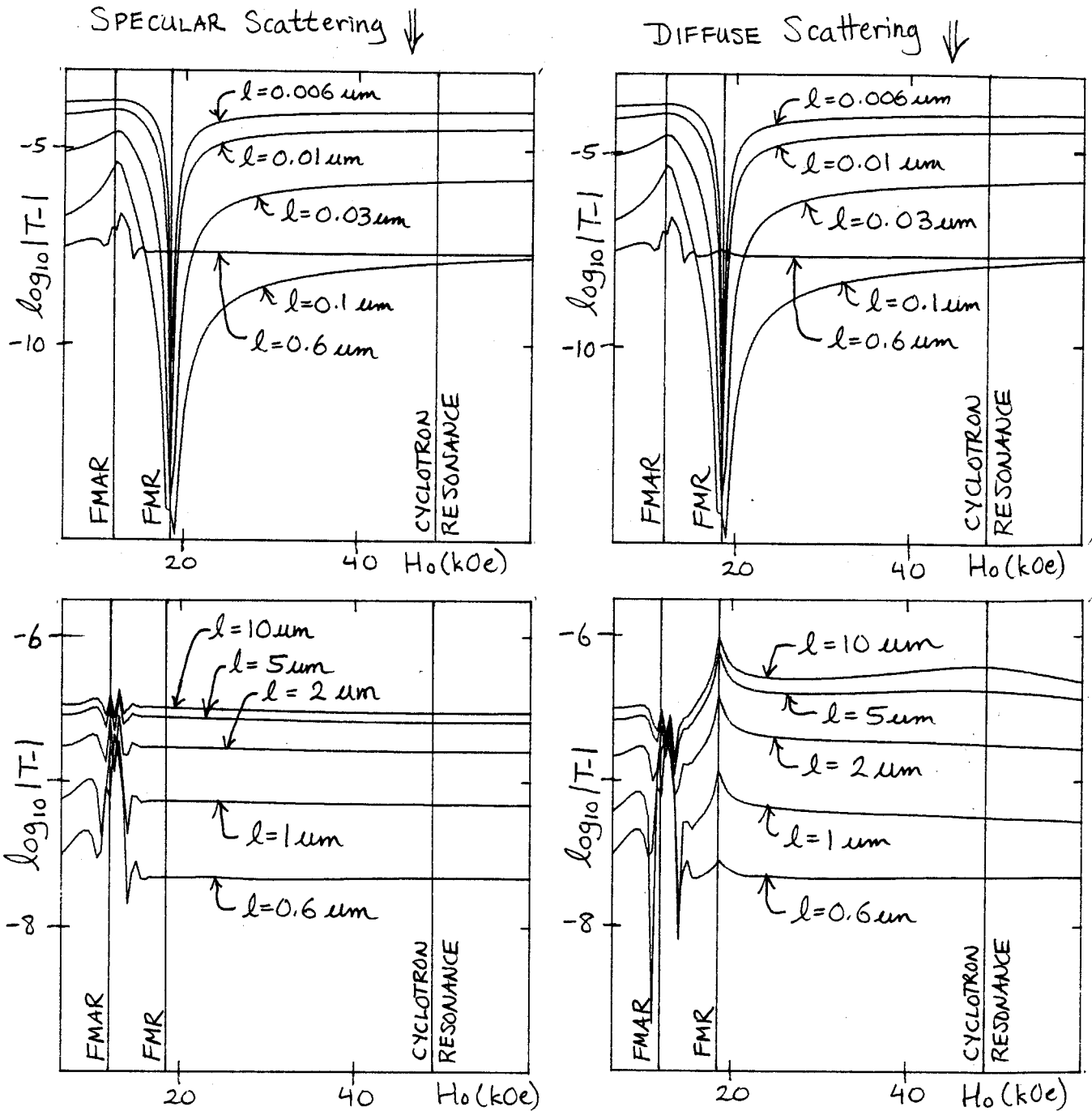


Fig. 28 Plots of $\log_{10}|T_-|$ vs H_0 for $d = 2 \mu\text{m}$ and various mean free paths l . The calculations were carried out using the Nickel parameters of Appendix A.

SPECULAR Scattering ↓

DIFFUSE Scattering ↓↓

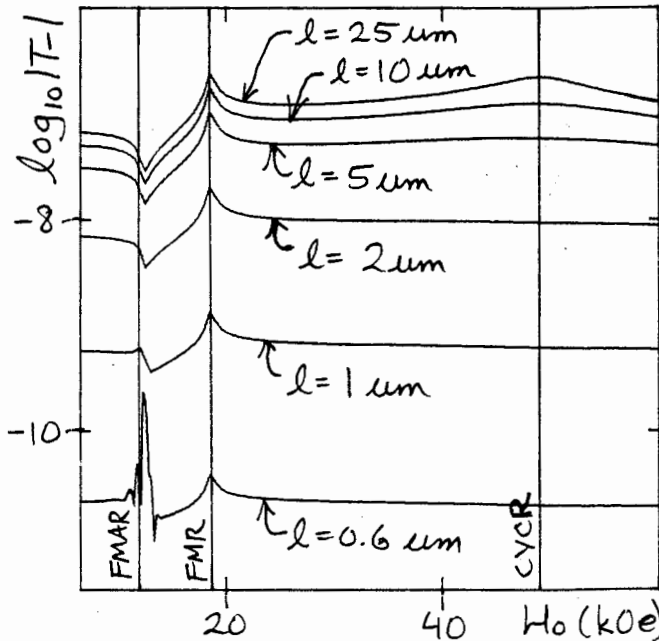
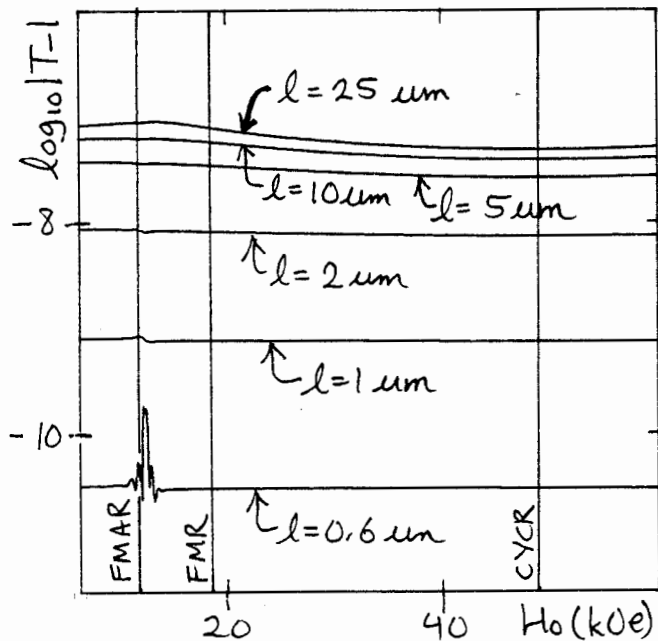
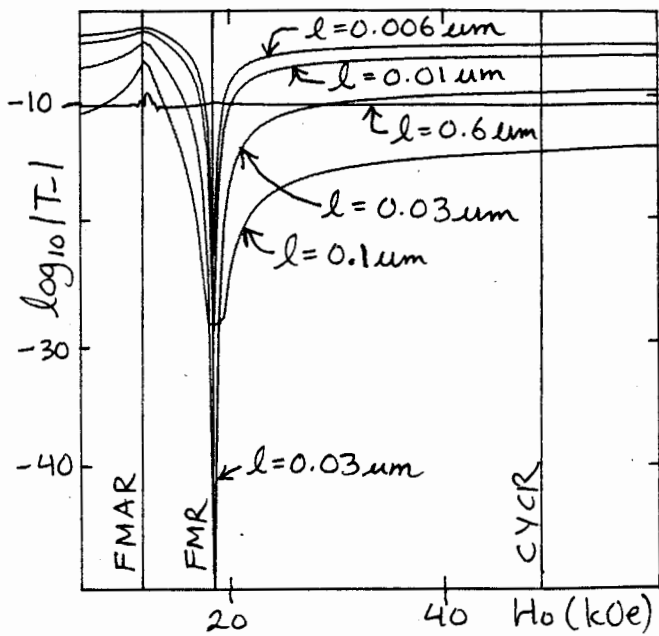
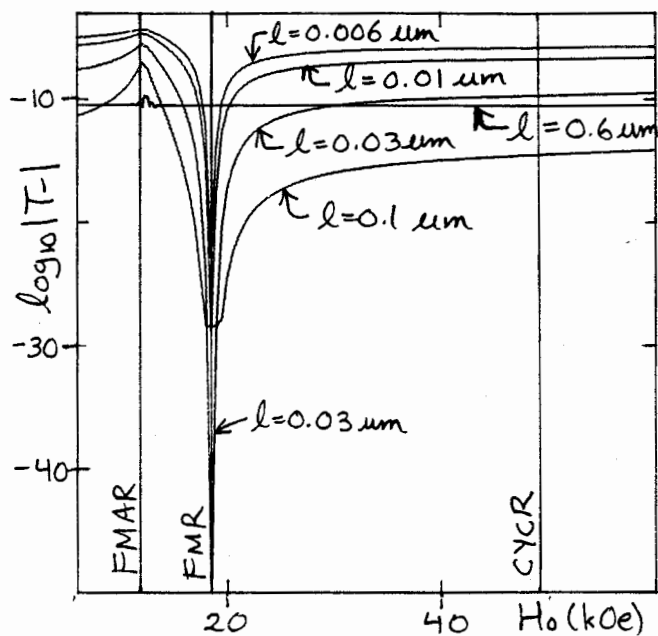


Fig. 29 Plots of $\log_{10}|T-1|$ vs H_0 for $d = 5 \mu\text{m}$ and various mean free paths l . The calculations were carried out using the Nickel parameters of Appendix A.

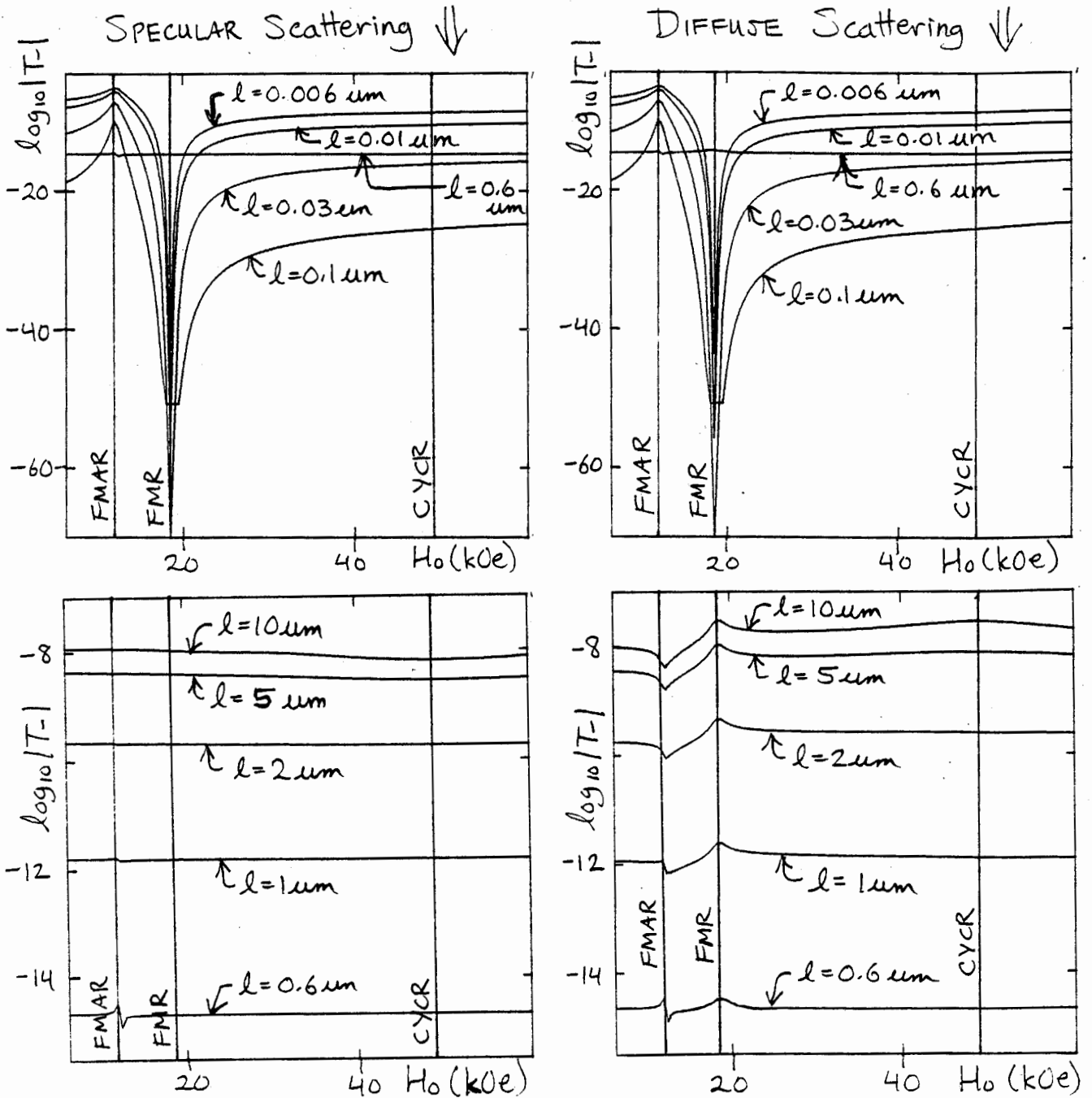


Fig. 30 Plots of $\log_{10}|T-|$ vs H_0 for $d = 10 \mu\text{m}$ and various mean free paths l . The calculations were carried out using the Nickel parameters of Appendix A.

FMR. The effect of increasing l is to cause the FMAR peak to narrow and attenuate while the FMR minimum increases and broadens. In the NSE-ASE transition regime, where $\delta/l \approx 1$, the T_- curves go through an overall minimum and then increase with l . In the ASE regime ($\delta/l \leq 1$) the magnitude of T_- , for a given slab thickness d , varies with l but is essentially independent of the type of surface scattering. However, the surface scattering definitely has an effect on the transmission lineshape. Referring to figures 28-30, we see that the T_- curves calculated for $l = 0.6 \mu\text{m}$ develop complicated structure at FMAR for both specular and diffuse surface scattering but only the T_- curve calculated for diffuse scattering develops a peak at FMR. No such FMR peak is predicted by the specular scattering calculation.

As l is increased further, the transmission curves calculated for specular surface scattering predict that the complicated structure at FMAR will give way to a broad maximum while a broad minimum will develop at a value of H_0 corresponding to cyclotron resonance (see the T_- curves calculated for $l = 10 \mu\text{m}$ in figures 28-30). No interesting features are predicted to develop at FMR. In contrast, the T_- curves calculated for diffuse surface scattering develop a minimum at FMAR, a maximum at FMR, and a broad maximum at cyclotron resonance when $d/l < 1$.

7.2.3 Variation of T_+ with H_0 and l

In figure 28 we plot $\log_{10}|T_+|$ vs. H_0 for $0.006 \mu\text{m} \leq l \leq 25 \mu\text{m}$ and for slab thicknesses $d = 2 \mu\text{m}$ (fig. 31), $d = 5 \mu\text{m}$ (fig. 32), and $d = 10 \mu\text{m}$ (fig. 33).

Similar to the results found for T_- , we can see that when $\delta/l > 1$, the transmission is essentially independent of the type of surface scattering. When $l = 0.006 \mu\text{m}$ the calculated transmission curves agree with the transmission calculated using the NSE transmission coefficients [4.13] derived in chapter 4: the T_+ curves exhibit a monotonic increase with H_0 . The effect of increasing l is to cause an overall decrease in the transmission amplitude. The curves go through a minimum in the NSE-ASE transition region and then begin to increase in amplitude. In the ASE regime ($\delta/l \leq 1$), the surface scattering once again affects the transmission lineshape. In figure 31 we see that the curves calculated for diffuse scattering now decrease monotonically with H_0 while the T_+ curves calculated for specular surface scattering increase monotonically with H_0 .

7.3 Discussion of the Transmission Behaviour

An understanding of the variation of T_{\pm} with l , and how T_{\pm} depends on the surface scattering, can be obtained from a study of the integral form of T_{\pm} derived in section 6.6 for specular

SPECULAR Scattering ↓

DIFFUSE Scattering ↓

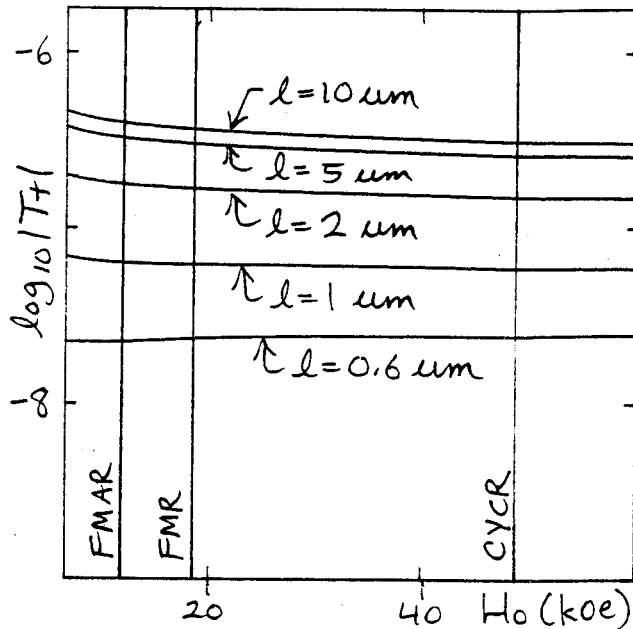
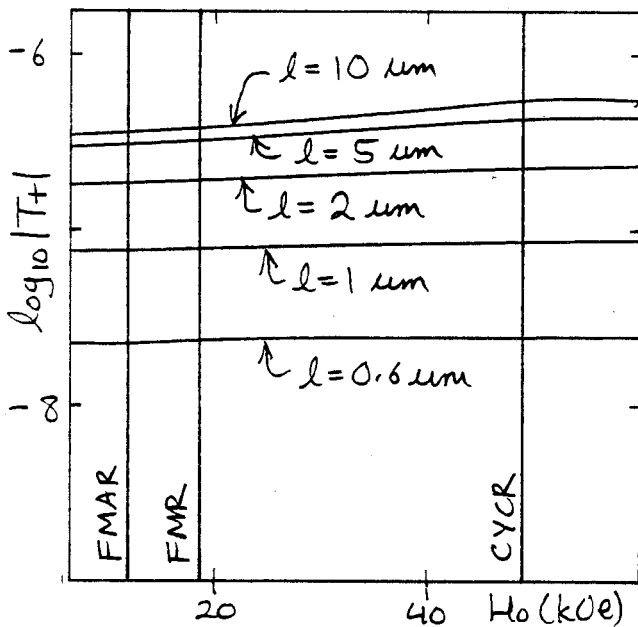
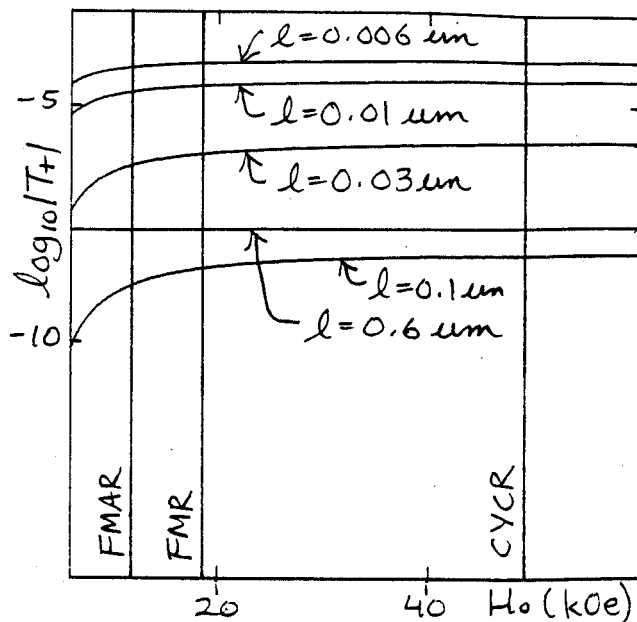
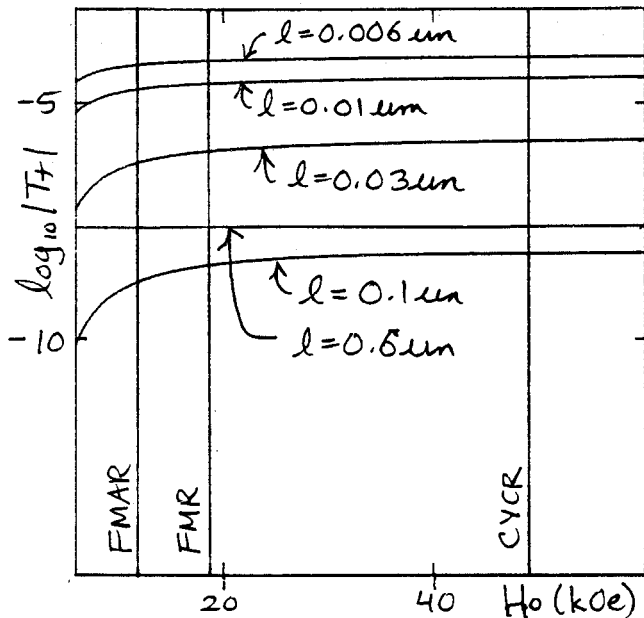


Fig. 31 Plots of $\log_{10}|T_+|$ vs H_0 for $d = 2 \mu\text{m}$ and various mean free paths l . The calculations were carried out using the Nickel parameters of Appendix A.

SPECULAR Scattering ↓

DIFFUSE Scattering ↓

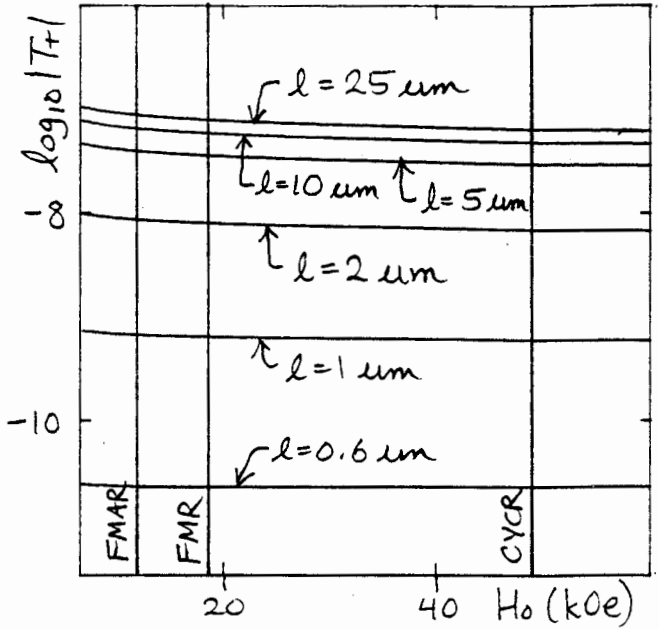
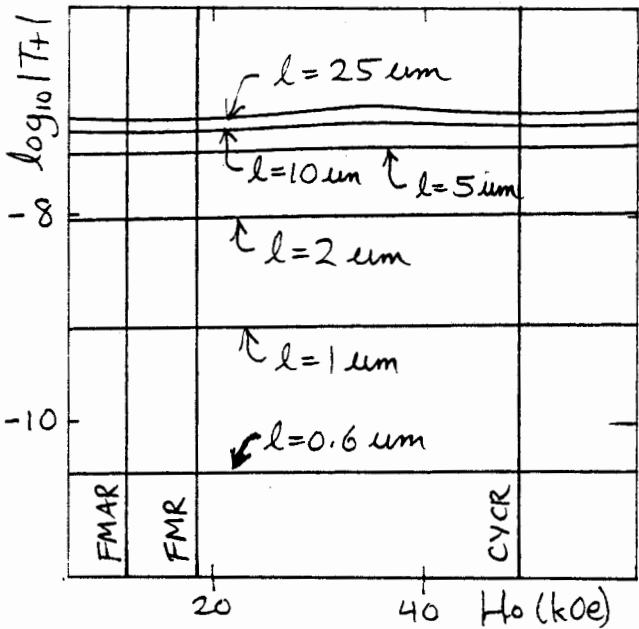
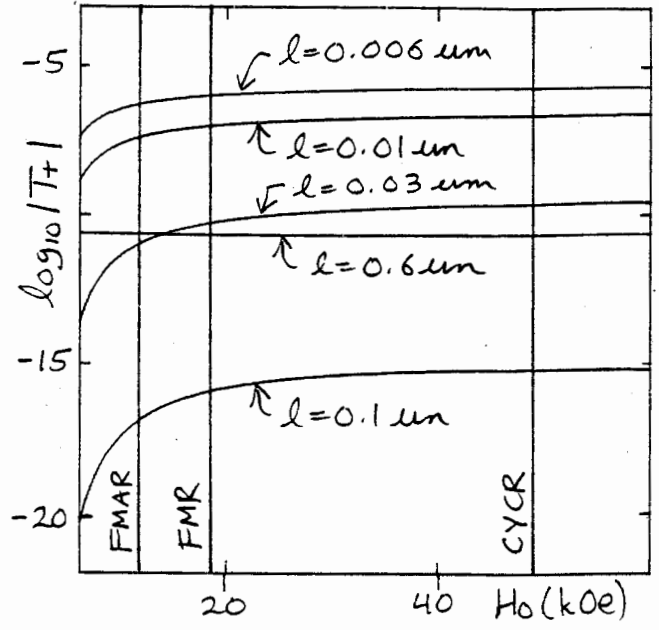
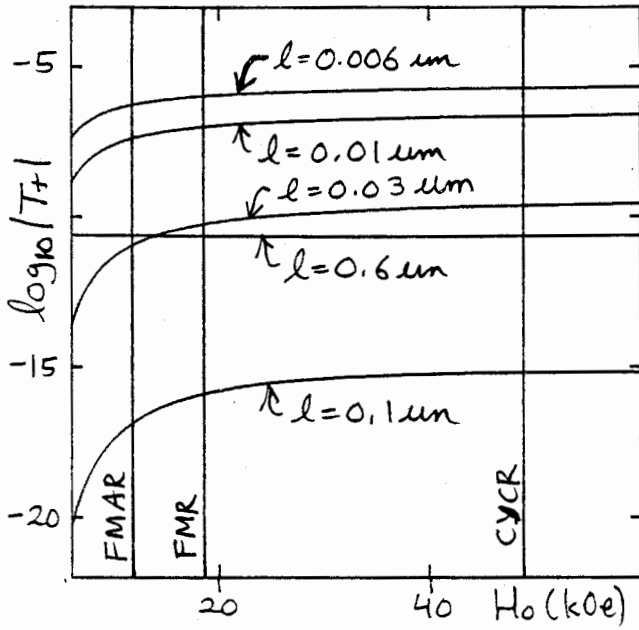


Fig. 32 Plots of $\log_{10}|T_+|$ vs H_0 for $d = 5 \mu\text{m}$ and various mean free paths l . The calculations were carried out using the Nickel parameters of Appendix A.

SPECULAR Scattering ↓

DIFFUSE Scattering ↓

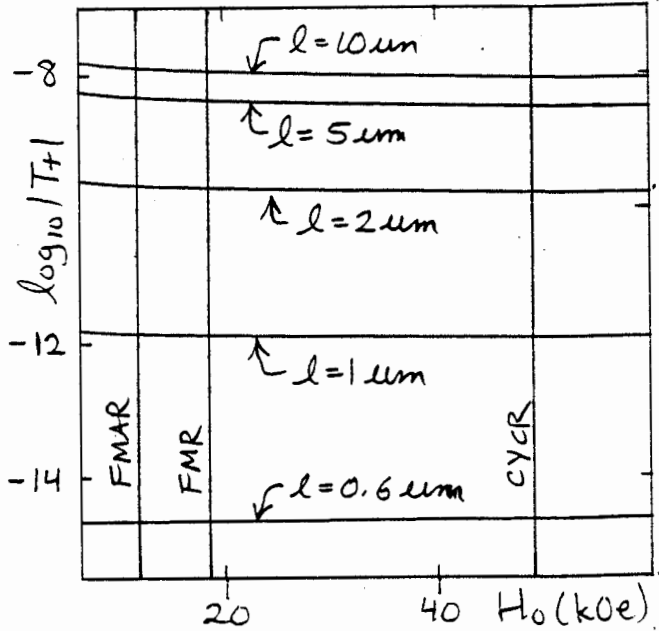
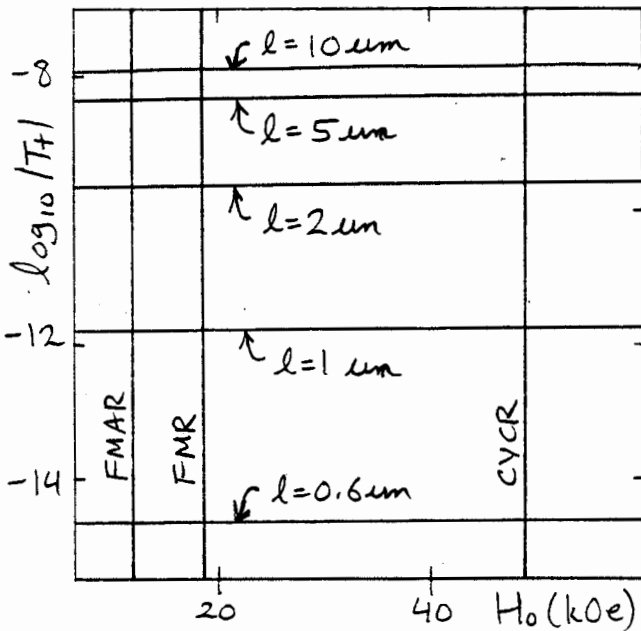
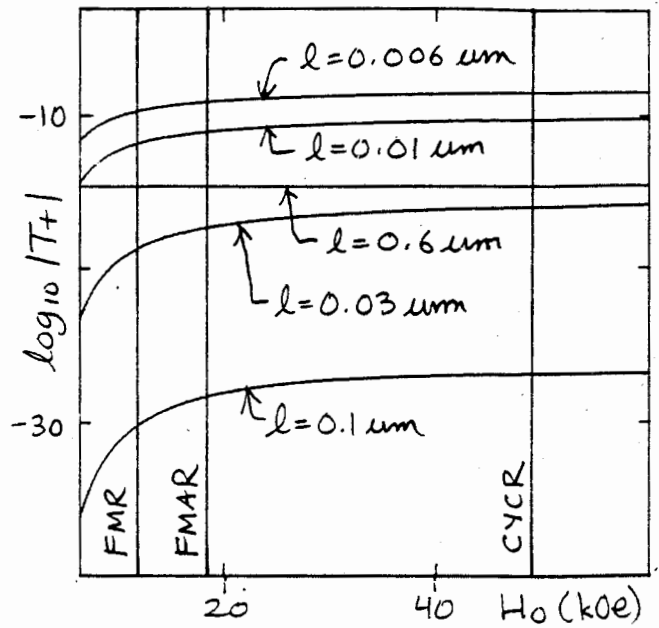
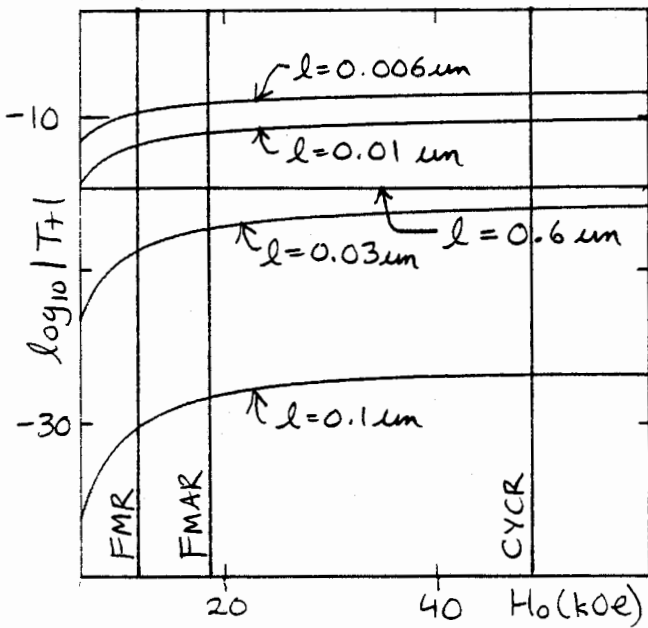


Fig. 33 Plots of $\log_{10}|T_+|$ vs H_0 for $d = 10 \mu\text{m}$ and various mean free paths l . The calculations were carried out using the Nickel parameters of Appendix A.

surface scattering and a thick slab ($d/l \gg 1$). We had:

$$T_{\pm} = -\frac{8i\omega\mu}{c} \frac{l}{L\Delta X} \sum_i \frac{e^{-L\Delta X \frac{d}{2}}}{2y_i + \alpha k(y_i)} - \frac{8}{3} \frac{\omega}{c} \frac{(\delta^2 l)}{d^2} e^{-L\Delta X (\frac{d}{2})} \quad [6.70]$$

The integral form was derived by replacing the infinite sum solution of T_{\pm} by a sum of residues (the first term of [6.70]) and a contour integral (the second term of [6.70]).

By plotting both terms of [6.70] vs. H_0 and l one can readily determine that the residue term governs the behaviour of T_{\pm} in the NSE regime ($\delta/l > 1$) while the integral term governs the behaviour of T_{\pm} in the ASE regime ($\delta/l < 1$). This is illustrated in figures 34 and 35 where we plot the two terms making up T_{\pm} as functions of H_0 for $d = 5 \mu\text{m}$, $l = 0.03 \mu\text{m}$ (NSE regime - fig. 34) and $l = 2.0 \mu\text{m}$ (ASE regime - fig. 35). In the NSE regime, d/l was so large that the integral term was effectively zero. The residue term is entirely responsible for the transmission behaviour when $\delta/l > 1$. When $\delta/l \gg 1$, the residue term reduces to the NSE transmission coefficient [4.13]. As l is increased, the real parts of the roots y_1 and y_2 steadily increase with l , leading to the attenuation of the T_{+} and T_{-} curves when $\delta/l > 1$. (see figure 29, for example). When $\delta/l \leq 1$, the residue term virtually stops changing with l . The integral term is a steadily increasing function of l . When $\delta/l \approx 1$ (the NSE-ASE transition region), the integral term becomes comparable to the residue term leading to the interference effects noted on the T_{\pm} curves calculated for $l = 0.6 \mu\text{m}$ and shown in figures 28 to 30. Further increases in

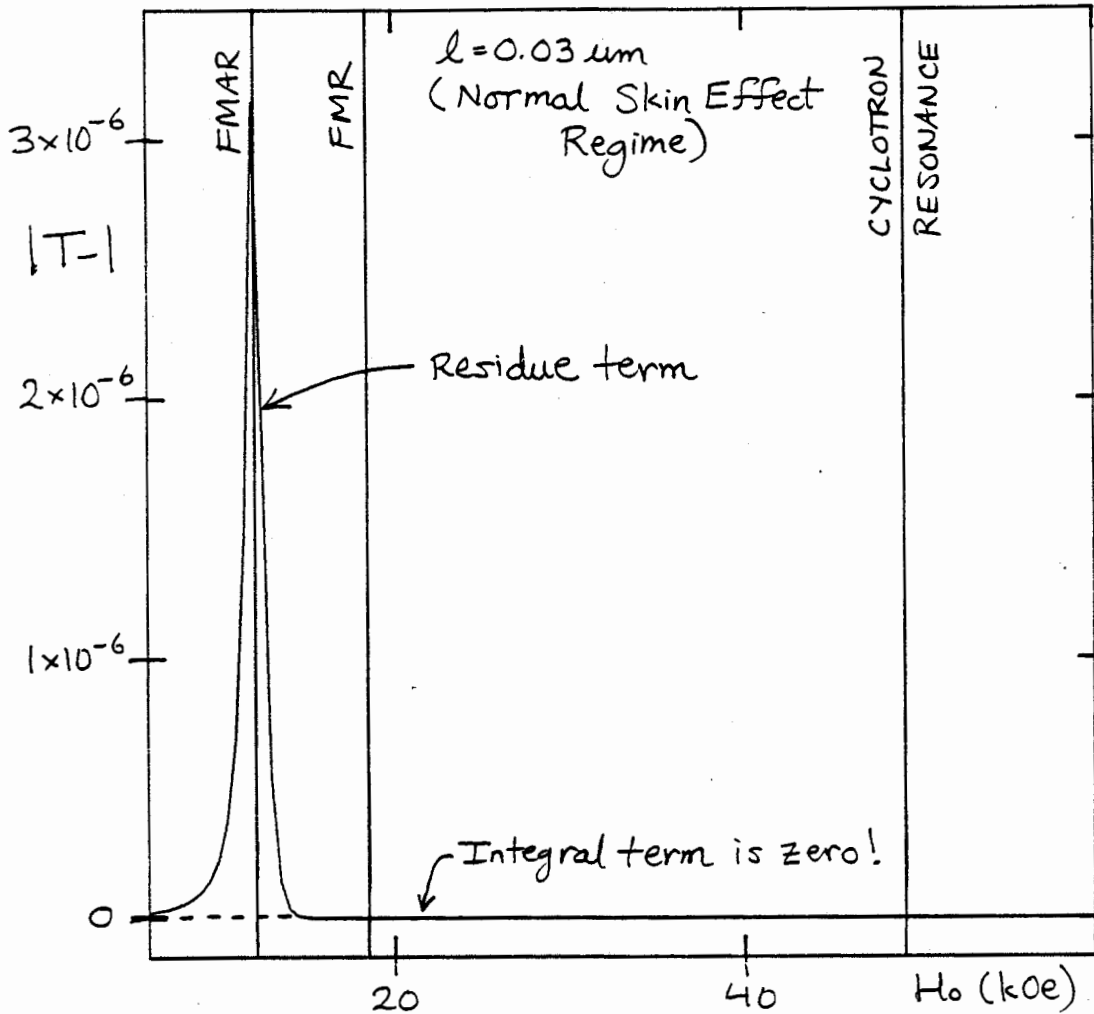


Fig. 34 Plots of the residue and integral terms that make up T_+ for the case of specular surface scattering, $d = 5 \mu\text{m}$ and $l = 0.03 \mu\text{m}$. The residue term dominates the transmission in the NSE regime.

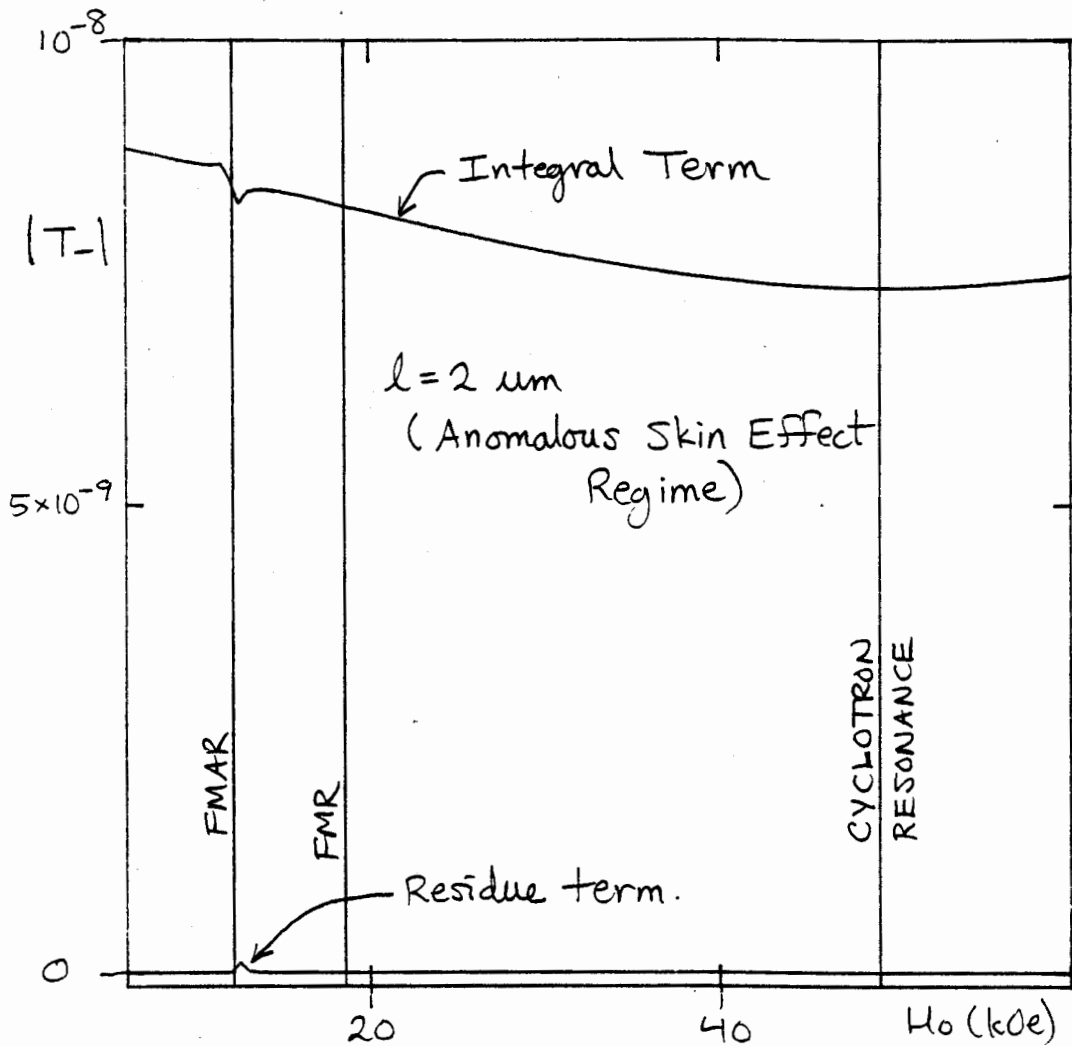


Fig. 35 Plots of the residue and integral terms that make up T_+ for the case of specular surface scattering, $d = 5 \mu\text{m}$ and $l = 2 \mu\text{m}$. The integral term dominates the transmission in the ASE regime.

l cause the integral term to increase in amplitude and become the dominant contribution to T_{\pm} in the ASE regime (see figure 35).

Physically, we associate the residue term in T_{\pm} with the transport of electromagnetic wave energy across the slab; the integral term is associated with energy transport across the slab by conduction electrons that enter the front surface skin layer, collide with the $z = 0$ slab face, and head back out into the slab carrying away energy picked up from the electric fields in the skin layer.

In the NSE regime, where $\delta/l \gg 1$, l is so small that most of the conduction electrons cannot carry energy out of the skin layer and across the slab. Hence, the electric fields at the rear of the slab (which govern T_{\pm}) are primarily due to the propagation of microwave radiation across the slab and, therefore, are not seriously affected by the type of surface scattering.

However, since σ_0/l is a constant in our metal then increasing l will increase σ_0 . Since the skin depth δ is proportional to $\sigma_0^{-1/2}$ the transmission associated with the propagation of microwave radiation across the slab must decrease with increasing l . This is precisely the behaviour exhibited by the residue term in T_{\pm} and in the plots of T_{\pm} vs. H_0 calculated for $\delta/l > 1$ in figures 28-33.

When l increases enough to make $\delta/l \approx 1$ (the NSE-ASE transition region), the conduction electrons can begin to carry

energy picked up in the skin layer out into the slab and contribute to the electric field distribution. The longer l becomes, the larger this contribution to the electric field will be. Since the conduction electrons generating the additional fields in the slab had to collide with the front surface skin layer before they could head back into bulk of the slab we should expect the electric fields in the slab, and therefore T_{\pm} , to be affected by the surface scattering. Our calculated results shown in figures 28 to 33 seem to confirm this.

The effect of surface scattering on the conduction electrons that generate the electric fields in the slab when $\delta/l \leq 1$ is explicitly illustrated in figure 36 where we have plotted $\ln|G_{\pm}(z)|$ vs both H_0 ($6 \leq H_0 \leq 60$ kOe) and z ($0 \leq z \leq 5 \mu\text{m}$) for $d = 5 \mu\text{m}$ and $l = 25 \mu\text{m}$. Comparing the two plots in figure 36 we can clearly see that the electric fields generated in the skin layer by the incident microwaves for specular and diffuse scattering are remarkably similar. However, outside the skin layer, the electric fields definitely depend on the type of surface scattering. The electric field distribution for specular scattering is remarkable devoid of any interesting H_0 dependent features except near FMAR. In contrast, the electric field distribution generated for the case of diffuse surface scattering seems to "image" the electric fields in the skin layer all the way across the slab.

The electric field plots of figure 36 also make clear the role played by surface scattering at the rear of the slab. For

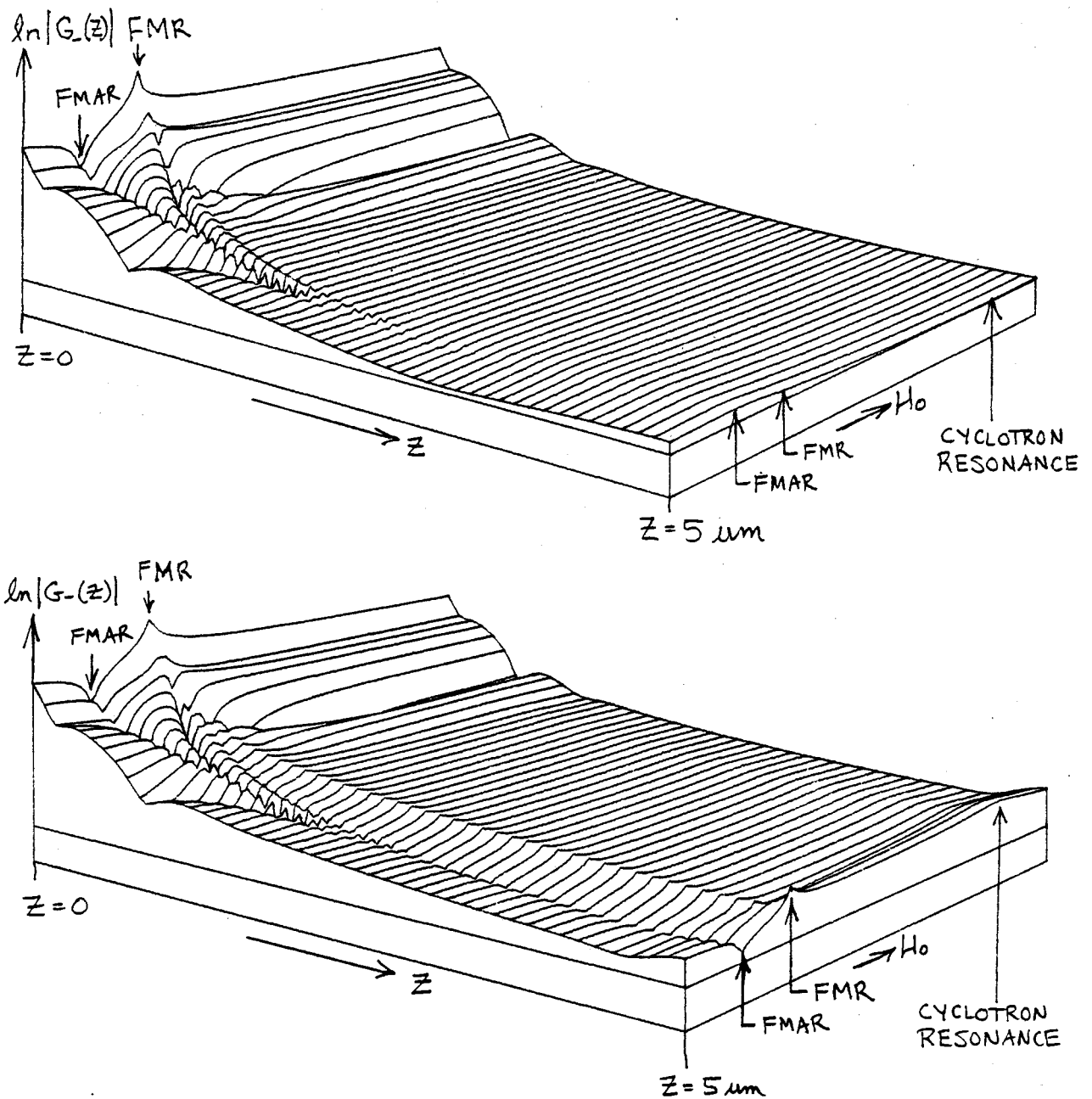


Fig. 36 $\ln|G(z)|$ plotted against depth z and the applied magnetic field H_0 for a $5 \mu\text{m}$ thick slab of Nickel. The electron mean free path was taken to be $l = 25 \mu\text{m}$. The parameters used in the calculation are listed in Appendix A.

specular scattering, the electric fields at $z = d$ are nearly the same as the electric fields in the bulk. In contrast, Baraff^{24, 23} has shown that the presence of a diffusely scattering boundary at the rear of the slab enhances the electric field distributions near $z = d$. Further, diffuse scattering at the $z = d$ slab face is directly responsible for the transmission peak at cyclotron resonance²³. Both the sharpening of the field distribution and the generation of the cyclotron resonance peak near the rear of the slab are clearly evident in figure 36.

7.4 Scaling Properties of the Transmission Coefficients

In section 6.6 we derived an expression for the transmission coefficients T_{\pm} for a thick slab ($d/l \gg 1$) and specular surface scattering (see equation [6.70]). In the ASE regime, the residue term in the thick slab expression is negligible and the transmission is given by the integral term:

$$T_{\pm} \left(\frac{d}{l} \gg 1 \right) = -\frac{8}{3} \frac{\omega}{c} \frac{(\delta_0^2 l)}{d^2} e^{-LAX \frac{d}{l}} \quad [7.3]$$

We have found that the thick slab expression [7.3] has the useful property that it can predict the magnitude of T_{\pm} within a factor of 2 or 3 when $\delta/l \leq 1$ and $d/\delta > 3$ or 4. This is illustrated in figures 37 and 38 where we have plotted the

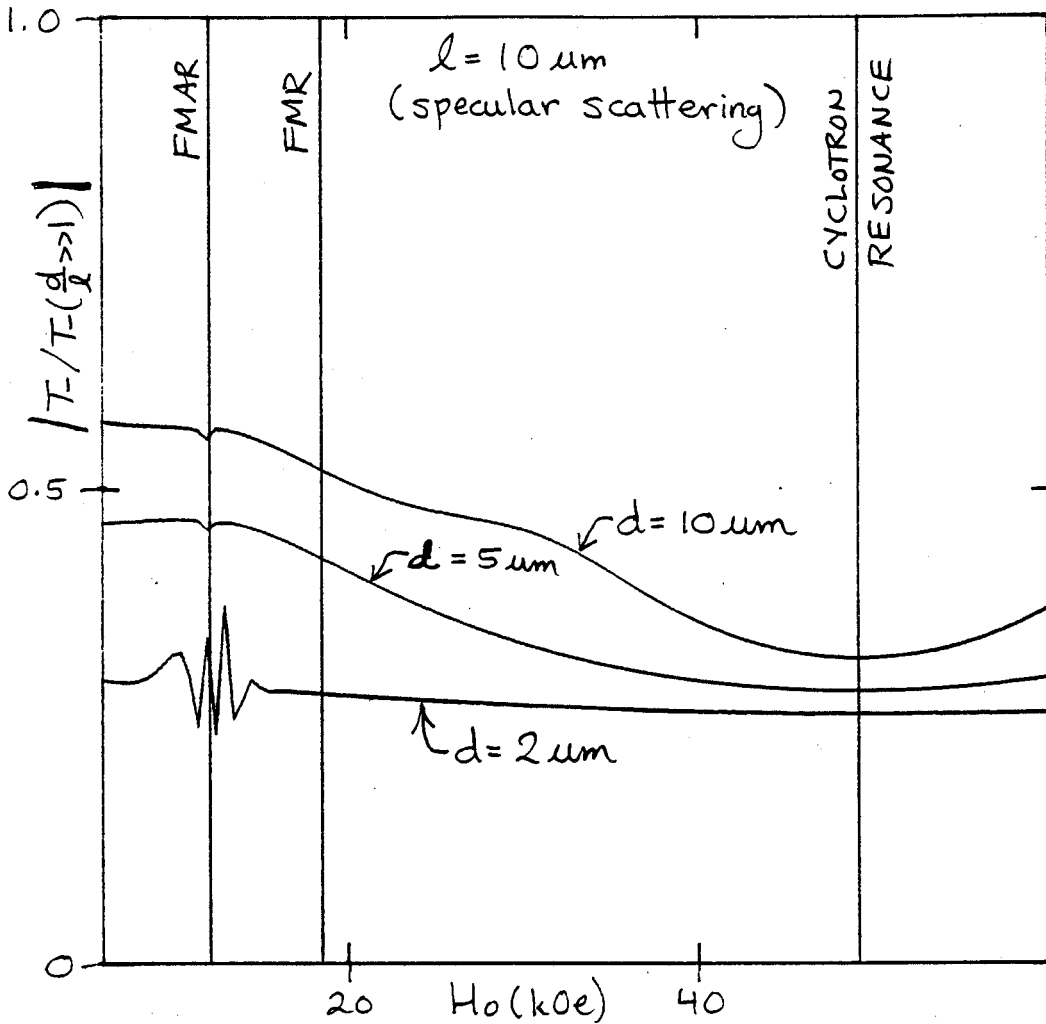


Fig. 37 Plots of $|T_-/T_-(d/l \gg 1)|$ vs H_0 for $l = 10 \mu\text{m}$ and $d = 2, 5, \text{ and } 10 \mu\text{m}$. Specular surface scattering was assumed. The plots clearly show that the magnitude of T_- is given to within a factor of 2 by the thick slab, specular scattering expression.

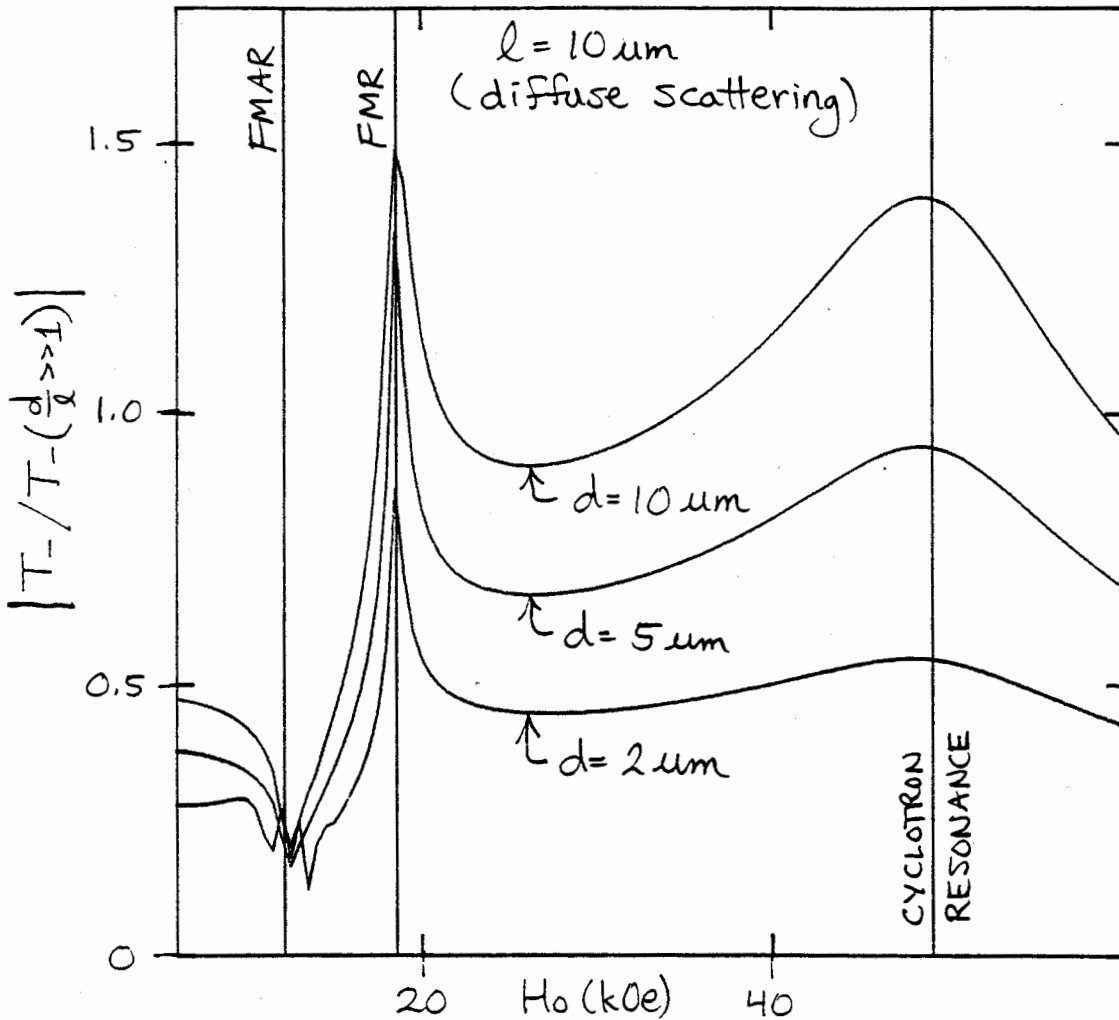


Fig. 38 Plots of $|T_- / T_-(d/l \gg 1)|$ vs H_0 for $l = 10 \mu\text{m}$ and $d = 2, 5, \text{ and } 10 \mu\text{m}$. Diffuse surface scattering was assumed. The plots clearly show that the magnitude of T_- is given to within a factor of 2 by the thick slab, specular scattering expression.

transmission ratios $|T_-/T_-(d/l \gg 1)|$ for both specular and diffuse surface scattering when $l = 10 \mu\text{m}$ and $d = 2, 5, \text{ and } 10 \mu\text{m}$. In all cases, the transmission ratio is of the order of 0.5 to 1.5. One also finds that for fixed l , the variation of $|T_-/T_-(d/l \gg 1)|$ with H_0 is approximately constant. The scaling law can prove useful for the common situation where one has calculated T_{\pm} as a function of H_0 and l for one particular value of d and then must compare the calculations to experimental data obtained using a slab of a slightly different thickness.

7.5 The Linearly Polarized Transmission Coefficient

Although our analysis of the transmission behaviour has been most conveniently carried out in terms of the circularly polarized transmission coefficients T_{\pm} , we do not measure T_+ or T_- in an actual microwave transmission experiment. Rather, we measure T , the linearly polarized transmission coefficient which we defined in section 2.5 as

$$T = [T_+ + T_-]/(2\beta_0 Z_0) \quad [2.106]$$

where β_0 is the cavity amplitude factor and Z_0 is the propagating waveguide impedance.

For a system designed to measure the transmission of 24 GHz microwave radiation³⁴, $\beta_0 = 2.32 \times 10^{-2}$, and $Z_0 = 1.23$. Using

the published values of β_0 and Z_0 we have calculated and plotted $\log_{10}|T|$ as a function of H_0 for $l = 1, 2, 5,$ and $10 \mu\text{m}$ and $d = 2 \mu\text{m}$ (figs. 39-40), $d = 5 \mu\text{m}$ (figs. 41-42), and $d = 10 \mu\text{m}$ (figs. 43-44).

Perhaps the most striking feature of the T vs. H_0 curves are the amplitude oscillations whose period varies with the slab thickness d and whose amplitude varies with l . The amplitude oscillations are called Gantmakher-Kaner oscillations⁴⁷ (or GKO). The GKO are have been observed in perpendicular configuration transmission experiments carried out on alkali metals at low temperatures⁵¹. The GKO are due to interference between the positive and negative circularly polarized transmission coefficients that combine to form T (see equation [2.106] above). To see this we consider the simplest case of a thick slab ($d/l \gg 1$) and specular surface scattering. When $\delta/l \leq 1$ then the circularly polarized transmission coefficients are given by [7.3]. Using [6.70] in [2.106] gives

$$\beta_0 Z_0 T = -\frac{8}{3} \frac{\omega}{c} \left(\frac{\delta_0^2 l}{d^2} \right) \cos\left(\omega_c \frac{d}{v_F}\right) e^{-[1-i\omega\tau] \frac{d}{l}} \quad [7.4]$$

Since ω_c varies with H_0 through

$$\omega_c = \frac{eH}{m^*c}$$

then [7.4] says that $|T|$ will vary cosinusoidally with H_0 . The

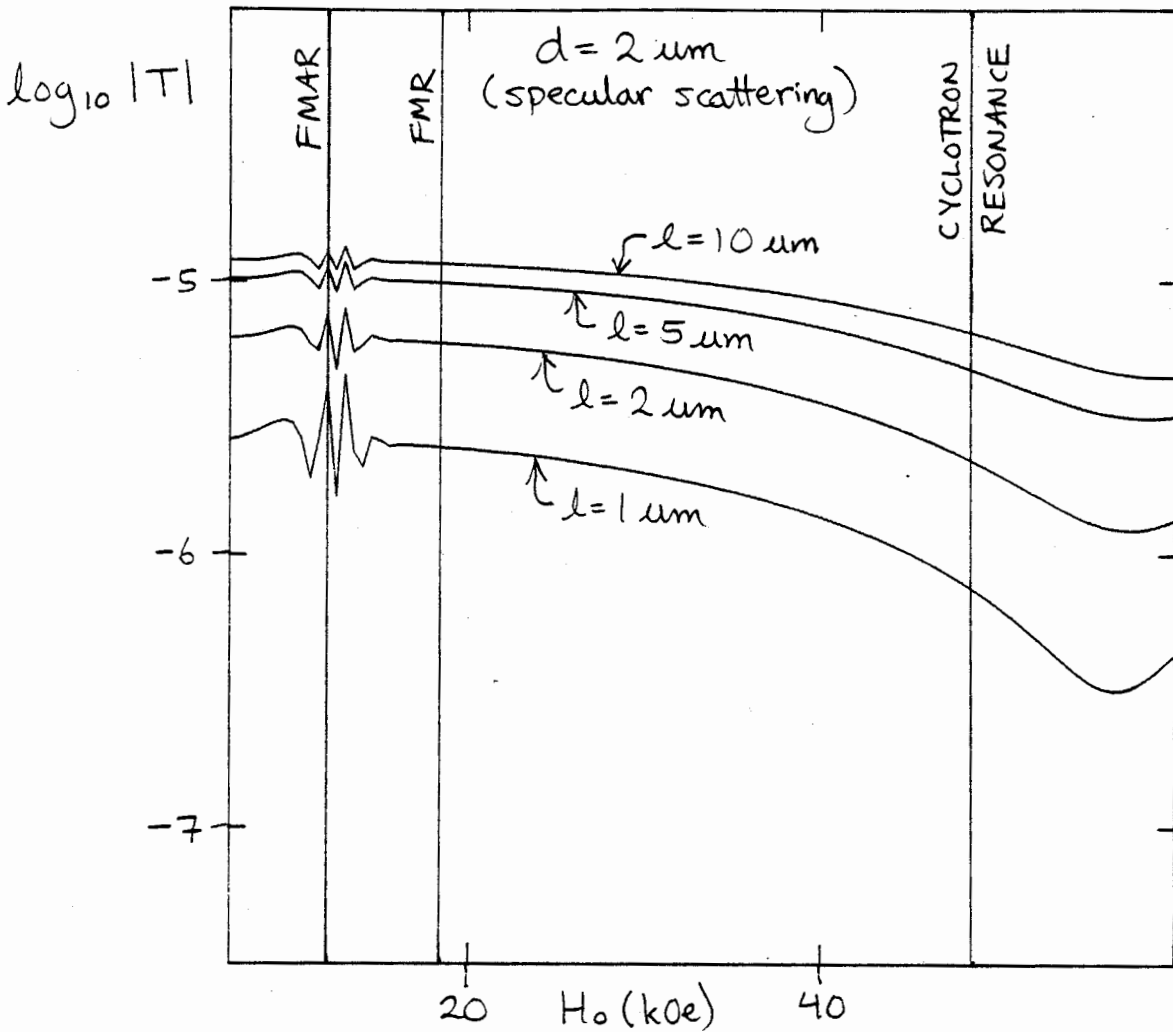


Fig. 39 Plots of $\log_{10} |T|$ vs H_0 for a 2 micron thick slab of Nickel with specular surface scattering. The calculations were carried out using the Nickel parameters of Appendix A. The mean free path varies from 1 μm to 10 μm .

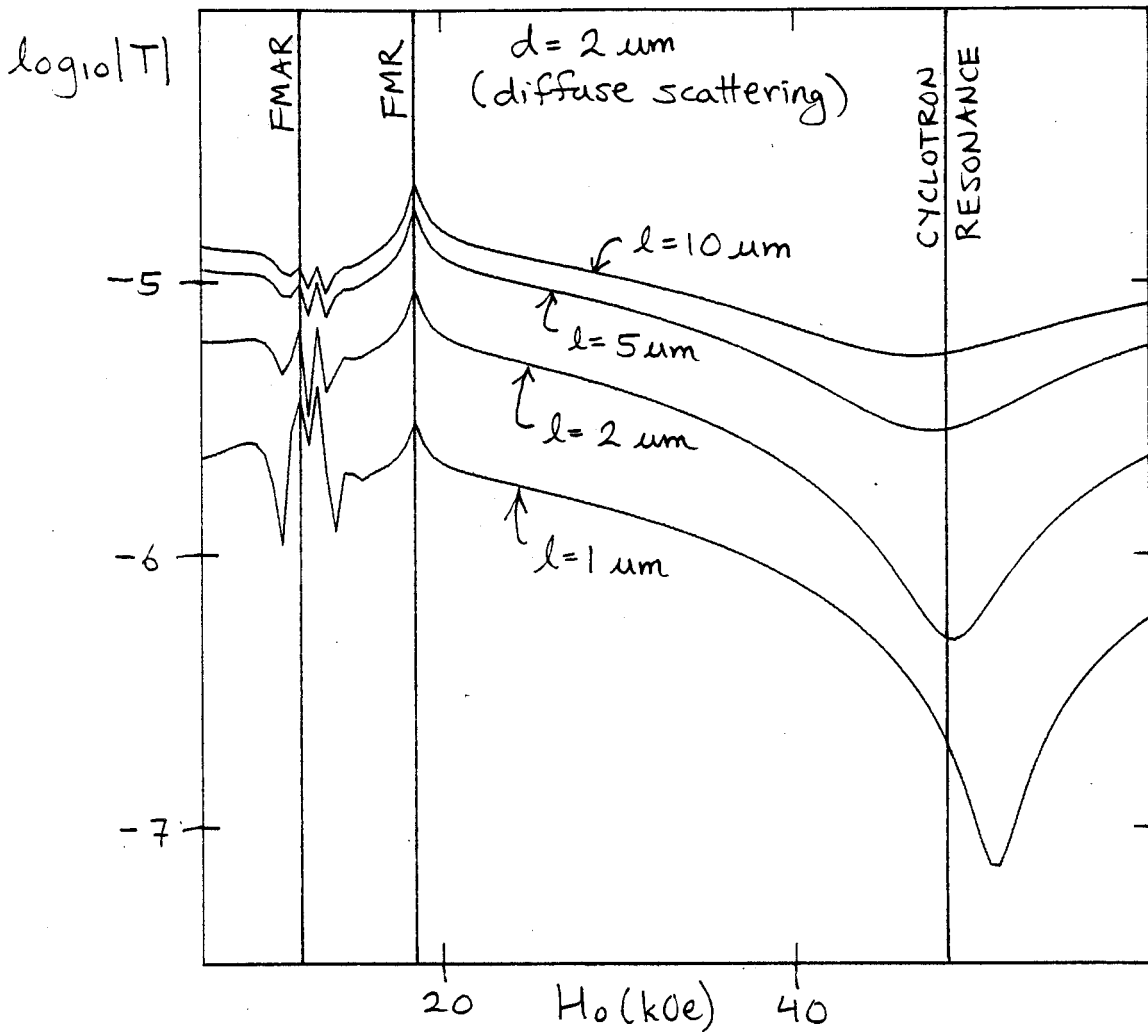


Fig. 40 Plots of $\log_{10}|T|$ vs H_0 for a 2 micron thick slab of Nickel with diffuse surface scattering. The calculations were carried out using the Nickel parameters of Appendix A. The mean free path varies from 1 μm to 10 μm .

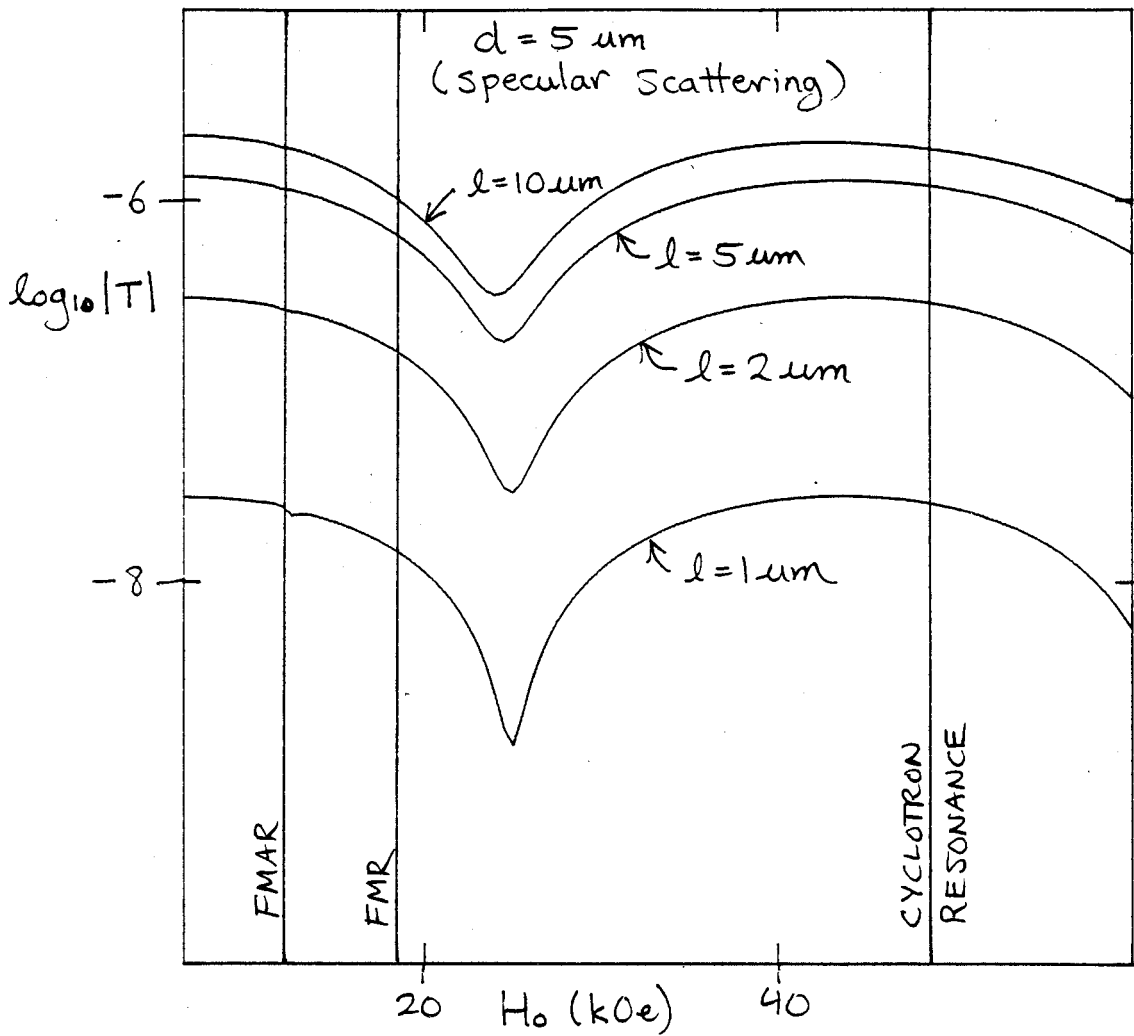


Fig. 41 Plots of $\log_{10}|T|$ vs H_0 for a 5 micron thick slab of Nickel with specular surface scattering. The calculations were carried out using the Nickel parameters of Appendix A. The mean free path varies from 1 μm to 10 μm .

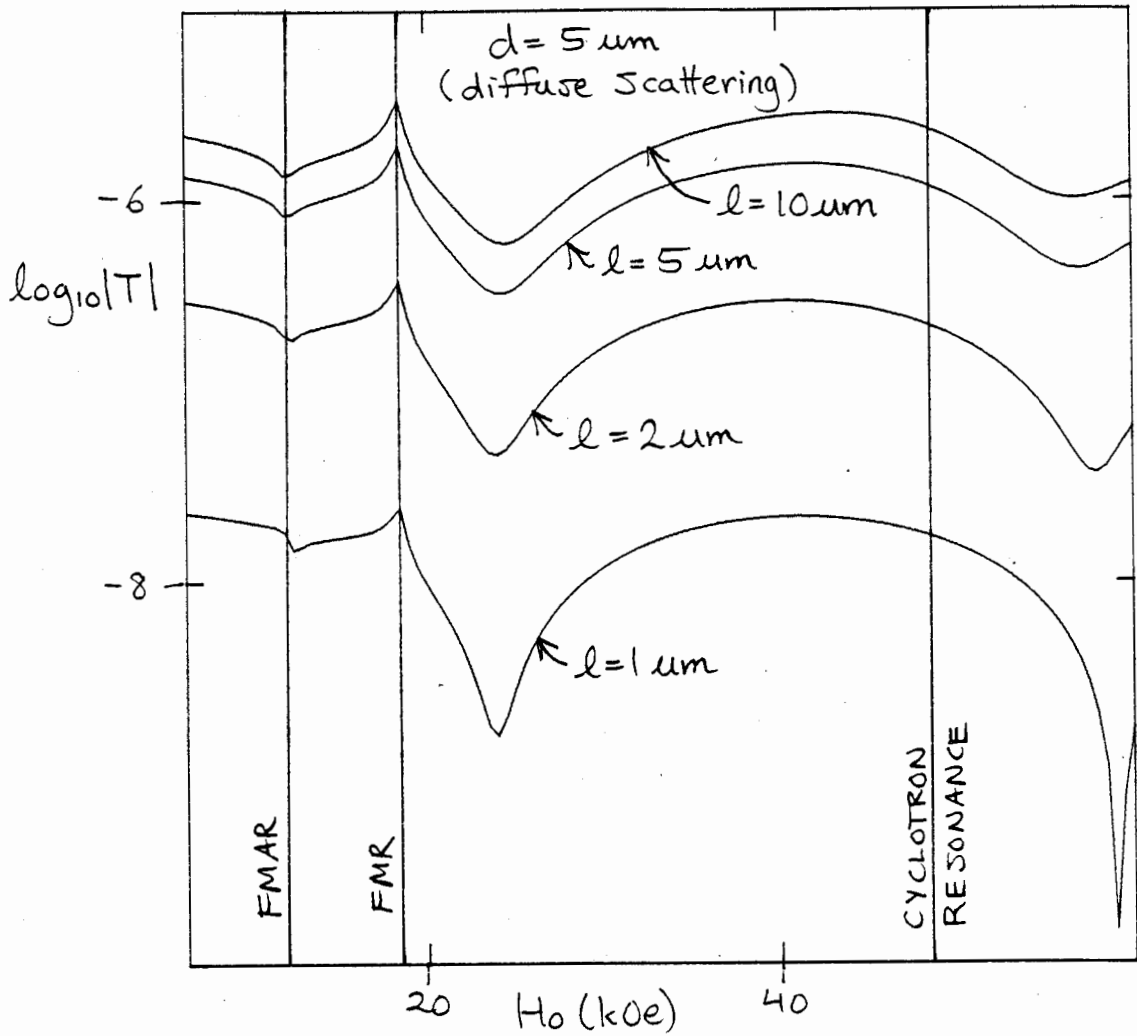


Fig. 42 Plots of $\log_{10}|T|$ vs H_0 for a 5 micron thick slab of Nickel with diffuse surface scattering. The calculations were carried out using the Nickel parameters of Appendix A. The mean free path varies from 1 μm to 10 μm .

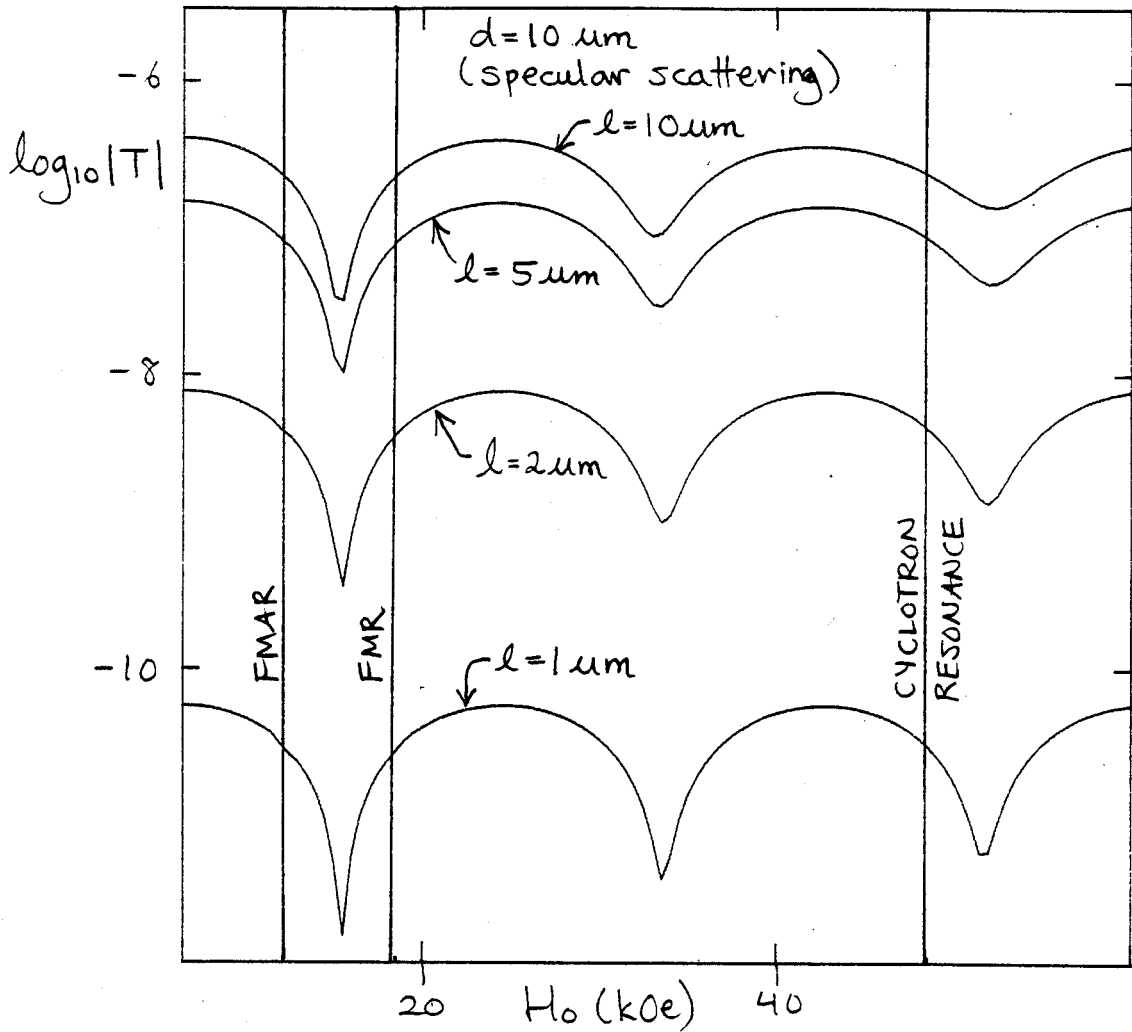


Fig. 43 Plots of $\log_{10}|T|$ vs H_0 for a 10 micron thick slab of Nickel with specular surface scattering. The calculations were carried out using the Nickel parameters of Appendix A. The mean free path varies from 1 μm to 10 μm .

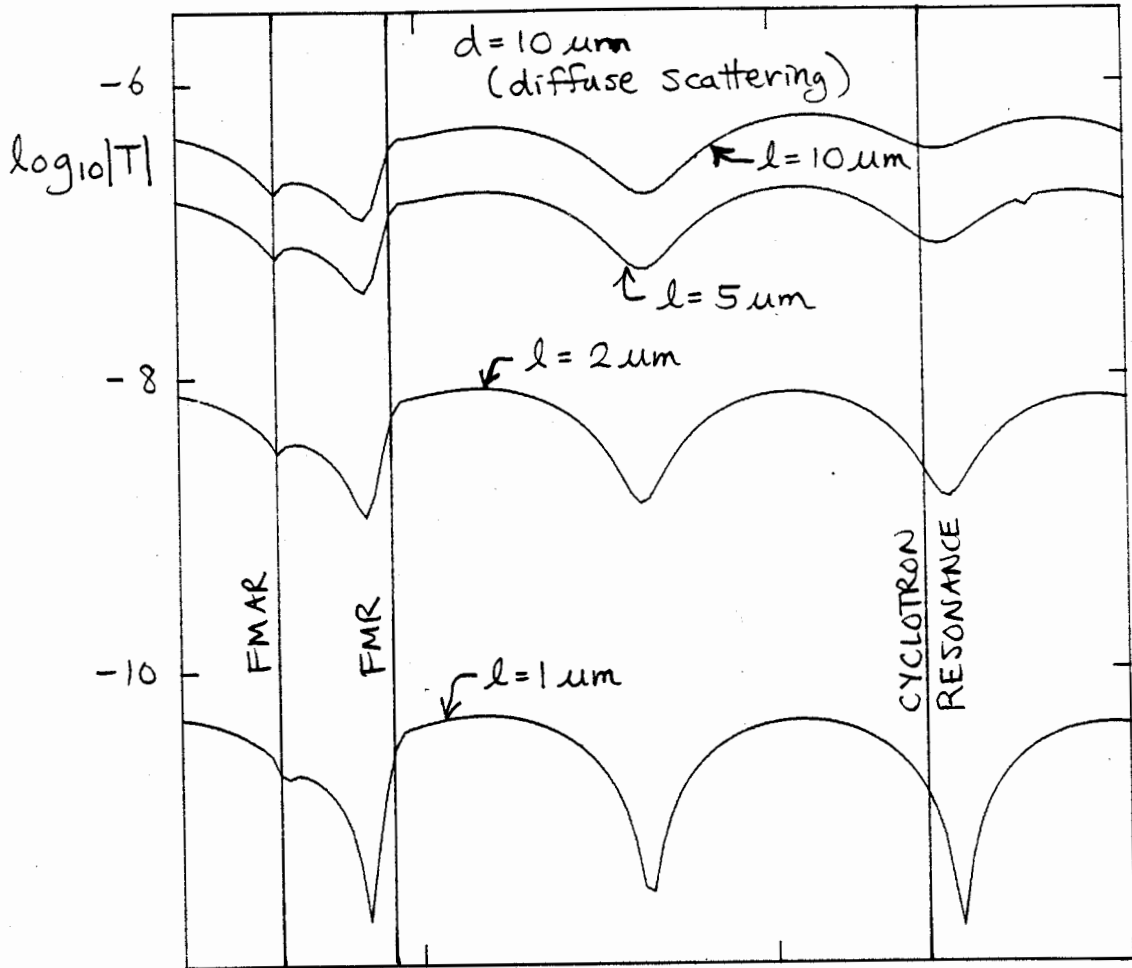


Fig. 44 Plots of $\log_{10}|T|$ vs H_0 for a 10 micron thick slab of Nickel with diffuse surface scattering. The calculations were carried out using the Nickel parameters of Appendix A. The mean free path varies from 1 μm to 10 μm .

spacing of the oscillations depends upon the Fermi surface parameters v_F and m^* and upon the slab thickness d . Not suprisingly, the period of the oscillations have been used to extract information about the curvature of the Fermi surface of several non-magnetic metals^{47, 51}.

In our case, the GKO will be superimposed over any transmission features associated with the magnetic response of our metal. One can see that the transmission features associated with the magnetic response of the metal cause considerable distortion of the GKO, the distortion being much stronger for the case of diffuse scattering than for specular scattering (compare figures 41 and 42, for example).

The distortion of the GKO should be readily observable in a transmission experiment. 24 GHz transmission systems have been described³⁴ that can measure transmitted signals down to 10^{-20} Watt. Such a system could therefore measure transmission features as small as $|T| \approx 10^{-10}$ if the specimen were irradiated with a 1 Watt microwave beam[†]. Referring to figures 39-44 we can see that the ASE transmission features predicted by our transmission calculations should be observable in slabs of Nickel 2 to 10 μm thick when the mean free path is over 1 μm . Such long mean free paths can be easily obtained at 4.2 K (liquid Helium temperature) if we use Nickel specimens with residual resistance ratios in excess of 1000 (for an RRR of

[†]The ratio of the incident to the transmitted microwave power is just $|T|^2$

1000, λ would be the order of 6 μm at 4.2 K).

Appendix A: Nickel Parameters

<u>Parameter Name</u>	<u>Value for Nickel</u>	<u>Definition</u>
M_S	510.1 Oe	Saturation Magnetization ⁵² .
$4\pi M_S$	6.410 kOe	Saturation Field.
ω/γ	7.827 kOe	Precessional Field ³ .
K_1	-1.1×10^6 ergs/cc.	First Anisotropy constant ⁵³ in Nickel at 4.2 K.
G	2.45×10^8 sec ⁻¹	Gilbert Damping Parameter ³ .
v_F	2.0×10^7 cm/sec.	Fermi Velocity ¹⁶ .
m^*/m_0	5.0	Effective Mass Ratio of Conduction Electrons ¹⁶ (m_0 = free electron mass).
r_{room}	6.0×10^{-6} Ohm-cm	Room temperature resistivity ⁵⁴ .

σ_0	$c^2 \cdot 10^{-9} / r$	Relation between d.c. conductivity and resistivity (σ_0 in esu, r in ohm-cm).
$\sigma_0(\text{room})$	1.498×10^{17} esu	d.c. conductivity at room temperature
l_r	6.516×10^{-3} microns	Estimated conduction mean free path at room temperature ³² .
σ_0 / l	2.299×10^{23} esu/cm	Ratio of d.c. conductivity to mean free path.

Appendix B: Linear and Circular Polarization

Consider a transverse electric field vector $\bar{\mathbf{E}}(z,t)$ that varies spatially in the z direction only and has a time dependence of $\exp(-i\omega t)$:

$$\bar{\mathbf{E}}(z,t) = \bar{\mathbf{E}}(z)\exp(-i\omega t) \quad [\text{B.1}]$$

Such a field vector is usually represented by a pair of orthogonal, linearly polarized, vectors $\bar{\mathbf{E}}_x(z,t)$ and $\bar{\mathbf{E}}_y(z,t)$ defined by

$$\bar{\mathbf{E}}_x(z,t) = E_x(z)\hat{\mathbf{x}}\exp(-i\omega t) \quad [\text{B.2}]$$

$$\bar{\mathbf{E}}_y(z,t) = E_y(z)\hat{\mathbf{y}}\exp(-i\omega t) \quad [\text{B.3}]$$

where $E_x(z)$ and $E_y(z)$ are, in general, complex valued functions of z and $\hat{\mathbf{x}}$ and $\hat{\mathbf{y}}$ are unit vectors in the x and y directions, respectively. In terms of [B.2] and [B.3], $\bar{\mathbf{E}}(z,t)$ can be written as

$$\begin{aligned} \bar{\mathbf{E}}(z,t) &= \bar{\mathbf{E}}_x(z,t) + \bar{\mathbf{E}}_y(z,t) \\ &= [E_x(z)\hat{\mathbf{x}} + E_y(z)\hat{\mathbf{y}}]\exp(-i\omega t) \end{aligned} \quad [\text{B.4}]$$

However, this is not the only way of expressing $\bar{\mathbf{E}}(z,t)$. Another, equally valid, representation of $\bar{\mathbf{E}}(z,t)$ is in terms of orthogonal, circularly polarized, field vectors $\bar{\mathbf{E}}_+(z,t)$ and $\bar{\mathbf{E}}_-(z,t)$ defined by

$$\bar{\mathbf{E}}_+(z,t) = E_+(z)\hat{\mathbf{e}}_+\exp(-i\omega t) \quad [\text{B.5}]$$

$$\bar{\mathbf{E}}_-(z,t) = E_-(z)\hat{\mathbf{e}}_-\exp(-i\omega t) \quad [\text{B.6}]$$

where $E_+(z)$ and $E_-(z)$ are also, in general, complex valued functions of z and $\hat{\mathbf{e}}_{\pm}$ are circularly polarized basis vectors defined by

$$\hat{\mathbf{e}}_{\pm} = (\hat{\mathbf{x}} \mp i\hat{\mathbf{y}})/2 \quad [\text{B.7}]$$

In terms of these new vectors, $\bar{\mathbf{E}}(z,t)$ can be written as

$$\begin{aligned} \bar{\mathbf{E}}(z,t) &= \bar{\mathbf{E}}_+(z,t) + \bar{\mathbf{E}}_-(z,t) \\ &= [E_+(z)\hat{\mathbf{e}}_+ + E_-(z)\hat{\mathbf{e}}_-]\exp(-i\omega t) \end{aligned} \quad [\text{B.8}]$$

In contrast to the linearly polarized field components $\bar{\mathbf{E}}_x(z,t)$ and $\bar{\mathbf{E}}_y(z,t)$ which always lie along the x and y directions, the circularly polarized field components $\bar{\mathbf{E}}_{\pm}(z,t)$ rotate about the z axis with an angular velocity of ω rad/sec.

To see this, we use [B.7] to write:

$$\begin{aligned}\bar{\mathbf{E}}_{\pm}(z,t) &= E_{\pm}(z)\exp(-i\omega t)\hat{\mathbf{e}}_{\pm} \\ &= (1/2)E_{\pm}(z)(\hat{\mathbf{x}} \mp i\hat{\mathbf{y}})[\cos(\omega t) - i\sin(\omega t)]\end{aligned}\quad [\text{B.9}]$$

The components of the actual electric fields are obtained by taking the real part of [B.9]. Assuming, for simplicity, that the amplitudes $\bar{\mathbf{E}}_{\pm}(z,t)$ are real we get:

$$[\bar{\mathbf{E}}_{\pm}(z,t)]_x = (1/2)E_{\pm}(z)\cos(\omega t)\quad [\text{B.10}]$$

$$[\bar{\mathbf{E}}_{\pm}(z,t)]_y = \mp(1/2)E_{\pm}(z)\sin(\omega t)\quad [\text{B.11}]$$

Hence, if we were to look down the z axis (towards $z = -\infty$) the positive circularly polarized component $\bar{\mathbf{E}}_{+}(z,t)$ will rotate clockwise about the z axis with an angular velocity of ω rad/sec. while the negative circularly polarized component $\bar{\mathbf{E}}_{-}(z,t)$ will rotate counterclockwise about the z axis with an angular velocity of ω rad/sec.

Converting from the linear to the circularly polarized representations of $\bar{\mathbf{E}}(z,t)$ is quite simple. Equating [B.4] to

[B.8], and using [B.7] gives

$$\begin{aligned} [E_x(z)\hat{x} + E_y(z)\hat{y}] &= [E_+(z)\hat{e}_+ + E_-(z)\hat{e}_-] \\ &= (1/2)[E_+(z) + E_-(z)]\hat{x} \\ &\quad - (i/2)[E_+(z) - E_-(z)]\hat{y} \end{aligned} \quad [B.12]$$

Equating x and y components in [B.12] yields

$$2E_x(z) = E_+(z) + E_-(z) \quad [B.13]$$

$$2iE_y(z) = E_+(z) - E_-(z) \quad [B.14]$$

and inverting [B.13] and [B.14] gives the simple relations

$$E_{\pm}(z) = E_x(z) \pm iE_y(z) \quad [B.15]$$

Appendix C: Generalized Boundary Conditions

In this appendix we show how an electric field distribution satisfying arbitrary boundary conditions can be constructed by superposing two electric field distributions that satisfy particularly simple sets of boundary conditions.

In sections 2.2 to 2.5 of chapter 2 we found that the circularly polarized rf electric fields $E_{\pm}(z)$ present in a ferromagnetic metal slab that occupied the space $0 \leq z \leq d$ and had a d.c. magnetic field applied along the z axis, satisfied the two independent, second order, integro-differential equations

$$E_{\pm}''(z) + a_{\pm} \int_0^d K_{\pm}(z, \xi) E_{\pm}(\xi) d\xi = 0 \quad [C.1]$$

where $a_{\pm} = [2i\mu_{\pm}/(\sigma_0 \delta_0^2)]$ [C.2]

and $K_{\pm}(z, \xi)$ is the circularly polarized kernel as defined in section 2.4.

The solutions of equations [C.1] will each contain two arbitrary constants which we may take to be proportional to the electric field derivatives at the $z = 0$ and $z = d$ slab faces. Specifically, since the magnetic fields $h_{\pm}(z)$ are related to the

electric field derivatives by the circularly polarized Maxwell's equation

$$E'_{\pm}(z) = \pm(\omega\mu_{\pm}/c) h_{\pm}(z) \quad [C.3]$$

then we may fix the form of the solutions $E_{\pm}(z)$ by specifying the values of $h_{\pm}(0)$ and $h_{\pm}(d)$; that is, $E_{+}(z)$ is uniquely determined by $h_{+}(0)$ and $h_{+}(d)$ while $E_{-}(z)$ is uniquely determined by $h_{-}(0)$ and $h_{-}(d)$.

Consider the solutions of [C.1] that satisfy the particular choices

$$h_{\pm}(0) = 1; h_{\pm}(d) = 0 \quad [C.4]$$

Label the solutions as $G_{+}(z)$ and $G_{-}(z)$ or, for brevity, $G_{\pm}(z)$. Now consider the solutions of [C.1] satisfying

$$h_{\pm}(0) = 0; h_{\pm}(d) = 1 \quad [C.5]$$

If we label these new solutions as $F_{\pm}(z)$, then the electric field solutions $E_{\pm}(z)$ satisfying arbitrary values of $h_{\pm}(0)$ and $h_{\pm}(d)$ may be written as

$$E_{\pm}(z) = h_{\pm}(0)G_{\pm}(z) + h_{\pm}(d)F_{\pm}(z) \quad [C.6]$$

But, $F_{\pm}(z) = -G_{\pm}(d - z)$. To see this we take the boundary value problem satisfied by $G_{\pm}(z)$ and change variable from (z, ξ) to (z', ξ') where

$$z = d - z' \quad [C.7]$$

$$\xi = d - \xi' \quad [C.8]$$

Thus, we go from

$$G_{\pm}''(z) + a_{\pm} \int_0^d K_{\pm}(z, \xi) G_{\pm}(\xi) d\xi = 0$$

$$h_{\pm}(0) = 1; h_{\pm}(d) = 0$$

to

$$G_{\pm}''(d - z') + a_{\pm} \int_0^d K_{\pm}(d - z', d - \xi') G_{\pm}(d - \xi') d\xi' = 0$$

$$h_{\pm}(0) = 0; h_{\pm}(d) = -1$$

(the boundary conditions were transformed using [C.3] and the fact $E'_{\pm}(z) = -E'_{\pm}(d - z')$).

Now, under an inversion of space about the point $z = d/2$, the kernel remains invariant^{20, 37}; ie,

$$K_{\pm}(z', \xi') = K_{\pm}(d - z', d - \xi') \quad [C.9]$$

Using this in the integro-differential equation for $G_{\pm}(d - z')$ shows that if $G_{\pm}(z)$ is a solution of [C.1] that satisfies $h_{\pm}(0) = 1; h_{\pm}(d) = 0$ then $G_{\pm}(d - z)$ is a solution of [C.1] that satisfies $h_{\pm}(0) = 0; h_{\pm}(d) = -1$. The result $F_{\pm}(z) = -G_{\pm}(d - z)$ follows immediately and [C.6] can be re-written as

$$E_{\pm}(z) = h_{\pm}(0)G_{\pm}(z) - h_{\pm}(d)G_{\pm}(d - z) \quad [C.10]$$

The solutions of [C.1] that satisfy arbitrary values of $h_{\pm}(0)$ and $h_{\pm}(d)$ may therefore be expressed in terms of the particular solutions $G_{\pm}(z)$ that satisfy the simple boundary conditions $h_{\pm}(0) = 1; h_{\pm}(d) = 0$. As shown in section 2.5, this allows us to express experimentally observable quantities like the surface impedance and the transmission coefficient solely in terms of $G_{\pm}(0)$ and $G_{\pm}(d)$.

Appendix D: Semi-Classical Current Density Calculation

In this appendix we review how to use the Boltzmann transport equation to calculate semi-classically the current response in a metal due to applied electric and magnetic fields. We consider linear response (ie, the current density in the metal is linearly related to the applied electric field) and use the method of Cohen, Harrison, and Harrison²⁶ to solve the Boltzmann transport equation. The resulting expressions for the current density are particularly useful for calculating the current response in an infinite conducting medium due to applied delta function electric fields (see chapter 3).

The current density $\vec{j}(\vec{r}, t)$ generated in a metal due to arbitrary electric and magnetic fields can be calculated semi-classically using the expression^{32, 55}:

$$\vec{j}(\vec{r}, t) = -2e/(2\pi)^3 \int_{\vec{K}} \vec{v} f(\vec{r}, \vec{K}, t) d\vec{K} \quad [D.1]$$

where the volume integral extends over all k-space and $f(\vec{r}, \vec{K}, t)$ is the phase space distribution function for electrons of wavevector \vec{K} and velocity \vec{v} at position \vec{r} at time t . In the absence of all electric and magnetic fields, $f(\vec{r}, \vec{K}, t)$ reduces to f_0 , the equilibrium Fermi-Dirac distribution function

$$f_0(\epsilon(\vec{K})) = [1 + \exp((\epsilon(\vec{K}) - \epsilon_F)/k_B T)]^{-1} \quad [D.2]$$

When electric and magnetic fields are present, the conduction electrons move through the metal and suffer collisions with impurities, lattice defects, phonons, and other electrons. In a steady state, the rate of change of $f(\vec{r}, \vec{k}, t)$ due to the applied fields is just balanced by $[\partial f / \partial t]_{\text{coll}}$, the rate of change of f due to collisions. This may be expressed by the Boltzmann Transport equation:

$$\partial f / \partial t + \dot{\vec{k}} \cdot \partial f / \partial \vec{k} + \vec{v} \cdot \partial f / \partial \vec{r} = [\partial f / \partial t]_{\text{coll}} \quad [\text{D.3}]$$

where \vec{k} and \vec{r} are determined by the semi-classical equations of motion

$$\vec{v}(\vec{k}) = (1/\hbar) \partial \epsilon(\vec{k}) / \partial \vec{k} \quad [\text{D.4}]$$

$$\hbar \dot{\vec{k}} = -e[\vec{E}(\vec{r}, t) + (1/c) \vec{v} \times \vec{H}(\vec{r}, t)] \quad [\text{D.5}]$$

\vec{E} and \vec{H} are the net electric and magnetic fields in the metal.

In order to solve the Boltzmann equation for $f(\vec{r}, \vec{k}, t)$ in closed form, one usually assumes that the collision term $[\partial f / \partial t]_{\text{coll}}$ is given by the relaxation time approximation^{17, 56}:

$$[\partial f / \partial t]_{\text{coll}} = -(f - f_0) / \tau \quad [\text{D.6}]$$

The meaning of the collision term [D.6] is that $f(\vec{r}, \vec{k}, t) / \tau$ electrons scatter out of a unit volume of phase space (\vec{r}, \vec{k}) in a

unit time while $f_0(\epsilon(\mathbf{k}))/\tau$ electrons scatter in. If we were to suddenly remove all applied $\bar{\mathbf{E}}$ and $\bar{\mathbf{H}}$ fields, and if f were independent of $\bar{\mathbf{r}}$, f would decay exponentially into f_0 with a characteristic relaxation time τ which is assumed to be a constant throughout the metal. To see this, insert [D.6] into [D.3] and set $\partial f/\partial \bar{\mathbf{r}}$ and $\dot{\bar{\mathbf{k}}}$ to zero before solving for $f(\bar{\mathbf{r}}, \bar{\mathbf{k}}, t)$.

It can also be shown that the collision term [D.6] corresponds to elastic scattering of the conduction electrons. In a pure metal, at low temperatures (the case we are interested in), the conduction electrons mainly scatter off randomly placed massive impurity ions and point lattice defects: such scattering events are elastic.

There are several ways of solving the Boltzmann equation for $f(\bar{\mathbf{r}}, \bar{\mathbf{k}}, t)$. We shall consider the method due to Cohen, Harrison, and Harrison²⁶ which is similar to the Chambers solution¹⁸ but easier to work with.

Solution of the Boltzmann Equation: The Method of Cohen, Harrison, and Harrison

An electron will contribute to $f(\bar{\mathbf{r}}, \bar{\mathbf{k}}, t)$ only if it is at the phase space point $(\bar{\mathbf{r}}, \bar{\mathbf{k}})$ at time t . The only way an electron could get to $(\bar{\mathbf{r}}, \bar{\mathbf{k}})$ at t is if it had scattered on to the unique phase space trajectory T , that runs through $(\bar{\mathbf{r}}, \bar{\mathbf{k}})$, at some point $(\bar{\mathbf{r}}', \bar{\mathbf{k}}')$ at time $t' < t$ (see figure 45). According to the relaxation time approximation, the number of electrons which

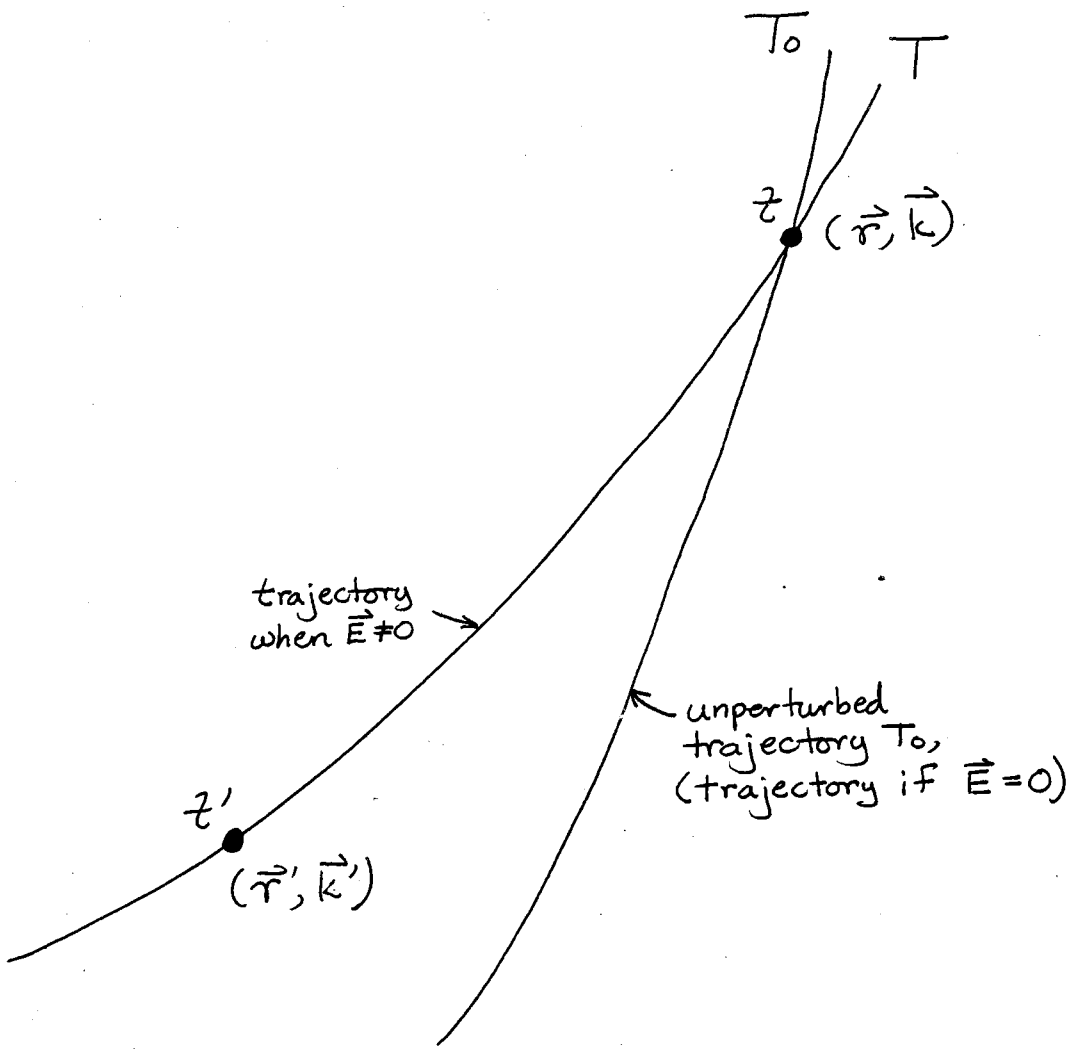


Fig. 45 The trajectory T of an electron in phase space when electric and magnetic fields are present. An electron which contributes to the distribution function $f(\vec{r}, \vec{k}, t)$ must have been scattered onto T at a time t' in the past at the corresponding point (\vec{r}', \vec{k}') and have followed T without scattering until it arrives at the point (\vec{r}, \vec{k}) at the time t . In the absence of the electric field, the electron follows the unperturbed trajectory T_0 .

scatter onto T in dt' at (\bar{r}', \mathbf{k}') is just $f_0(\epsilon(\mathbf{k}'))dt'/\tau$, and the probability that an electron will stay on T until it reaches (\bar{r}, \mathbf{k}) at time t is just $e^{-(t-t')/\tau}$. The distribution function $f(\bar{r}, \mathbf{k}, t)$ is obtained by summing over all times t' in the past. The result is

$$f(\bar{r}, \mathbf{k}, t) = \int_{-\infty}^t f_0(\epsilon(\mathbf{k}')) e^{-(t-t')/\tau} dt'/\tau \quad [D.7]$$

Now, during the time interval $[t', t]$ that an electron follows the trajectory T it will pick up energy $\Delta\epsilon(t') = \epsilon(\mathbf{k}) - \epsilon(\mathbf{k}')$ from the electric field \bar{E} . Thus, at time t' , $f_0(\epsilon(\mathbf{k}')) = f_0(\epsilon(\mathbf{k}) - \Delta\epsilon(t'))$ and we may re-write $f(\bar{r}, \mathbf{k}, t)$ as

$$f(\bar{r}, \mathbf{k}, t) = \int_{-\infty}^t f_0(\epsilon(\mathbf{k}) - \Delta\epsilon(t')) e^{-(t-t')/\tau} dt'/\tau \quad [D.8]$$

To proceed further we assume that $\Delta\epsilon/\epsilon \ll 1$ (ie, the applied electric field is weak) and the electron density is a constant (ie, the Fermi energy is independent of position) so we can expand $f_0(\epsilon(\mathbf{k}) - \Delta\epsilon(t'))$ about $\epsilon(\mathbf{k})$,

$$f_0(\epsilon(\mathbf{k}) - \Delta\epsilon(t')) \approx f_0(\epsilon(\mathbf{k})) - (\partial f_0 / \partial \epsilon) \Delta\epsilon(t')$$

Using this in [D.8] gives:

$$f(\bar{r}, \mathbf{k}, t) = f_0(\epsilon(\mathbf{k})) + g(\bar{r}, \mathbf{k}, t) \quad [D.9]$$

where

$$g(\bar{r}, \bar{k}, t) = -(\partial f_0 / \partial \epsilon) \int_{-\infty}^t \Delta \epsilon(t') e^{-(t-t')/\tau} dt' / \tau \quad [D.10]$$

and $\Delta \epsilon(t')$, the energy picked up by the electron in the time interval $[t', t]$, is given by

$$\Delta \epsilon(t') = -e \int_{t'}^t \bar{v}(\bar{k}'') \cdot \bar{E}(\bar{r}'', t'') dt'' \quad [D.11]$$

where \bar{k}'' and \bar{r}'' are chosen to lie on the unperturbed trajectory T_0 followed by the electron if the electric field \bar{E} were absent. This is permissible because we are only concerned with linear response (ie, a current response linear in the electric field).

Cohen, Harrison, and Harrison simplified [D.10] using integration by parts

$$\int u dv = uv - \int v du$$

with $u = \Delta \epsilon(t')$ and $dv = (dt' / \tau) e^{-(t-t')/\tau}$. Since $\Delta \epsilon(t) = 0$, $g(\bar{r}, \bar{k}, t)$ becomes:

$$g(\bar{r}, \bar{k}, t) = -(\partial f_0 / \partial \epsilon) \int_{-\infty}^t e^{-(t-t')/\tau} d[\Delta \epsilon(t')] \quad [D.12]$$

where

$$d[\Delta \epsilon(t')] = -e \bar{v}(\bar{k}') \cdot \bar{E}(\bar{r}', t') dt' \quad [D.13]$$

is the energy picked up by an electron during the infinitesimal

time interval $[t', t'+dt']$. Again, \bar{r}' and \bar{k}' lie along the unperturbed trajectory T_0 and correspond to the position of the electron in phase space at time t' .

The calculation of the current density $\bar{j}(\bar{r}, t)$ due to arbitrary, weak, electric and magnetic fields is now relatively straightforward. First, one uses the semi-classical equations of motion [D.4] and [D.5] to determine the unperturbed electron trajectory that runs through the phase space point (\bar{r}, \bar{k}) at time t . One then calculates $d[\Delta\epsilon(t')]$ from [D.13], inserts the result in [D.12], and does the integral over t' to get $g(\bar{r}, \bar{k}, t)$. The distribution function $f(\bar{r}, \bar{k}, t)$ is then given by $f = f_0 + g$ (see [D.9]). The current density $\bar{j}(\bar{r}, t)$ is obtained using [D.1]. Only g , the deviation of f from f_0 , will contribute to the current density. We may therefore write the current density expression as

$$\bar{j}(\bar{r}, t) = -2e/(2\pi)^3 \int_{\bar{k}} \bar{v}g(\bar{r}, \bar{k}, t)d\bar{k} \quad [D.14]$$

Note that at room temperatures and below, the term $(\partial f_0/\partial\epsilon)$ in $g(\bar{r}, \bar{k}, t)$ is very nearly equal to $-\delta(\epsilon-\epsilon_F)$ where $\delta(x)$ is the Dirac delta function and ϵ_F is the Fermi energy. This restricts the integral over k -space in $\bar{j}(\bar{r}, t)$ to an integral over the fermi surface. It also means that when we are working out the unperturbed phase space trajectory T_0 , we need only consider \bar{k} values on the Fermi surface.

Appendix E: The Exponential Integral

In this appendix we consider a numerical procedure for evaluating the exponential integral $E_1(z)$ for a complex argument. This function is needed to carry out the numerical solution to the electric field boundary value problem for the case of diffuse surface scattering (see chapter 5).

The exponential integral for a complex argument z can be defined by⁵⁷

$$E_1(z) = \int_1^{\infty} \frac{e^{-zu}}{u} du = \int_z^{\infty} \frac{e^{-t}}{t} dt \quad [\text{E.1}]$$

The function is analytic over the entire complex t plane except for a branch cut along the negative real axis that's associated with the $1/t$ term in the integrand. The function goes to infinity at $z = 0$.

Now, scientific subroutines exist that evaluate the function

$$E_1(x) = \int_x^{\infty} \frac{e^{-t}}{t} dt; \quad x \in \mathbb{R}, x > 0 \quad [\text{E.2}]$$

to 13 or so digits when the argument x is a real, positive number (see, for example, the IMSL subroutine MMDEI). However,

there seems to be no routines available for evaluating $E_1(z)$.

To evaluate the latter function we make use of the fact that the integral from z to ∞ in $E_1(z)$ is path independent as long as we do not cross the branch cut along the negative real axis. If we write $z = a + ib$, and assume that $a > 0$, then we can split the integral for $E_1(z)$ into two parts:

$$E_1(z) = E_1(a+ib) = \int_{a+ib}^a \frac{e^{-t}}{t} dt + \int_a^{\infty} \frac{e^{-t}}{t} dt; a > 0 \quad [E.3]$$

where the integral from $a + ib$ to a is along the vertical line $t = a$ and the integral from a to infinity is along the positive real axis. The second integral in [E.3] can be evaluated with an existing scientific subroutine. The first integral can be split up into real and imaginary parts.

$$\begin{aligned} \int_{a+ib}^a \frac{e^{-t}}{t} dt &= \int_b^0 \frac{e^{-a-iu}}{a+iu} i du = - \int_0^b \frac{e^{-a} e^{-iu} i (a-iu) du}{a^2 + u^2} \\ &= - e^{-a} \int_0^b \frac{u \cdot \cos(u) + a \cdot \sin(u)}{a^2 + u^2} du \\ &\quad - i e^{-a} \int_0^b \frac{u \cdot \sin(u) - a \cdot \cos(u)}{a^2 + u^2} du \end{aligned}$$

... [E.4]

Each part can be easily evaluated with some kind of numerical integration package like DCADRE (available from the IMSL scientific subroutine library).

Appendix F: Gauss-Laguerre Quadrature

Gauss-Laguerre quadrature⁴⁴ can be used to evaluate real valued integrals of the form

$$\int_0^{\infty} e^{-x} F(x) dx$$

by a finite sum:

$$\int_0^{\infty} e^{-x} F(x) dx \approx \sum_{i=1}^n A_i F(x_i)$$

where the arguments x_i are the zeros of the n^{th} Laguerre polynomial

$$L_n(x) = e^x \frac{d^n}{dx^n} (e^{-x} x^n)$$

and the A_i are given by

$$\begin{aligned} A_i &= \frac{1}{L'_n(x_i)} \int_0^{\infty} \frac{L_n(x) e^{-x}}{x - x_i} dx \\ &= \frac{(n!)^2}{x_i |L'_n(x_i)|^2} \end{aligned}$$

The maximum difference between the true integral and the approximation does not exceed⁴⁴

$$E = \frac{(n!)^2}{(2n)!} F^{(2n)}(\theta)$$

where θ is chosen to maximize $F^{(2n)}(x)$ on the interval $0 \leq x < \infty$.

The n -point Gauss-Laguerre quadrature formula gives exact results when $F(x)$ is a polynomial of degree $2n-1$ or less. Tables of x_i and A_i for values of n ranging from 10 to 20 can be found in numerical analysis texts⁴⁴.

Several mathematical subroutine libraries contain routines for evaluating integrals using the Gauss-Laguerre method. For example, the NAG library contains a function D01BAF (option D01BAX) that allows one to use up to $n = 64$ points.

BIBLIOGRAPHY

1. J.F. Cochran and B. Heinrich, IEEE Trans. Magn. 16, 660 (1980).
2. B. Heinrich, J.M. Rudd, K. Urquhart, K. Myrtle, and J.F. Cochran, J. Appl. Phys. 55, 1814 (1984).
3. G. Dewar, B. Heinrich, and J.F. Cochran, J. Appl. Phys. 50, 2437 (1979).
4. B. Heinrich and J.F. Cochran, J. Appl. Phys. 50, 2440 (1979).
5. C. Kittel, Phys. Rev. 110, 836 (1958).
6. G.C. Alexandrakis, J.W. Allen, and I.A. Privorotskii, J. Appl. Phys. 50, 2443 (1979).
7. C. Vittoria, M. Rubenstein, and P. Lubitz, Phys. Rev. B12, 5150 (1975).
8. S.M. Bhagat and P. Lubitz, Phys. Rev. B10, 179 (1974).
9. A.B. Pippard, "The Dynamics of Conduction Electrons" Gordon and Breach, New York, (1965).
10. G.E.H Reuter and E.H. Sondheimer, Proc. Roy. Soc. A195, 336 (1948).
11. K. Fuchs, Proc. Camb. Phil. Soc. 34, 100 (1938).
12. V.I. Okulov and V.V. Ustinov, FNT 5, 213 (1979)
13. J.F. Cochran and B. Heinrich, J. Appl. Phys. 50, 7729 (1979).
14. N.C. Banik and A.W. Overhauser, Phys. Rev. B16, 3379 (1977).
15. Ye. M. Kogan, Ye. A. Turov, and V.V. Ustinov, Fiz. Metal Mettalloed 53, 223 (1982)
16. P. Goy and C.C. Grimes, Phys. Rev. B7, 299 (1973).
17. E.H. Sondheimer, Advances in Physics 1, 1 (1952).
18. R.G. Chambers, Proc. Roy. Soc. A202, 378 (1950a).

19. G.V. Skrotskii and L.V. Kurbatov, "Ferromagnetic Resonance" Pergamon Press, New York, (1966) S. Vonsovskii, Ed.
20. J.F. Cochran, Can. J. Phys. 48, 370 (1970).
21. P.M. Platzmann and J.S. Buchsbaum, Phys. Rev. 132, 2 (1963)
22. G.A. Baraff, J. Math. Phys. 9, 372 (1968).
23. G.A. Baraff, Phys. Rev. B7, 580 (1973).
24. G.A. Baraff, Phys. Rev. 167, 625 (1968).
25. G.A. Baraff, Phys. Rev. 178, 1155 (1969).
26. M.H. Cohen, M.J. Harrison, and W.A. Harrison, Phys. Rev. 117, 937 (1960)
27. J.D. Jackson, "Classical Electrodynamics" John Wiley and Sons Inc., N.Y., (1975)
28. W.S. Ament and G.T. Rado, Phys. Rev. 97, 1558 (1955)
29. W.F. Brown "Micromagnetics" Robert E. Krieger Publishing Co., N.Y., (1978)
30. J.F. Cochran, B. Heinrich, and G. Dewar, Can. J. Phys., 55, 787 (1977)
31. S. Chikazumi, "Physics of Magnetism" John Wiley and Sons Inc., N.Y., (1964)
32. N.W. Ashcroft and N.D. Mermin, "Solid State Physics" Holt, Reinhart, and Winston, N.Y., (1976)
33. T.L. Gilbert, Phys. Rev. 100, 1234 (1955)
34. J.F. Cochran, B. Heinrich, and G. Dewar, Can. J. Phys. 55, 834 (1977)
35. M.G. Calkin, P.J. Nicholson, Rev. Mod. Phys. 39, 361 (1967)
36. E.A. Kaner and V.F. Gantmakher, Usp. Fiz, Nauk 94, 193 (1968)
37. D.K. Wagner and R. Cochran, J. Low Temp. Phys. 50, 549 (1975)
38. M.I. Kaganov, Fiz. Metal. Metalloved 7, 288 (1959)
39. B. Heinrich and V.F. Meshcheryakov, Zh. Eksp. Teor. Fiz. 59, 424 (1970)

40. R. Kalaba, J. Math. Phys. 11, 1999 (1970)
41. R.M. Wilcox, J. Math. Phys. 12, 1195 (1971)
42. R.L. Burden, J.D. Faires, A.C. Reynolds "Numerical Analysis", Prindle, Weber, and Schmidt, Boston, (1981)
43. M.R. Spiegel, "Schaum's Outline Series: Handbook of Mathematical Functions and Tables" Mc-Graw Hill, N.Y., (1968)
44. F. Scheid, "Schaum's Outline Series: Numerical Analysis" Mc-Graw Hill, N.Y., (1968)
45. M.R. Spiegel, "Schaum's Outline Series: Complex Variables" Mc-Graw Hill, N.Y., (1964)
46. P.D. Southgate, J. Appl. Phys. 40, 22 (1969)
47. V.F. Gantmakher and E.A. Kaner, Sov. Phys. JETP 48, 1572 (1965)
48. V.L. Gurevich, Sov. Phys. JETP 33, 1497 (1957)
49. G.T. Rado, J. Appl. Phys. 29, 330 (1958)
50. L.L. Hirst and R.E. Prange, Phys. Rev. 139, A892 (1965)
51. D. Pinkel, G.L. Dunifer, and S. Schultz, Phys. Rev. B18, 6658 (1978)
52. R. Kaul and E.D. Thompson, J. Appl. Phys. 40, 1383 (1969)
53. T. Tokunaga, J. of Science Hiroshima U. Series A 38, 215 (1974)
54. M.J. Laubitz, T. matsumura, and P.J. Kelly, Can. J. Phys. 54, 92 (1976)
55. J.M. Ziman, "Principles of the Theory of Solids" Cambridge University Press, N.Y., (1972)
56. D.K. Wagner and R. Bowers, Advances in Physics 27, 651 (1978)
57. Abramowitz and Stegun, "Handbook of Mathematical Functions" NBS, Wash. D.C., (1964)